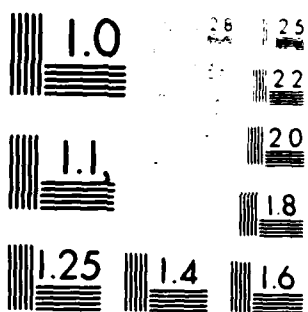


AD-A131 828 ACTA AERONAUTICA ET ASTRONAUTICA SINICA(U) FOREIGN
TECHNOLOGY DIV WRIGHT-PATTERSON AFB OH S LU ET AL.
28 JUL 83 FTD-ID(RS)T-0266-83

1 / 3

F/G 20/4 NL

NI



U.S. GOVERNMENT PRINTING OFFICE: 1963

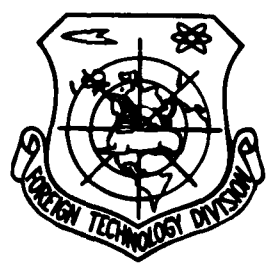
2

FTD-ID(RS)T-0266-83

FOREIGN TECHNOLOGY DIVISION



ACTA AERONAUTICA ET ASTRONAUTICA SINICA



FTD
1983
E

Approved for public release;
distribution unlimited.

ADA131829

DTIC FILE COPY



83 08 25 169

EDITED TRANSLATION

FTD-ID(RS)T-0266-83

26 July 1983

MICROFICHE NR: FTD-83-C-000951

ACTA AERONAUTICA ET ASTRONAUTICA SINICA

English pages: 189

Source: Hang Kong Xuebao, Vol. 3, Nr. 4, December
1982, pp. 1-108

Country of origin: China

Translated by: SCITRAN

F33657-81-D-0263

Requester: FTD/TQIA

Approved for public release; distribution unlimited.

Approved
1
2
3
4
5
6
7
8
9
10
11
12
13
14
15
16
17
18
19
20
21
22
23
24
25
26
27
28
29
30
31
32
33
34
35
36
37
38
39
40
41
42
43
44
45
46
47
48
49
50
51
52
53
54
55
56
57
58
59
60
61
62
63
64
65
66
67
68
69
70
71
72
73
74
75
76
77
78
79
80
81
82
83
84
85
86
87
88
89
90
91
92
93
94
95
96
97
98
99
100

X

THIS TRANSLATION IS A RENDITION OF THE ORIGINAL FOREIGN TEXT WITHOUT ANY ANALYTICAL OR EDITORIAL COMMENT. STATEMENTS OR THEORIES ADVOCATED OR IMPLIED ARE THOSE OF THE SOURCE AND DO NOT NECESSARILY REFLECT THE POSITION OR OPINION OF THE FOREIGN TECHNOLOGY DIVISION.

PREPARED BY:

TRANSLATION DIVISION
FOREIGN TECHNOLOGY DIVISION
WP-AFB, OHIO.

FTD -ID(RS)T-0266-83

Date 28 July 19 83

TABLE OF CONTENTS

	<u>Pages</u>
State-space aeroelastic modeling and its application in flutter calculations	1
Study on longitudinal dynamic characteristics of pilot-airplane systems - approach to the method for studying the PIO ¹ problem	20
Statistical determination of a flaw detection probability curve	35
Multi-level substructural analysis in modal synthesis - two improved substructural assembling techniques	49
9-node quadrilateral isoparametric element	64
Application of laser holographic interferometry to vibration analysis of aircraft beam structure model	73
On experimental methods for determining critical speeds	82
Three dimensional elastoplastic finite element analysis	96
An azimuth rate inertial navigation system	112
Optimal guidance laws for missiles with second-order characteristics	129
An optimal guidance law via first-order inertial loop	148
Deformation work density fracture criterion for composite materials	165
Numerical calculation of local convective heat transfer coefficients over air-cool vane surfaces	177
A briefing on the conference on new technologies in chemical analysis	186
Chinese society of aeronautics and astronautics holds inaugural meeting for committee on flight mechanics and flight tests	187
Chinese society of aeronautics and astronautics, Chinese society of mechanics and Chinese society of space navigation	188

GRAPHICS DISCLAIMER

All figures, graphics, tables, equations, etc.
merged into this translation were extracted
from the best quality copy available.

STATE-SPACE AEROELASTIC MODELING AND ITS APPLICATION
IN FLUTTER CALCULATION

Lu Shu-ch'uan*
(Nanching Aeronautical Institute)

ABSTRACT

In this paper, the available state-space aeroelastic models are reviewed, and several suggestions for improvement are proposed. A new state-space aeroelastic model is also proposed. Flutter calculation is carried out on two types of wings. These examples show that the new state-space aeroelastic model is one of high accuracy and low order. A method is presented by which the modals can be automatically identified and the flutter point automatically determined during the course of flutter calculation using state-space aeroelastic modeling.

I. INTRODUCTION

In recent years active flutter suppression has been widely studied, and research interests have included the problem of simplifying the control law for multiple input and multiple output systems under various limiting conditions. It is therefore necessary to establish aeroelastic models that are compatible with modern control theories. The crux lies in establishing a non-steady-state aerodynamic model. The aerodynamic forces found in the literature on flutter theory have been derived under the conditions of simple harmonic motion. In applying the modern control theories, however, it is necessary to have an expression for the aerodynamic forces that is valid under

* Received in May, 1982.

any given conditions of motion, and that takes the form of a rational function. In other words, the non-steady-state aerodynamic forces at the various dispersed points on the imaginary axis of the Laplace complex plane need to be extended to the entire plane. Furthermore, this approximate expression should be a rational function of the Laplace variable s . Its accuracy of fitting should be high, and the order of the corresponding aeroelastic model should be low. This type of rational approximation was first proposed by Jones[1], and expanded later by several other authors [2,3,4].

Although no solid proof has been given, this method of extension does have some significance. For, in flutter calculation, the problem of greatest concern is that of determining the critical conditions, under which the motion is simple harmonic motion. The error for the points in the neighborhood of the imaginary axis (which approximately undergo simple harmonic motion) cannot be too large either.

We have reviewed various methods that are presently available, and proposed some suggestions for improvement. We have also proposed a new state-space aeroelastic model.

Because several state-space coordinates are introduced in the state-space aeroelastic model which are not present in the original structural model, extra roots are produced. A brief discussion is given on their properties. The first and second derivatives of the characteristic values with respect to velocity have been derived in this paper, and have been used to automatically identify modals (including the extra roots) and automatically determine the flutter point.

II. PRESENTLY AVAILABLE NON-STEADY-STATE AERODYNAMIC MODELS

The Laplace transform for the flutter equation of motion is

$$([M_s]s^2 + [B_s]s + [K_s])\{X(s)\} = q[A]\{X(s)\} \quad (1)$$

where $\{X(s)\}$ is the vector of general coordinates of the model, of order $(n,1)$; $[M_s]$, $[B_s]$ and $[K_s]$ are, respectively, the mass, resistance and rigidity matrices of the structure; s is the Laplace variable. $[A]$ is the matrix of the coefficients of influence of the aerodynamic forces, and is a function of \bar{s} , where $\bar{s} = \frac{sb}{V}$ is the dimensionless quantity of s . b is the half-chord length of the wing. V is the velocity of the oncoming stream. q is the velocity pressure.

The problem at hand is this: Given the matrix of the coefficients of influence of the simple harmonic non-steady-state aerodynamic forces for a set of values of k :

$$[A(k_l)] = [F(k_l)] + i[G(k_l)] \quad (l = 1, 2, \dots, L)$$

where $k = \frac{wb}{V}$ is the reduction frequency, find a rational approximation that can be used in the fitting.

The presently available rational approximations are:

1. Roger's approximation [2]:

$$[A_{\omega}] = [Q_1] + [Q_2]\bar{s} + [Q_3]\bar{s}^2 + \sum_{i=1}^N \frac{[E_i]\bar{s}}{\bar{s} + r_i} \quad (2)$$

The resulting aeroelastic model is of order $(N+2) \cdot n$. In most applications [5,6], $N=4$, i.e., the order is $6n$. Usually, r_i is taken to be the N values of k within the range of the reduction frequency studied.

2. Padé's approximation in matrix form [3,4]:

$$[A_{op}] = (\bar{s}[I] - [R])^{-1}([P_1] + [P_2]\bar{s} + [P_3]\bar{s}^2) \quad (3)$$

The resulting model is of order $3n$.

3. Karpel's approximation [4]:

$$[A_{op}]_{(n,n)} = [Q_1] + [Q_2]\bar{s} + [Q_3]\bar{s}^2 + \underset{(n,m)}{[D]} (\bar{s}[I] - \underset{(m,m)}{[R]})^{-1} \underset{(m,n)}{[E]}\bar{s} \quad (4)$$

The numbers in the parentheses below the equation denote the order of the matrices. The resulting model is of order $2n+m$.

4. Indices for fitting accuracy:

In this paper, three indices are used in evaluating the fitting accuracy.

(1) Total relative error ϵ ;

$$\epsilon = \sqrt{\frac{\sum_{l=1}^L \sum_{i=1}^n \sum_{j=1}^n [(F_{ap,ij}(k_l) - F_{ij}(k_l))^2 + (G_{ap,ij}(k_l) - G_{ij}(k_l))^2]}{\sum_{l=1}^L \sum_{i=1}^n \sum_{j=1}^n (F_{ij}^2(k_l) + G_{ij}^2(k_l))}} \quad (5)$$

F_{ap} and G_{ap} are the F and G matrices obtained in the process of fitting. i and j are the subscripts of the elements of the matrices.

(2) Relative error of the elements ϵ_{ij} ;

For each element of the $[F_{ap}(k_1)]$ and $[G_{ap}(k_1)]$ corresponding

to the L values of k there is one relative error. There are $2\ln^2$ in all which we will not list here one by one. In fact, the error of each element depends on the form of the approximate equation, the manner in which each element varies with the value of k and the relative amount of these variations. For a given set of subscripts, these three contributions are of a common nature. Therefore, the errors of elements with the same subscripts can be superposed, i.e.

$$\epsilon_{ij} = \sqrt{\frac{\sum_{l=1}^L [(F_{app,ij}(k_l) - F_{ij}(k_l))^2 + (G_{app,ij}(k_l) - G_{ij}(k_l))^2]}{\sum_{l=1}^L (F_{ij}^2(k_l) + G_{ij}^2(k_l))}} \quad (6)$$

(3) Error in flutter velocity ϵ_{vf}

$$\epsilon_{vf} = \frac{V_f - V_{f0}}{V_{f0}} \quad (7)$$

where V_{f0} is the flutter velocity in the absence of control obtained from the data collected prior to fitting, and V_f is that obtained from the various approximate equations.

Among the above three types of errors, ϵ reflects the total fitting accuracy, and is the main index. After the fitting, ϵ_{ij} ought to be examined to see if any important model has a large error in the range of reduction frequency of interest. ϵ_{vf} is also just an index for reference only. It only indicates the error of flutter velocity in the absence of control, while in the presence of control, there may be very large variations in flutter velocity.

5. Comparison and Analysis:

Two examples have been computed in this paper.

Example 1 is a triangular wing with degree of freedom $n=4$. The matrix $[A]$ of aerodynamic force is computed for $k=0.1, 0.2, 0.25, 0.2857, 0.3333, 0.3636, 0.4, 0.5, 0.6667$ and 1 using the method given in Reference [7] for subsonic flow. The V_{f0} thus obtained is 908.4 ft/sec. (The experimentally obtained value is 924 ft/sec.) The errors obtained from the above three fitting equations are listed Table 1.

Example 2 is a swept-back wing, with $n=3$. Fitting of $[A]$ is done for $k=0.2, 0.2222, 0.25, 0.2857, 0.3333, 0.4, 0.5, 0.6667$ and 1. The results are shown in Table 2.

In the above examples, when using Roger's equation, we take $N=4$ and $r=0.2, 0.4, 0.6$ and 0.8 . When using Karpel's equation, we take $m=4$ and the initial values of r to be $-0.2, -0.4, -0.6$ and -0.8 .

It is obvious from Tables 1 and 2 that, among the three methods, the fitting accuracy is highest for Roger's equation. The total error ϵ is small, and its ϵ_{ij} are particularly small. However, it has a relatively high order. The orders of the other two methods are half as high, but their ϵ is rather large for the second example. In particular, the ϵ_{ij} for some of the elements are very large. ϵ_{vf} is small for all three methods. Although the latter two methods have larger ϵ , their ϵ_{vf} remains small because of the requirements that $[A]$ or its imaginary part be perfectly fitted when $k=k_f$.

The main reason for Roger's equation to have a higher fitting accuracy is as follows. In the process of fitting, after r_i is determined, each element in the same matrix is independently

determined. On the other hand, in the other two methods, the elements in the same matrix must be determined simultaneously. Thus, in the process of fitting, the accuracy of the larger elements is ensured at the expense of that of the smaller elements. The larger the extent of correlation, the larger the error.

Fitting accuracy is also affected by the method of fitting. In the latter two methods, the special conditions of $k=0$ and of k_{f1} and k_{f2} are utilized to establish the three relations for the special matrices. Although the computation is thus simplified, it is accompanied by a large error. Moreover, the relation used in the Karpel approximation to fit $[R]$, $[D]$, and $[E]$ is nonlinear. Even after many iterations, good fitting can only be obtained locally. This adversely affects the increase in accuracy.

When carrying out flutter calculations using the above approximations, it is necessary to introduce augmented state coordinates. This gives rise to extra roots. In our two examples, the extra roots produced by using Roger's and Karpel's equations are stable roots. Because no restriction is placed on eigenvalues of $[R]$ by Pade's matrix relation, unstable eigenvalues are produced in both examples. These extra roots arise because of the mathematical model of aerodynamics used, and do not exist in the actual physical model. Therefore, they can be singled out in the computations. (See Section V.) However, in the simulation, it must be ensured that negative characteristic values exist.

It can be seen from the above that Roger's approximation has the highest accuracy, and its extra roots are all stable. However, its order is relatively high. By carefully selecting the r_i values, the fitting accuracy can be further enhanced.

Karpel's approximation has a lower order, and a fitting accuracy improved over that of Pade's. However, the nonlinearity in the fitting places a limit on the improvement of fitting accuracy. See Section III for an improvement of this situation.

Pade's matrix approximation has the lowest accuracy.

III. IMPROVED KARPEL METHOD - THE METHOD OF SUBMATRICES

In Equation (4), take m such that it is an integral factor of n , and subdivide each matrix into several $m \times m$ submatrices. As

$$[D_i](ik[I] - [R])^{-1} = (ik[I] - [\bar{Q}_i])^{-1}[D_i] \quad (8)$$

where

$$[\bar{Q}_i] = [D_i][R][D_i]^{-1} \quad (9)$$

the following relation holds for a certain submatrix on the left hand side of Equation (4):

$$[F_{ij}] + i[G_{ij}] = [Q_{1,ij}] + ik[Q_{2,ij}] - k^2[Q_{3,ij}] + (ik[I] - [\bar{Q}_i])^{-1}[D_i][E_{ij}]ik \quad (10)$$

Multiplying $(ik[I] - [\bar{Q}_i])$ to both sides of Equation (10), separating the result into the real and imaginary parts, and transposing, one obtains

$$\left. \begin{aligned} [Q_{1,ij}]^T[\bar{Q}_i]^T + k^2([Q_{2,ij}]^T - [Q_{3,ij}]^T[\bar{Q}_i]^T) - [F_{ij}]^T[\bar{Q}_i]^T &= k[G_{ij}]^T \\ k([Q_{3,ij}]^T[\bar{Q}_i]^T - [Q_{1,ij}]^T - [E_{ij}]^T[D_i]^T) + k^2[Q_{3,ij}]^T - [G_{ij}]^T[\bar{Q}_i]^T &= -k[F_{ij}]^T \end{aligned} \right\} \quad (11)$$

Combine the relations for the submatrices in the same subrow and put them in the form of a set of linear equations in the unknown matrices $[Q_{1,i}]^T[\bar{Q}_i]^T$, $[Q_{2,i}]^T[\bar{Q}_i]^T$, $[Q_{3,i}]^T[\bar{Q}_i]^T$, $[F_i]^T$, $[G_i]^T$, $[D_i]^T$, $[E_i]^T$. $[Q_{i,1}]$ denotes the first subrow ($i=1, 2, 3$) of $[Q_i]$. First solve for these five sets of matrices, then find the eigenvalues and eigenvectors of $[\bar{Q}_1]$, to be formed separately into $[R]$ and $[D_1]$. $[Q_{3,1}]$, $[Q_{2,1}]$, $[Q_{1,1}]$ and $[E]$ can then be solved from the other four sets of matrices.

In solving the other subrows, first express $(k|I) = Q + iD$ of Equation (10) as $(D)(k|I) = (R)$, and write $(k|I) = (R)$ as $[AR] + i[Ai]$. Then separate Equation (10) into the real and imaginary parts, giving

$$(F_1) = (Q_{1,1}) - k^2(Q_{1,1}) - k D(A)(R)(F_1) \quad (12)$$

$$(1 \neq 1)$$

$$(G_1) = k^2(Q_{1,1}) + k D(A)(R)(F_1) \quad (13)$$

Again, combine the relations for the submatrices in the same subrow and transpose, and one obtains the set of linear equations in the unknown matrices $(Q_{1,1})$, $(Q_{2,1})$, $(Q_{3,1})$, (D) which can be solved for readily.

It can be seen from Tables 1 and 2 that, with respect to the two examples, the fitting accuracy of the results obtained by this method is much better than that of Karpel's method. ϵ_{12} is small in general. ϵ_{15} is very small. Only ϵ_{21} in example 1 is high. This is because the absolute value of the element with the same subscripts is the smallest. In example 2, there are unstable extra roots, which can be eliminated by placing restrictions on the eigenvalues.

In summary, in the above method, Karpel's nonlinear fitting equation is transformed into a set of linear equations. The fitting accuracy is thus greatly improved.

IV. A NEW APPROXIMATION

Putting together as much as possible the merits of the various methods, we propose the following approximation:

$$(A_{ij}) = (Q_1) + (Q_2)i + (Q_3)i^2 + \sum_{r=1}^N \frac{(D)(E)}{i+r} i^r \quad (14)$$

The steps for determining the matrices in the above relation are as follows:

(1) Assign a value to N .

(2) Assign initial values to r_1 .

(3) Take $d_{i,j}=1$ for a certain row (such as the j th row), where $i=1,2,\dots,N$, and determine the j th row of $[Q_1]$, $[Q_2]$ and $[Q_3]$, as well as $[E_i]$ ($i=1,2,\dots,N$), using the same method as Roger's.

(4) For the other rows (e.g., the i th row), one has

$$\left. \begin{aligned} ([Q_{1,i}])^T - k_i^2 ([Q_{3,i}])^T + \sum_{m=1}^N \frac{k_i^2}{r_m^2 - k_i^2} (E_m) d_{m,i} &= ([F_i(k)])^T \\ k_i ([Q_{2,i}])^T - \sum_{m=1}^N \frac{r_m k_i}{r_m^2 - k_i^2} (E_m) d_{m,i} &= ([G_i(k)])^T \end{aligned} \right\} \quad (l = 1, 2, \dots, L) \quad (15)$$

In the above equation, $[Q_{1,i}]$ represents the i th row of $[Q_1]$, $d_{m,i}$ denotes the i th element of $[D_m]$, etc. $[Q_{1,i}]$, $[Q_{2,i}]$, $[Q_{3,i}]$ and the various $d_{m,i}$ are solved for.

(5) Find ϵ .

(6) Determine r_i (with the restrictive condition that r_i be greater than 0.05), and repeat steps (3) to (5), until the iteration converges.

(7) If accuracy is poor, increase the value of N and repeat steps (2) and (6).

In the above process, the fitting accuracy is highest for the j th row that is the first to be determined. Therefore, fitting should be carried out first on the row where the elements with larger absolute values or the degree of freedom corresponding

to the most important model are found.

Tables 1 and 2 show the results obtained by this method ($N=4$). In example 1, ϵ of this method is smaller than that of Roger's. In example 2, it is larger than that of Roger's. This method results in slightly higher ϵ_{ij} than that of Roger's method, while ϵ_{vf} is small for both. However, the order of this method is only about half as high as that of Roger's method. The accuracy of our method is obviously much higher than the other two methods.

In summary, this method provides a model with high accuracy and low order. This is because the augmented subspace corresponding to each relation in the approximation is of order 1, while the subspace corresponding to the relations in Roger's approximation is of order n . Moreover, the interdependence of the elements in our approximation is reduced to a minimum, and the values of r are carefully selected, thus the improved fitting accuracy.

V. METHOD FOR AUTOMATICAL MODAL IDENTIFICATION AND FLUTTER POINT DETERMINATION

From Equation (A6) of the Appendix, it can be seen that the unified state-space aeroelastic model is given by

$$\{\dot{q}\} = [H]\{q\} \quad (16)$$

For the significance of the symbols, see the Appendix. The real part of the eigenvalue of the above equation represents the rate of attenuation, while the imaginary part represents the frequency of vibration.

In the above equation, $[q]$ contains the augmented state coordinates X_{ai} ($i=1,2,\dots,N$). Therefore, N extra eigenvalues have

been introduced. These need to be distinguished from the structural models in the computation.

To identify the modals, one needs to find the first and second order derivatives of the eigenvalues s with respect to the velocity V . The first order derivative of the m th eigenvalue S_m with respect to velocity is

$$(S_m)_v = [p_m] (H)_v \{q_m\} \quad (17)$$

In the equation, $[p_m]$ and $\{q_m\}$ are, respectively, the m th left and right eigenvectors. The second derivative of S_m with respect to velocity is:

$$(S_m)_{vv} = [p_m] (H)_{vv} \{q_m\} + 2 \sum_{\substack{i=1 \\ i \neq m}}^M a_{mi} [p_m] (H)_v \{q_i\} \quad (18)$$

where M is the total order of the model, and

$$a_{mi} = [p_m] (H)_v \{q_i\} / (S_m - S_i) \quad (19)$$

With the help of these two derivatives, the modal can be automatically identified. The main line of thought is as follows.

(1) Calculate the eigenvalues for $v \neq 0$. At this point, the imaginary parts of the eigenvalues corresponding to the structural modals approximate the individual vibration frequencies, while the imaginary parts of the eigenvalues corresponding to the augmented modals are approximately zero. Hence, if one arranges the eigenvalues in the order of decreasing magnitude of the imaginary part, the first $2n$ eigenvalues will be the ones corresponding to the structural models.

(2) Calculate $(S_m)_v$ and $(S_m)_{vv}$. Assume the increase in velocity to be ΔV , then one can use the derivative at $V=V_i$ to represent the eigenvalue $S_{m,i+1}$ at $V_{i+1} = V_i + \Delta V$:

$$S_{m,i+1}' = S_{m,i} + (S_{m,i})_v \cdot \Delta V + \frac{1}{2} (S_{m,i})_{vv} \cdot \Delta V^2 \quad (20)$$

(3) Solve for the eigenvalues $S_{m,i+1}$ from Equation (16), and compare it with $S_{m,i+1}'$. If the discrepancies in the real and imaginary parts all lie within a certain range (eg. $\pm 10\%$), then these two eigenvalues correspond to the same modal. Otherwise, interchange the order of the eigenvalues.

(4) In Equation (20), it has been assumed that $(S_m)_{vvv} \cdot \Delta V^3$ is a small quantity. Hence, if there is a relatively large difference between the values of $S_{m,i+1}$ and $S_{m,i+1}'$, one can reduce the step size ΔV until it is possible to automatically identify the modals.

(5) The point corresponding to the condition where the real part of the structural modal is zero is the flutter point.

Figure 1 shows the result of the flutter calculation. The branches 1-4 correspond to the structural modals, while branch 5 corresponds to the augmented space coordinates. $\omega = 0$ for the other two modals and is not shown in the figure. From Figure 1a it can be seen that the frequency of branch 5 increases sharply with increasing velocity. Therefore, it is not possible to distinguish the modals by traditional means (i.e., to order the modals according to the magnitude of the frequency). From Figure 1b, when $v = 360$ ft/sec, there is a relatively large variation in the real part of the eigenvalue. Therefore, the step sizes are reduced in the calculations to keep track of the variation. Thus, this method can be used to identify the modals and determine the flutter point automatically even in fairly complicated situations.

VI. CONCLUSIONS

1. It has been shown that the accuracy of matrix Pade approximation is unsatisfactory even though its order is much lower than Roger's. So does the order of Karpel's, whose fitting accuracy is better than that of Pade's, but improvement of the accuracy is limited by nonlinearity of the fitting equation. The accuracy of Roger's approximation is the best because of independent determination of elements in the same matrix, but its order is also the highest.

Improvements to the Karpel fitting method which are proposed in this paper, simply deal with the conversion of nonlinear problems into linear ones, which not only simplifies calculation but improves the fitting accuracy somewhat.

2. The fitting accuracy of the new approximate expression proposed in this paper is comparable to that of Roger but its order number is only half that of Roger. It provides a model with fitting accuracy which is relatively high but an order number which is relatively low.

3. This paper proposes first and second order derivative expressions for flutter determinant eigenvalues versus velocity in state space. Using these can automatically identify model state and automatically determine flutter point.

Table 1. Error comparison between various methods

① 近似式名称	Roger	② Pade' 型矩阵	Karpel	③ 子矩阵法	④ 本文的方法
⑤ 阶数	24	12	12	12	12
ϵ_0	0.58%	1.98%	1.82%	0.48%	0.22%
ϵ_{01}	-0.9%	-0.3%	-0.6%	-0.5%	0.1%
ϵ_{11}	0.001	0.027	0.027	0.064	0.025
ϵ_{12}	0.000	0.046	0.021	0.038	0.010
ϵ_{13}	0.001	0.004	0.007	0.003	0.002
ϵ_{14}	0.001	0.046	0.010	0.004	0.005
ϵ_{21}	0.016	0.203	0.130	0.336	0.087
ϵ_{22}	0.001	0.063	0.024	0.056	0.004
ϵ_{23}	0.002	0.015	0.023	0.006	0.006
ϵ_{24}	0.005	0.108	0.019	0.008	0.015
ϵ_{31}	0.003	0.084	0.015	0.061	0.001
ϵ_{32}	0.006	0.066	0.031	0.052	0.003
ϵ_{33}	0.005	0.011	0.011	0.004	0.001
ϵ_{34}	0.009	0.057	0.044	0.010	0.003
ϵ_{41}	0.002	0.116	0.060	0.051	0.056
ϵ_{42}	0.002	0.044	0.009	0.029	0.016
ϵ_{43}	0.009	0.010	0.037	0.006	0.005
ϵ_{44}	0.002	0.037	0.027	0.004	0.004

Table 2. Error comparison between various methods

① 近似式名称	Roger	② Pade' 型矩阵	Karpel	③ 子矩阵法	④ 本文的方法
⑤ 阶数	18	9	10	9	10
ϵ	0.55%	0.55%	21.59%	0.74%	0.83%
ϵ_{01}	0.3%	-5.5%	1.3%	0.8%	1.0%
ϵ_{11}	0.007	0.062	0.060	0.009	0.003
ϵ_{12}	0.016	0.220	0.170	0.014	0.011
ϵ_{13}	0.002	0.104	0.234	0.004	0.001
ϵ_{21}	0.028	0.089	0.172	0.015	0.046
ϵ_{22}	0.006	0.041	0.138	0.015	0.023
ϵ_{23}	0.005	0.034	0.242	0.002	0.005
ϵ_{31}	0.003	0.095	0.125	0.018	0.021
ϵ_{32}	0.010	0.091	0.038	0.024	0.031
ϵ_{33}	0.008	0.110	0.274	0.008	0.010

Key: 1) name of approximation; 2) Pade matrix approximation;
3) the method submatrices; 4) method of this paper; 5) order.

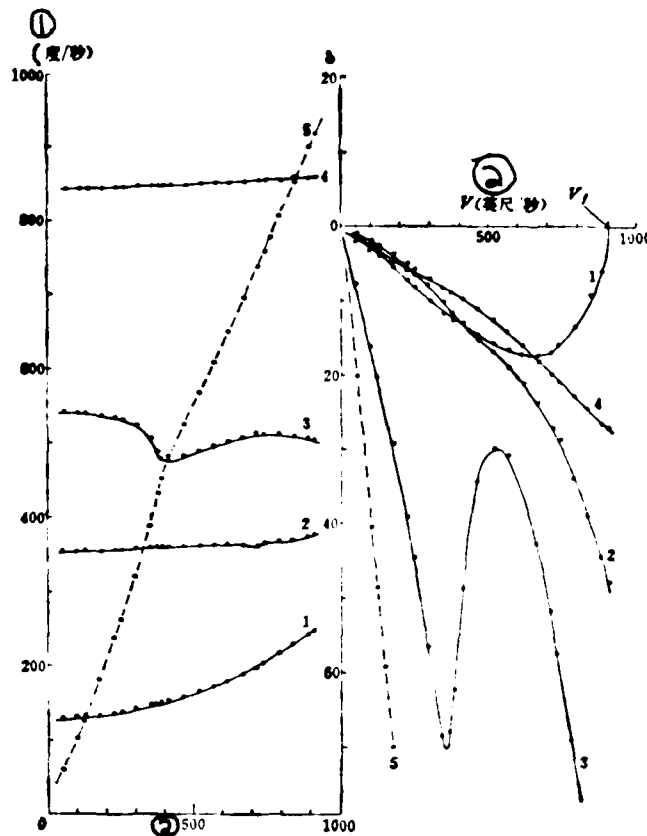


Figure 1a. Variation of frequency (imag. part of eigenvalue) with velocity.

Key: 1) deg/sec; 2) ft/sec.

Figure 1b. Variation of real part of eigenvalue with velocity.

APPENDIX

Equation of Motion for State-Space Flutter

The Laplace transforms for the equation of motion for the flutter of an aeroelastic system with n degrees of freedom is

$$((M_s)S^2 + (B_s)S + (K_s))\{X(S)\} = q\{A\}\{X(S)\} \quad (A1)$$

For the meanings of the symbols, see Equation (1).

The general form of the rational approximation of [A] is given by

$$\{A_{nr}\}_{(n,n)} = \{Q_1\}_{(n,n)} + \{Q_2\}_{(n,n)} s + \{Q_3\}_{(n,n)} s^2 + \sum_{i=1}^N \{D_i\}_{(n,m)} (s(I) + \{R_i\}_{(m,m)}^{-1} \{E_i\}_{(m,n)} s) \quad (A2)$$

The numbers in the parentheses below the equation denote the order of the matrices. The correspondence between the matrices in the various approximation equations discussed in the paper and those in Equation (A2) is given in Table A1.

Substitute Equation (A2) into Equation (A1). After rearranging, one gets

$$S^2\{M\}\{X(S)\} = \left(-S\{B\} - \{K\} + q \sum_{i=1}^N \{D_i\}(s(I) + \{R_i\}^{-1}\{E_i\} s) \right) \{X(S)\} \quad (A3)$$

where

$$\{M\} = \{M_1\} - \frac{1}{2} \rho b^2 \{Q_2\}$$

$$\{B\} = \{B_1\} - \frac{1}{2} \rho b l^2 \{Q_2\}$$

$$\{K\} = \{K_1\} - \frac{1}{2} \rho l^3 \{Q_2\}$$

If we take

$$\{X_n(S)\} = (s(I) + \{R_i\}^{-1}\{E_i\} s) \{X(S)\} \quad (A4)$$

and substitute it into Equation (A3), we obtain, after rearrangement and conversion, the equation of motion for the state-space flutter;

$$\begin{bmatrix} \dot{x} \\ \ddot{x} \\ x_{n1} \\ \vdots \\ x_{nN} \end{bmatrix} = \begin{bmatrix} 0 & [I] & 0 & \cdots & 0 \\ -\{M\}^{-1}\{K\} & -\{M\}^{-1}\{B\} & q\{M\}^{-1}\{D_1\} & \cdots & q\{M\}^{-1}\{D_N\} \\ 0 & \{E_1\} & -\frac{V}{b}\{R_1\} & & 0 \\ \vdots & \vdots & & \ddots & \\ 0 & \{E_N\} & 0 & & -\frac{V}{b}\{R_N\} \end{bmatrix} \begin{bmatrix} x \\ \dot{x} \\ x_{n1} \\ \vdots \\ x_{nN} \end{bmatrix} \quad (A5)$$

This equation can be written in the concise form:

$$\{\dot{q}\} = [H]\{q\} \quad (A6)$$

The total order of the equation is $2N + Nm$.

Table A1. Table for corresponding symbols

① 有理近似式 名称	② 总阶数	m	N	Q_1 (n, n)	Q_2 (n, n)	Q_3 (n, n)	D_i (n, m)	R_i (m, m)	E_i (m, n)
Roger	$(N+2)n$	n	N	Q_1	Q_2	Q_3	I	$r_i I$	E_i
③ Pade' 型矩阵	$3n$	n	1	$Q_1 \bullet$	$Q_2 \bullet$	0	I	$-R$	$E \bullet$
Karpel	$2n + m$	m	1	Q_1	Q_2	Q_3	D	$-R$	E
④ 本文的方法	$2n + N$	1	N	Q_1	Q_2	Q_3	D_i	r_i	E_i

Key: 1) name of the rational approximation; 2) total order; 3) Pade's matrix approximation; 4) method of this paper; 5) with respect to Pade's matrix approximation, we have:

$$\begin{aligned} [Q_1] &= -[R][P_1] \\ [Q_2] &= [P_2] \\ [E] &= [P_2] - [Q_1] + [R][Q_2] \end{aligned}$$

REFERENCES

1. Jones, R.T., "The Unsteady Lift of a Wing of Finite Aspect Ratio", NACA R-681, 1941.
2. Roger, K.L., "Airplane Math Modeling Methods for Active Control Design", AGARD-CP-228, August 1977.
3. Vepa, R., "Finite State Modeling of Aeroelastic Systems", NASA CR-2779, 1977.
4. Karpel, M. "Design for Active Flutter Suppression and Gust Alleviation Using State-Space Aeroelastic Modeling", AIAA paper 80-0766, May 1980.

5. Abel, I., "An Analytical Technique for Predicting the Characteristics of a Flexible Wing Equipped with an Active Flutter Suppression System and Comparison with Wind-Tunnel Data", NASA TP 1367, 1979.
6. Nissim, E. and Lottati, L., "Active Control Systems for Flutter Suppression and Gust Alleviation in Supersonic Cruise Aircraft", AIAA paper 79-0792, April 1979.
7. Ch'en Ching-sung: "Principle and Method of Computing the Distribution of Wing Lift for Different Positions of the Aileron in Subsonic Flow", Hang Kung K'e Chi HK 79004, 1979.

STUDY ON LONGITUDINAL DYNAMIC CHARACTERISTICS OF PILOT-AIRPLANE SYSTEMS
- APPROACH TO THE METHOD FOR STUDYING PIO¹ PROBLEM -

Ch'en T'ing-nan Li Ch'un-chu
(Air Force College of Engineering)

ABSTRACT

In order to meet the needs for studying PIO (Pilot-Induced Oscillation) and take the serious influence of control system nonlinearity (e.g., clearance and friction, etc.) on PIO into account, a dynamic structure diagram (see Figure 2) and an analog structure diagram (see Figure 3) of longitudinal motion of pilot-control-airframe with nonlinearity have been derived. Moreover, computations have been carried out on a DMJ-3A analog computer for three cases as examples, i.e., the moment arm in normal state (short arm), the moment arm in troubled state (long arm), and the moment arm still in troubled state (long arm) without pilot's correction, for a fighter flying at low level and high speed. The results are shown in Figure 4, Figure 5 and Figure 6. It is obvious that they coincide with the actual flight and thereby it is proved preliminarily that the structure diagram and the analog structure diagram (i.e., the computation method for PIO) proposed are not only reliable, but also of value in practical analysis and use. The results obtained also demonstrate that the phenomenon of the longitudinal oscillation with big amplitude for a fighter at low level and high speed is the problem of PIO.

* Received in January 1982.

1) PIO: an abbreviation for Pilot-Induced Oscillation

In order to get a clear understanding of the influence of the pilot on the pilot-airplane system, different pilot's transfer functions have been adopted to compute the pilot-airplane system on the DMJ-3A analog computer. The results obtained prove that the mathematical model of the pilot exerts a great influence on the pilot-airplane system (see Figure 7).

We wish to thank Prof. Chao Chen-yen, Assist. Prof. Fang Ch'eng-Chin and Assist. Prof. Liu Ch'ien-kang for their guidance in this study.

I. PRESENTATION OF THE PROBLEM

Around the 1940's, because of improved performance and range of the flight of airplanes, there arose the problem of "pilot-induced prolonged or uncontrollable oscillation" [3], i.e., the so-called PIO. PIO is not a simple problem of stability of the airplane itself. As described in Reference [4], airplanes in which PIO occurred depended both on themselves and on the pilot at the control stick for stabilization. Therefore, this is a typical stability problem of a pilot-airplane combination.

At present, PIO has become an important problem affecting the performance of high-speed airplanes. It has aroused great interest, and is being studied at home and abroad. However, in the literature we have studied, the effect of nonlinearity has often been omitted. It has been clearly pointed out in Reference [3] that control system friction and flight path are also significant factors affecting PIO. Moreover, in some studies on PIO at home and abroad, no consideration has been given to the influence of the pilot. In others, the pilot's transfer function has been reduced to 1. This is not appropriate, either.

For example, some of the so-called "large-amplitude oscillations"² were actually due to the pilot's participation in the control.

In order to carry out a more accurate and realistic study of the PIO problem, i.e., the problem of stability of the pilot-control-airframe system, we have, through research on the structure and inter-relationship of the pilot, the control system and the airframe, presented a dynamic structure diagram of the longitudinal motion that includes nonlinearity. Computations have been carried out on a DMJ-3A analog computer.

II. CONSTRUCTION OF THE DYNAMIC STRUCTURE DIAGRAM OF THE LONGITUDINAL MOTION OF THE PILOT-CONTROL-AIRFRAME SYSTEM

The pilot controls the airplane chiefly by means of adjustment of attitude θ or overload Δn_y . We will discuss the case of control based on overload¹.

In this paper, discussion will be centered on the type of airplanes in which (1) the control before the power-assist unit is mass trimmed, wherefore

$$K_{n_y} \text{ (overload feedback gain)} \approx 0$$

$$K_{\ddot{\theta}} = K_{n_y} \frac{l_b}{g} \ddot{\theta} \text{ (}\ddot{\theta}\text{ feedback gain)} \approx 0, \text{ and}$$

2) "Large-amplitude oscillation" is a term used by the troops for large-amplitude longitudinal oscillation.

1) We plan to discuss the case of control based on attitude in another paper.

(2) the power-assist unit is irreversible, wherefore

$$K_{\alpha} (\alpha \text{ and } \phi \text{ feedback gain}) = 0.$$

Thus, the block diagram for the pilot-control-airframe system can be simplified to that shown in Figure 1.

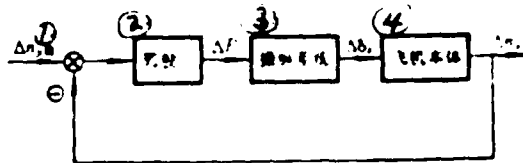


Figure 1. The man-machine block diagram of an aircraft whose control is mass trimmed and is of irreversible type.

Key: 1) $\Delta n, \delta$ input; 2) pilot; 3) control system; 4) airframe.

A. Mathematical Model of the Pilot

The study of the mathematical model of the pilot is a very complicated task. Much work has already been done at home and abroad. Specifically, the model should possess such characteristics as nonlinearity, delay, adaptation and self-adjustment[7]. In most cases, however, only one or a few of its characteristics have been stressed for the sake of simplicity. In this paper, we use the pilot's transfer function given in Reference [9]:

$$G_{\text{pilot}}(s) = \frac{K e^{-\tau s}}{1 + T s}$$

B. Mathematical Model of the Control System

The longitudinal control system refers to the entire system from the control stick to the elevator. It includes the control stick, connector rod, mass trim, moment arm, load mechanism, power-assist unit and the elevator. To simplify the computation, we make the following assumptions:

(1) The effect of gravity is negligible. Because gravity is basically a constant, it can only have a very small influence on equilibrium[8].

(2) Effect of mass (inertia) is considered for the elevator only. The reason is: for an aircraft whose control is mass trimmed and is of irreversible type, the overload has no effect on equilibrium. Moreover, in controlled motion, the acceleration is in general relatively small. Therefore, the inertia produced in the various control columns before the power-assist unit is negligible when compared to that produced by the load mechanism.

(3) The inertia produced in the elevator is regarded as an inertial load on the power-assist unit and therefore is added onto the values of the power-assist unit in the computation.

Based on the above assumptions, the structure diagram of the control system can be constructed sectionally.

1. From the control stick to the power-assist unit (including the load mechanism):

$$x_z = f(P_z, \text{flight path, friction})$$

$$x_1 = K_1 x_z$$

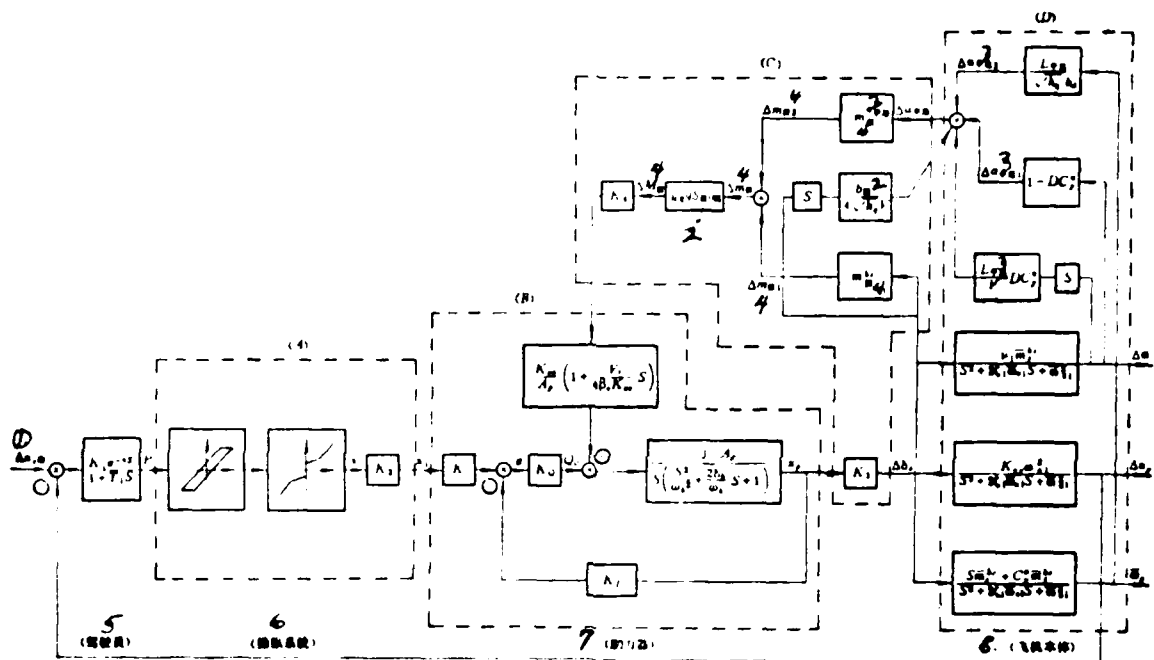


Figure 2. The dynamic structure diagram of longitudinal motion of pilot-control-airframe combined system.

Key: 1) Δn_y ; 2) rudder; 3) elevator; 4) shear; 5) pilot; 6) control system; 7) power-assist unit; 8) airframe.

In the above equations, x_2 is the displacement of the control stick, P_2 is the moment of the control stick, x_1 is the displacement of the forward-pull stick of the power-assist unit, and K_1 is the transfer ratio of the two displacements.

2. Power-assist unit:

From Reference [10], the dynamic structure diagram of the power-assist unit is as shown in (B) of Figure 2.

3. From the power-assist unit to the elevator:

The displacement x_p output by the power-assist unit causes the elevator to deflect. Besides serving as input to the airframe, the deflection of the elevator also has the following two effects.

(1) It produces an increment in the shearing moment in the elevator. This increment in moment is directly fed back to the power-assist unit.

(2) The angular velocity $\dot{\delta}_z$ of the deflection of the elevator gives rise to a certain resistance moment, which is also fed back to the power-assist unit. The magnitude of this moment can be calculated from the following relation:

$$\Delta M_{\text{resistance}} \approx 1/8 \cdot m_{\text{shear}}^2 \cdot \dot{\delta}_z^2 \cdot b_{\text{rudder}}^2 \cdot S_{\text{rudder}} \cdot \sqrt{k_q} \cdot V$$

The dynamic structure diagram for this portion is as shown in (C) of Figure 2.

C. Mathematical model of the airframe

As the problem of PIO is mainly associated with short-period modes, the transfer function of the airframe will also be expressed in terms of short periods.

The effects of the airframe are as follows. First, $\dot{\alpha}_y$ is produced as a result of the input $\dot{\alpha}_z$. This $\dot{\alpha}_y$ is to be fed back to the pilot. Secondly, the input of $\dot{\alpha}_z$ gives rise to $\dot{\alpha}_x$, $\dot{\alpha}_y$ and $\dot{\alpha}_z$, all of which will give rise to an increase in the angle of attack of the elevator $\dot{\alpha}_{\text{elevator}}$. This causes an increase $m_{\text{shear}}^{\text{elevator}}$ in the shearing moment.

The dynamic structure diagram of the airframe is as shown in (D) of Figure 2.

D. Dynamic structure diagram of longitudinal motion of the pilot-control-airframe system.

From the above analysis, the dynamic structure diagram of the pilot-control-airframe system should be as shown in Figure 2.

III. COMPUTATIONAL METHOD

It can be seen from Figure 2 that after the nonlinear factors of the pilot and the control system are introduced, the solution of the problem becomes very complicated. The authors used an analog computer to solve the problem presented in the structure diagram.

Based on Reference [11] and similar works, the dynamic structure diagram in Figure 2 can be transformed into the analog structure diagram shown in Figure 3. (The transfer coefficients given in the diagram correspond to those in the following computation.)

For the pure delay e^{-1S} , the authors have used the curve fitting method of Smith and Wood, taking

$$e^{-1S} \approx \frac{10 - 4.7\tau S + \tau^2 S^2}{10 + 4.7\tau S + \tau^2 S^2}$$

In addition, in order to increase the simulation accuracy for the friction characteristics, we have, on the basis of Reference [11], put two ratio devices in series.

For the equations used for obtaining the transfer coefficients in Figure 3, see Reference [2].

IV. EXAMPLES

The emphasis of this study is on the man-machine system stability of a fighter flying at low level and high speed under three typical conditions, namely

- (1) moment arm in normal state (short arm),
- (2) moment arm in troubled state (long arm),
- (3) moment arm still in troubled state (long arm), but without pilot's participation in correction.

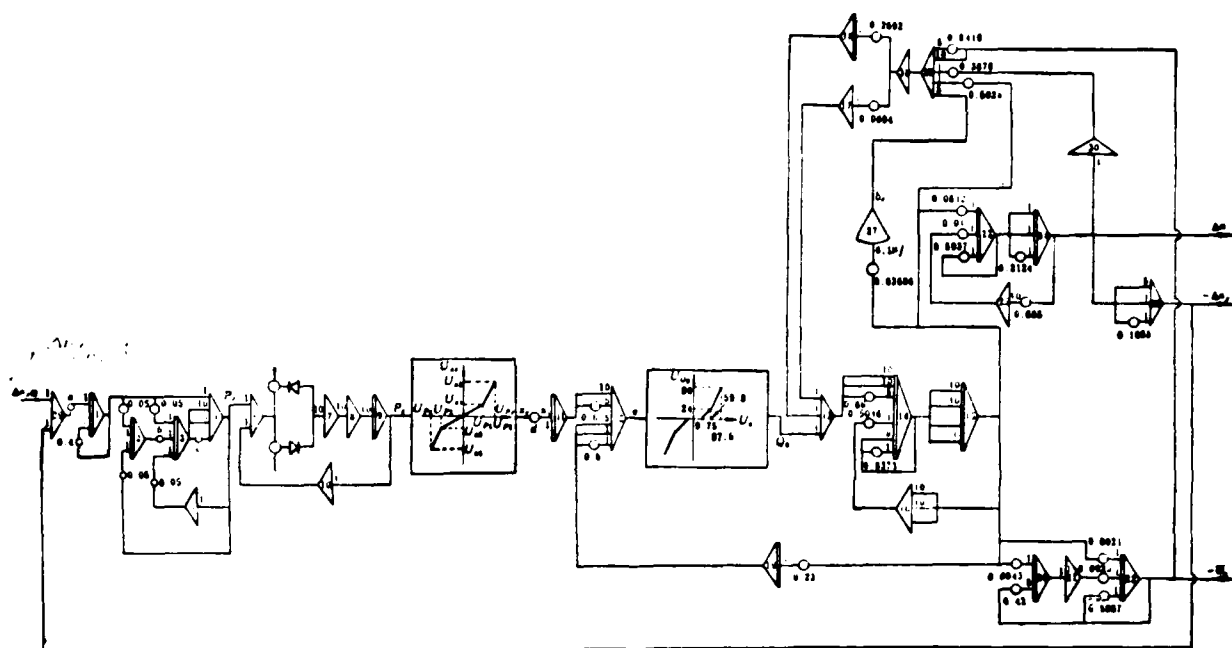


Figure 3. The analog structure diagram of a fighter at low altitude and high speed (H-2000m. M=0.9), and its moment arm in normal state (short arm) or in troubled state (long arm).

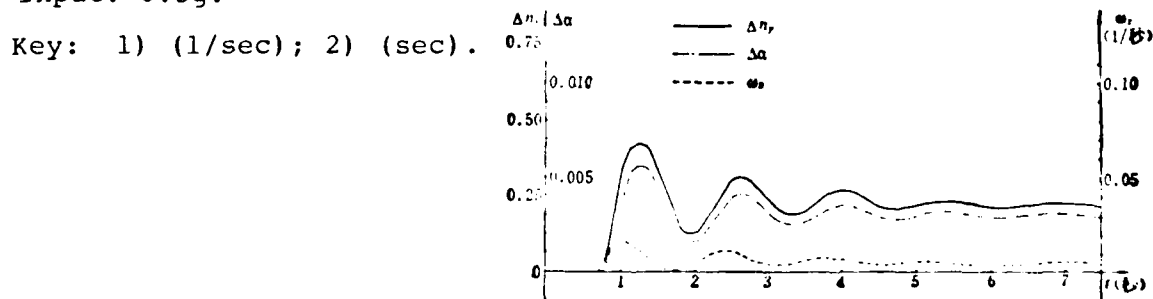
The analog structure diagram is basically the same for the case with the moment arm in normal state and that with the moment arm in troubled state, except that the values for the constant-coefficient parts a,b,c and d, and for the voltage and slope at deflection point on the general function representing the moment of the control stick are different (see Figure 3). The analog structure diagram for the case where the pilot does not participate in controlling the fighter can be obtained by making some changes in Figure 3. These are:

- (1) Cut the return part of the overload feedback.
- (2) Omit the pilot contribution.

The conditions for the computation are taken to be as follows. Level of flight $H=2000\text{m}$. $M=0.9$. Weight in flight $G=6652\text{ kg}$. Center of gravity located at $\bar{x}_T=0.41$.

The result of the computation for the case with the moment arm in normal state (short arm) is as shown in Figure 4, where the input $\Delta n_{\text{sh}}=0.5$.

Figure 4. The man-machine system output of a fighter with its moment arm in normal state (short arm).
Input: $0.5g$.



The result for the case with moment arm in a troubled state (long arm) is shown in Figure 5. It should be mentioned here that in this case there is rapid divergence. If the input is still taken to be $\Delta n_y = 0.5$, then the machine quickly becomes overloaded. We have reduced the input to $\Delta n_y = 0.025$ so as to be able to prolong the period before overload occurs and to get a clear picture of the process of divergence.

Figure 6 shows the result for the case with the moment arm still in troubled state but without pilot's correction. The input is still taken to be $\Delta n_{y_{input}} = 0.5$.

In order to see the effect of the pilot on the man-machine system, we also computed the man-machine stability under the condition in which the pilot's model was replaced by $G_{pilot}(s) = 1$. The result is shown in Figure 7.

From the curves obtained from the computation we see that for the fighter flying at low level and high speed:

(1) When the moment arm is in normal state (short arm), the man-machine system is stable. This is in agreement with the actual flight experience.

(2) When the moment arm is in a troubled state (long arm), the man-machine system is unstable. Divergence is rapid even for a very small input. (In the example, $\Delta n_{y_{input}}$ is only 0.025.) This is also in agreement with actual flight experiences.

(3) When the moment arm is in a troubled state (long arm) and the pilot does not participate in correction, the man-machine system is stable. This agrees with the pilot's experience.

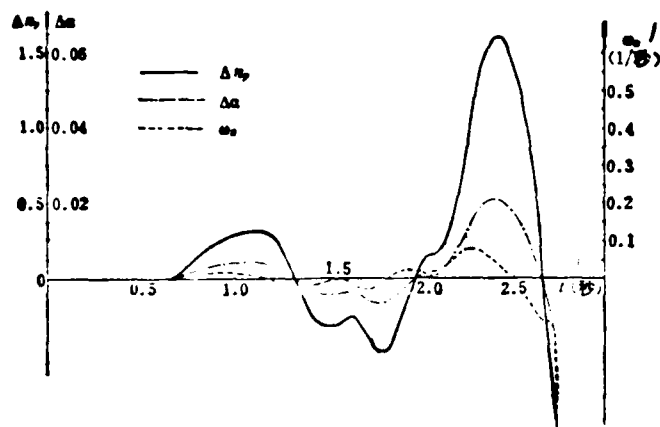


Figure 5. The man-machine system output of a fighter with its moment arm in troubled state (long arm). Input: 0.025g.

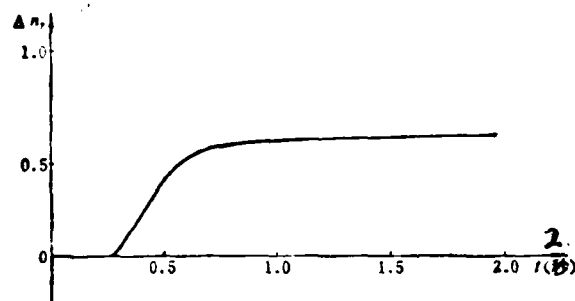


Figure 6. The output of a fighter without pilot's correction and its moment arm in troubled state (long arm). Input: 0.5g.

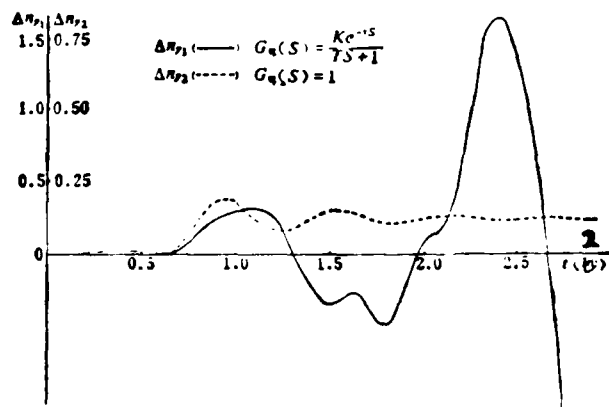


Figure 7. The effect of pilot's transfer function on the man-machine system.

Key to Figures 5,6,7: 1) (1/sec); 2) (sec).

(4) If, when the moment arm is in a troubled state (long arm), the pilot's transfer function is simplified to 1 (i.e., the effects of delay, inertia and amplification are omitted), then the man-machine system is stable. This obviously does not agree with what happens during actual flight.

V. CONCLUSIONS

The following conclusions can be drawn from the simulation computations:

1. The structure diagram derived and simplified by the authors for a man-machine system that includes the nonlinear factors of the pilot and the control system can be used in the study of PIO. Not only is the computation method relatively simple, but the results are also very reliable.

2. The authors believe that the large-amplitude oscillation breakdown that occurred to a certain fighter while it was flying at low level with the moment arm at long arm was a PIO problem. The divergence of the oscillation under such conditions was entirely due to the pilot. If the pilot had not participated in the correction then the airframe would have been stable.

3. There is a fundamental difference between the stability of the airframe and the stability of the closed-loop including the pilot.

4. The pilot's transfer function has a large effect on the computation of man-machine stability.

REFERENCES

1. Ch'en T'ing'nan, Li Ch'un'chu: "Study of the Dynamic Structure Diagram of the Longitudinal Motion of the Pilot-Control-Airframe System", K'ung Chun Kung Ch'eng Hsueh Yuen Hsueh Pao, No. 1, 1981.
2. Ch'en T'ing-nan, Li Ch'un-chu: "Simulation Computation and Analysis of the Longitudinal Motion of the Pilot-Control-Airframe System", K'ung Chun Kung Ch'eng Hsueh Yuen Hsueh Pao, No. 1, 1982.
3. Background Information and User Guide for MIL-F-8785 B (ASG), "Military Specification-Flying Qualities of Piloted Airplanes" AFFDL-TR-69-72.
4. Ralph, H. Smith, "A Theory for Longitudinal Short-period Pilot Induced Oscillations", AFFDL-TR-77-57.
5. Neal. T. Peter and C.R. Chalk, "Revision of Military Specification MIL-F-8785 B (ASG) Flying Qualities of Piloted Airplanes" 1971.
6. "Analysis of Breakdown of Elevator Control System", Air Force Command Center, 1970.
7. Stanley M. Shinnars, "A Guide to Systems Engineering and Management", 1976.
8. Etkin, "Dynamics of Atmospheric Flight", 1972.
9. V.A. Bodner, M.S. Kozlov. Stabilization of aircraft and autopilots, 1961.
10. Herbert E. Merritt, "Hydraulic Control Systems", 1967.
11. Chou Yen-hsun et al: "Technique of Simulation and Mixed-Simulation Computations", Kuo Fang Kung Yeh Publishing House, 1980.
12. A.A. Lebedev, L.S. Chernobrovkin. Dynamics of flight of unmanned aircraft, 1962.

STATISTICAL DETERMINATION OF A FLAW DETECTION PROBABILITY CURVE

Lin Fujia and Huang Yushan

(Northwestern Polytechnical University)

Abstract

The reliability prediction and damage tolerance analysis of aircraft structures based on the principles of fracture mechanics require the knowledge of the ability of flaw detection. A statistical method for determining the flaw detection probability curve is developed and a test technique for obtaining independent flaw detection data is described in this paper. Based on these data and a formula proposed in this paper, the confidence lower limit of the flaw detection probability with the given confidence level for an arbitrary size of a sample and for an arbitrary value of the detection probability can be calculated merely with the help of the table of F-distribution. The presented formula occurs exactly and simply in comparison with other approximate formulas proposed by some authors.

As an example, the flaw detection probability curve with 95% confidence is given, which comes from the results of inspecting corner flaws at holes in 50 specimens. The specimens were made of steel 45 and the magnetic-particle technique was applied for non-destructive inspection.

Finally, the simplified method for determining the flaw detection probability curve is also discussed.

STATISTICAL DETERMINATION OF A FLAW DETECTION
PROBABILITY CURVE

/21

Lin Fujia and Huang Yushan

(Northwestern Polytechnical University)

ABSTRACT

This paper describes a method for obtaining and manipulating data for determining the flaw detection probability curve. A formula is given for the lower confidence limit that is accurate and simple. Results of actual tests have been included. A simplified method for determining the flaw detection probability curve is also discussed.

I. Introduction

In the design of aircraft structure damage tolerance based on the principles of fracture mechanics, it is necessary to calculate and predict the extent of the spread of the flaw. In engineering practices, the initial length a_i of the flaw, which is an important determining factor of the flaw spread, is sometimes determined on the basis of the reliability of flaw detection. For example, it is stated in the U.S. Military Specifications on "Aircraft Damage Tolerance Requirements" [1]* that all flaws larger than a_i must have a detection probability of 90% at the 95% confidence level. Obviously, to determine a_i by this method, one needs to determine a detection probability curve experimentally that corresponds to the confidence level $1 - \alpha$. This is the curve representing the variation of detection probability with the length of the flaw a , i.e., the $P_L(D/a) \sim a$ curve.

*Received in October 1981.

In the prediction of the reliability and economic life of an aircraft structure, it is sometimes necessary to know the distribution of flaws that have escaped detection. Here also, one has to make use of the $P_d = 1 - \exp(-\lambda L)$ curve. [2, 3, 4]

Tests have shown that, besides the type of method used for nondestructive testing, factors affecting the flaw detection probability include material characteristics, shape and position of flaw, surface smoothness of the structural part containing the flaw, work environment, illumination and the competence and attitude of the inspection personnel. The example given in this paper further shows that, if the position and direction where the flaw is likely to occur is known (such conditions exist in aircraft structures), then there will be an appreciable increase in the detection probability. Hence, in the damage tolerance design and reliability analysis of aircraft structures, it is not sufficient just to know the detection probability curve for a certain nondestructive testing method under a certain given condition. To reliably predict the life and breakdown probability of a structure, one must determine the detection probability curve taking all practical conditions into consideration.

However, at present there is a lack of such curves and standard procedures to follow in their determination. In this paper, a method for obtaining and manipulating data for determining this type of curve is presented. The feasibility of this method has been demonstrated through actual tests.

II. Method for Obtaining Data for Flaw Detection

First, to simulate actual conditions, prepare a given number of specimens with flaws of different lengths. (In the case where a sufficient number of actual structural parts containing flaws

are available, it is not necessary to take this step.) To simulate actual conditions means to ensure that the specimens are as close to the actual structural parts as possible in material, surface smoothness, shape of the region containing the flaw and the type of flaw. Then, use the specified non-destructive testing method to do repeated tests under the specified conditions (including work environment, illumination, technical competence of the inspection personnel, etc.), thus obtaining the number of flaws detected and the numbers of flaws that have escaped detection. /22

To be sure that representative and independent tests are done, the total number of specimens should not be less than 30, and half of the specimens should be free of flaws. The number of inspectors should not be less than 5. Each assignment of detection to each inspector should be completed independently. In the example given later in this paper, we have proposed several practical methods for ensuring the independence of the detection results.

A key problem in detection lies in the determination of the number of flaws that have escaped detection. The number of independent detections K of a flaw and the number of times the same flaw has escaped detection J are important data in the statistical analysis. K can be obtained directly. To determine J , one must first decide if the "flaw" actually exists. Experiments show that the following two methods lend themselves well to the solution of this problem:

1. Appropriately increase the number of independent detections K . If we assume that for a certain flaw α the detection probability $P(D|\alpha) = p$, i.e., $0 < p < 1$. The probability of escaping detection $q = 1 - p < 1$, and thus the probability of K independent detections all escaping detection is q^K . Obviously, when K is large, q^K is very small. Therefore, theoretically speaking, the flaw will

certainly be detected if a sufficient number of detections are performed on the same flaw.

2. Apply a fixed static pull (equivalent to half of the load of the prepared flaw) to the specimen, and carry out the detection under this condition, so as to render the flaw more visible. This method allows an effective determination of the existence of the flaw as well as a relatively accurate determination of the length of the flaw.

III. Statistical Analysis of the Detection Data

First, divide the lengths of the flaws into several ranges. Use the largest value in each range to represent the lengths of the flaws in that range, and fill in the detection data accordingly. Then, determine the detection probability for each single-flaw-length range in the following manner.

Each detection can have only one of two possible results: either the flaw is detected or it is not. Assume the probability of detection $P(D/\alpha) = p$, and the probability of not detecting the flaw $P(\bar{D}/\alpha) = q = 1 - p$. Thus, the binary distribution is obeyed by the number S of flaws detected when n independent detections are carried out for the flaws in the same flaw length range, and one has

$$P_n(S = S_n) = C_n^{S_n} p^{S_n} q^{n-S_n} \quad (1)$$

In the equation, p is unknown. Its point estimate is $\hat{p} = S_n/n$. To be on the safe side, it is usually required to find the lower confidence limit p_L of p in accordance with the specified confidence level $1 - \alpha$. The probability condition that needs to be satisfied is

$$P\{S \geq S_n\} = \sum_{i=S_n}^n C_n^i p_L^i (1-p_L)^{n-i} = \alpha \quad (2)$$

In general, tables of cumulative binary distribution list values for up to $n = 30$ only, and do not meet our needs. In Refs. [5] and [6], the usual approximation method is used; i.e., when n exceeds 30 and p approaches 0 or 1, Poisson's distribution is used to carry out an approximate calculation of p_L ; and when p has an intermediate value and n is very large, after a definite transformation, the normal distribution is used to carry out approximate calculation of p_L . For example, for $n = 45$, $S_n = 43$, $\alpha = 0.05$, the value of p_L as calculated using the above approximation is 0.894. The exact solution satisfying Eq. (2) is 0.867. The difference is 0.027, which may not be neglected in the region of high detection probability, as this is the region very closely related to structure safety. Moreover, this method of approximation is not very convenient to use. In this paper, the value of p_L satisfying Eq. (2) is found by merely using the table of F-distribution and the following exact and simplified equation:

$$p_L = \frac{f_2}{f_1 + f_2 x} \quad (3)$$

In the equation, the upper degree of freedom of the F-distribution $f_1 = 2(n - S_n + 1)$; the lower degree of freedom of F-distribution $f_2 = 2S_n$; x , the upper percentage point of the F-distribution, is found from the F-distribution according to the following equation:

$$P\{F > x\} = \alpha \quad (4)$$

We prove Eq. (3) as follows:

$$\text{Let } \Gamma(x) = \int_0^{\infty} t^{x-1} e^{-t} dt \text{ — } \Gamma \text{ function,}$$

$$I(y, \gamma, \theta) = \frac{B_y(\gamma, \theta)}{B(\gamma, \theta)} \text{ — Beta distribution function with } \gamma \text{ and } \theta \text{ as parameters,}$$

$$B(\gamma, \theta) = \int_0^1 t^{\gamma-1} (1-t)^{\theta-1} dt = \frac{\Gamma(\gamma) \Gamma(\theta)}{\Gamma(\gamma + \theta)} \text{ — Beta function,}$$

$$B_y(\gamma, \theta) = \int_0^y t^{\gamma-1} (1-t)^{\theta-1} dt \text{ — incomplete Beta function.}$$

In the above, $0 \leq y \leq 1$; $\gamma, \theta > 0$.

The probability density function for an F-distribution with given degrees of freedom f_1 and f_2 is

$$p(x, f_1, f_2) = \frac{\Gamma\left(\frac{f_1+f_2}{2}\right)}{\Gamma\left(\frac{f_1}{2}\right)\Gamma\left(\frac{f_2}{2}\right)} f_1^{\frac{f_1}{2}} f_2^{\frac{f_2}{2}} \frac{x^{\frac{f_1}{2}-1}}{(f_2+fx)^{\frac{f_1+f_2}{2}}} \quad (x > 0)$$

Transforming into an equation in the variable

$$Y = \frac{f_1 F}{f_2 + f_1 F}$$

one can deduce that Y obeys the Beta distribution with parameters

$$\gamma = \frac{f_1}{2}, \quad \theta = \frac{f_2}{2}, \quad \text{i.e.,}$$

$$P\{Y \leq y\} = I\left(y, \frac{f_1}{2}, \frac{f_2}{2}\right)$$

From the relation between F and Y, one readily obtains

$$P\{F > x\} = I\left(\frac{f_2}{f_2 + f_1 x}, \frac{f_2}{2}, \frac{f_1}{2}\right) \quad (5)$$

On the other hand, one can prove by repeated integration by parts that

$$\sum_{i=S_0}^n C_i^s p_i^i (1-p_i)^{n-i} = n C_{n-1}^{s-1} \int_0^{p_n} t^{s-1} (1-t)^{n-s} dt$$

It is easily seen that

$$n C_{n-1}^{s-1} = \frac{1}{B(S_0, n-S_0+1)}$$

Therefore,

$$\sum_{i=S_n}^n C_n^i p_L^i (1 - p_L)^{n-i} = I(p_L, S_n, n - S_n + 1) \quad (6)$$

By letting

$$\frac{f_1}{2} = n - S_n + 1, \quad \text{i.e., } f_1 = 2(n - S_n + 1), \quad \text{and}$$

$$\frac{f_2}{2} = S_n, \quad \text{i.e., } f_2 = 2S_n$$

and comparing Eqs. (5) and (6), one can see that if x satisfies Eq. (4), i.e., $P\{F > x\} = \alpha$, then the value of p_L calculated from Eq. (3) must satisfy Eq. (2), Q.E.D.

/24

The $P(D/\alpha)$ vs. α and $P_L(D/\alpha)$ vs. α curves are obtained by plotting the results of statistical analysis of inspection data for each flaw-length region.

IV. Example

We used 45# steel to make 50 specimens with dimensions as shown in Fig. 1. Cracks were prepared by means of a high-frequency fatigue tester. Half of the specimens were kept crack-free, while the rest contained cracks of different lengths. Inspection was carried out by means of the magnetic particles method. To ensure the independence of the test results, the following requirements were imposed on the inspection process:

- (1) The results of the inspection were recorded by a specially designated person. The 8 inspectors did their jobs separately without exchanging information or discussion.

- (2) All the specimens had to have the same external appearance, without any noticeable marks on their surfaces.
- (3) Two separate inspections of the same specimen by the same inspector had to be spaced by at least two days in time.

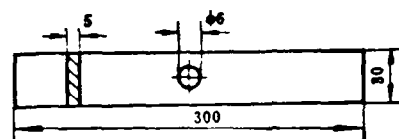


Figure 1. Specimen configuration.

Data analysis of the results of inspection is given in Table 1. The results are plotted in Figure 2. Flaw length refers to the length of the crack along the surface of the specimen.

Table 1. Analysis of the results of flaw detection ($1 - \alpha = 95\%$)

Key: 1) Flaw-length range (mm); 2) Total number of flaws;
 3) Number of flaws detected; 4) Point estimate of detection probability; 5) Upper degree of freedom in the F-distribution;
 6) Lower degree of freedom in the F-distribution; 7) Upper percentage point of the F-distribution; 8) Lower confidence limit of detection probability.

1 裂纹长度区间 (毫米)	2 总数	3 检出数	4 $\hat{p} = \frac{S_n}{n}$	5 F 分布的上自由度 $f_1 = 2(n - S_n + 1)$	6 F 分布的下自由度 $f_2 = 2S_n$	7 F 分布的上侧百分位点 x $P\{F > x\} = \alpha$	8 检测概率的置信下限 $P_L = \frac{f_2}{f_2 + f_1 x}$
0.41~0.60	513	158	0.308	712	316	1.18	0.273
0.61~0.80	264	152	0.576	226	304	1.23	0.522
0.81~1.00	111	95	0.856	34	190	1.49	0.789
1.01~1.20	157	141	0.898	34	282	1.47	0.849
1.21~1.40	191	175	0.916	34	350	1.46	0.876
1.41~1.60	225	213	0.947	26	426	1.52	0.915
1.61~1.80	176	169	0.960	16	338	1.68	0.926
1.81~2.00	65	65	1.000	2	130	3.07	0.953

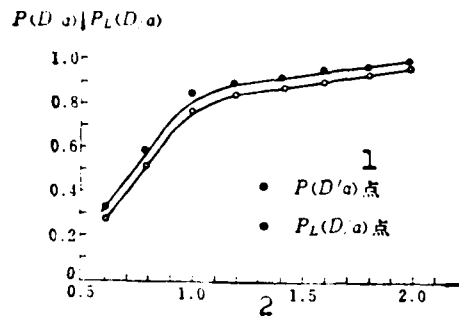


Figure 2. $P(D/a)$ vs. a and $P_L(D/a)$ vs. a curves obtained from inspection data.

Key: 1) Point; 2) (mm).

As the position and direction of the cracks in the given example /25 were definite and as expected, detection probability was rather high.

V. The Form of the $P(D/a) \sim a$ Curve and the Simplified Detection Method

As it takes a lot of time and manpower to do a thorough determination of the flaw detection probability curve, we propose a simplified engineering method. The basic idea is to make use of available information besides the data obtained for the present inspection. First, determine the form of the $P(D/a) \sim a$ curve and some of the parameters, based on given information. Then, take a few specimens (about 10), and carry out the inspections in one or two of the flaw-length regions. The remaining parameters can be estimated from the results obtained. Ref. [8] contains the experimental curves showing the ability of four nondestructive testing methods to detect surface cracks. The detection results given in this paper for using the magnetic particles method for detecting cracks can

also serve as a useful reference. Following is a discussion of three forms of $P(D/a) \sim a$ curve.

1. The power-expansion form used by Yang-Trapp [2]

$$P(D/a) = \begin{cases} \left(\frac{a - a_1}{a_2 - a_1} \right)^m, & a_1 \leq a \leq a_2 \\ 0, & a < a_1 \\ 1, & a > a_2 \end{cases}$$

a_1 , a_2 and m are constants to be determined. The physical meaning of a_1 and a_2 is obvious. Therefore, these two constants can be determined empirically. Thus, only m needs to be determined from experiments performed under given conditions. Note that as a_2 has a larger effect on the results, one should be conservative in choosing its value.

2. The exponential form used by Davidson [3]

$$P(D/a) = \begin{cases} 0, & a \leq a_0 \\ c_1 \{ 1 - \exp[-c_2(a - a_0)] \}, & a > a_0 \end{cases}$$

c_1 , a_0 and c_2 are constants to be determined. c_1 is very close to 1, and can be chosen in advance (e.g., $c_1 = 0.98 \sim 0.99$). The reason that c_1 is not set equal to 1 is due to the fact that even very long cracks can sometimes be overlooked in an inspection. a_0 has a definite physical meaning, and can be determined empirically. Thus, only c_2 needs to be determined through the detection process.

3. The Weibull probability distribution used by Heller-Stevens [9]

$$P(D/a) = 1 - \exp\left[-\left(\frac{a}{c}\right)^b\right], \quad a > 0$$

In this equation, b and c are the undetermined constants. As an engineering approximation, one can assume that b is the same for

the same nondestructive testing method. Only c needs to be determined experimentally. An advantage of this type of function is that it reflects the fact that even very small cracks can sometimes be detected, while it is sometimes possible to overlook a very large crack.

It remains to be determined which of the above three forms best describes the actual situation. As far as curve fitting is concerned, as the first two forms contain more parameters which can be estimated from a set of data obtained in the experiment, they can perhaps be better fitted to the experimental data. Table 2 gives the results of fitting these three forms of functions to the data obtained for our example. The residual standard deviations are given for the purpose of comparison. Figure 3 gives the three fitted curves.

As in the engineering approximation mentioned above, only one parameter needs to be experimentally determined for any of the forms; the multiple-parameter fitting feature of the first two forms is no longer an advantage. In this case, choosing the third form simplifies the plotting process as one can do it on the readily available Weibull probability paper.

/26

1 函 数 型 式	4 YANG-TRAPP型	4 DAVIDSON型	4 WEIBULL型
2 参数估计值	$a_1 = 0.59 \text{ 毫米}^5$ $a_2 = 1.82 \text{ 毫米}^5$ $m = 0.246$	$a_0 = 0.53 \text{ 毫米}^5$ $c_1 = 0.99$ $c_2 = 3.43 \text{ 毫米}^{-1} 6$	$b = 2.06$ $c = 0.87 \text{ 毫米}^5$
3 剩余标准差	0.058	0.050	0.061

Table 2. The Results of Least Square Analysis.

Key: 1) Functional Form; 2) Estimated Value of Parameter; 3) Residual Standard Deviation; 4) Form; 5) mm; 6) mm^{-1} .

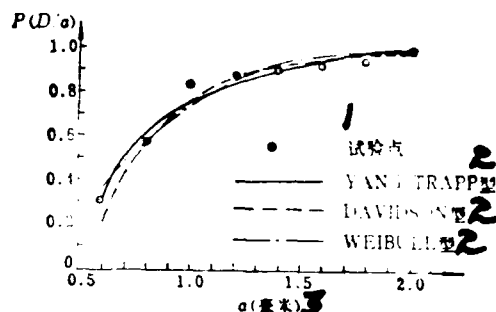


Figure 3. Three Types of $P(D/a)$ vs. a curve.

Key: 1) Experimental point; 2) Form; 3) (mm).

VI. Conclusion

Every nondestructive testing method has a certain range of sensitivity. Methods that are effective in the range of short crack lengths may have decreased sensitivity in the range of long crack lengths [8]. Therefore, while using a particular method, one must bear in mind the range of effectiveness of the flaw detection probability curve.

Many nondestructive testing methods have their flaw detection ability based on the area of the flaw. In this case, the statistical method of this paper is still applicable if the flaw length is replaced by the area of the flaw.

Many of the comrades of the former Room 504 of Northwestern Polytechnical University participated in the experimental work of this paper. We thank them all.

References

1. U.S. Military Specifications: Aircraft Damage Tolerance Requirements (MIL-A-83444 (USAF) 1974. 7.2), Aeronautical Technology Abroad, No. 69, 1977.
2. J. N. Yang and W. J. Trapp, Reliability Analysis of Aircraft Structures under Random Loading and Periodic Inspection, AIAA.J. Vol. 12, No. 12, Dec. 1974.
3. J. R. Davidson, Reliability and Structural Integrity, NASA TM X-71934, Nov. 1973.
4. J. N. Yang, Statistical Estimation of Economic Life for Aircraft Structures, J. Aircraft Vol. 17, No. 7, July, 1980.
5. P. F. Packman, J. K. Malpani, F. M. Wells, Probability of Flaw Detection for Use in Fracture Control Plans, Strength and Structure of Solid Materials, Tokyo, 1976, 127-143.
6. J. K. Malpani, Reliability of Flaw Detection by Nondestructive Inspection and Its Application to Future Mechanics Design /27 and Life Analysis, D. Phil. Thesis, University of Vanderbilt, 1976.
7. A. Hald, Statistical Theory with Engineering Application, New York, 1955.
8. P. F. Packman, H.S. Pearson, J. S. Owens, and G. Young, Definition of Fatigue Cracks through Nondestructive Testing, J. Materials, Vol. 4, No. 3, Sept. 1969.
9. R. A. Heller and G. H. Stevens, Bayesian Estimation of Crack Initiation Time from Service Data, J. Aircraft, Vol. 15, No. 11, 1978.

MULTI-LEVEL SUBSTRUCTURAL ANALYSIS IN MODAL
SYNTHESIS -- TWO IMPROVED SUBSTRUCTURAL
ASSEMBLING TECHNIQUES

Liu Guoguang and Li Junjie
(Aircraft Structural Mechanics Research Institute)

Zhang Dewen penned
(Beijing Institute of Structure and Environment Engineering)

Abstract

Most of the prevalent modal synthesis methods [1-10] are referred¹ to as "single level synthesis." Their application to dynamic analysis of large complex structures may be limited by computer capacity. Two improved substructural assembling techniques, called "multi-level synthesis" and "successive synthesis," are presented in order to raise computation efficiency and to be available for calculation of large structures on a computer with small interior capacity. In the present paper the "rigid substructure technique" [11] is also employed.

A typical example has been calculated with satisfactory results. Numerical calculations show that the accuracies of the two improved assembling methods are trustworthy provided the frequency criterion proposed in this paper is adopted.

I. Introduction

/28

The substructure model synthesis established by Hurty [1] is one of the methods of substructural dynamic analysis. It has made possible the calculations of dynamics of large

1. Received August 1981.

structures using a computer with limited capacity. At the same time, it ensures the independence of the design, modification and tests of the parts.

The emphasis of the "fixed-interface methods" [1, 2] and the "free-interface methods" [3-6] that have been prevalent for many years has been on the choice of the substructure (static or dynamic) modes. The assembling of substructures has remained in the stage of "single-level synthesis." This type of assembling method is still subject to limitation by the capacity of the computer. In this paper, two improved assembling techniques, called "multi-level synthesis" and "successive synthesis," are proposed. These techniques can lower the requirement on the interior capacity of the computer, and make it possible to do calculation of large structures on a computer with small interior capacity. Moreover, computation efficiency is thereby increased. In particular, when the substructures are appropriately subdivided, the successive synthesis method can reduce the bandwidth of the stiffness matrix and the mass matrix.

Because of limited space here, only the important points of the "multi-level synthesis" and "successive synthesis" will be described in terms of the "pseudo-fixed-interface" mode [7, 8] of the free-interface method. Some derivations will be omitted. For the "rigid substructure technique" and related equations, please see Ref. [11]. For the "pseudo-structure analysis" used for free substructures, please see the HAJIF-I¹ Theory Handbook to be published, as the method presented in this paper has already been adopted by HAJIF-I.

1. HAJIF-I is an abbreviation for "Aeronautical Structural Dynamic Analysis Systems."

II. Improved Assembling Method I -- "Multi-Level Synthesis"

The so-called "multi-level synthesis" is an extension in concept of the "single-level synthesis" and a further abstraction in the general coordinates.

In Figure 1, 1-5 represent the elastic substructures, and 1 and 2 represent the rigid substructures. The system shown in Figure 1 can be analyzed dynamically using the tree-type substructure system given in Figure 2. In the following, let $\langle p, r \rangle$ denote the r th substructure of the p th level. The rigid parts can be treated as individual substructures rather than as belonging to the neighboring elastic substructures. (See Ref. [11] for the advantage and method of this approach.)

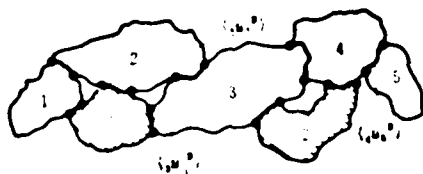


Figure 1. A general structure system.

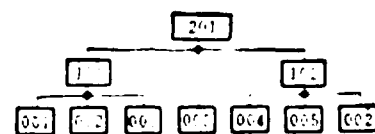


Figure 2. A multi-level (tree-type) substructure system.

First, we use the method of finite element analysis to establish the direct equation of motion of the elastic substructure r of the 0th (original) level:

$$\begin{bmatrix} m_r^{BB} & m_r^{BI} \\ m_r^{IB} & m_r^{II} \end{bmatrix} \begin{Bmatrix} \ddot{u}_r^B \\ \ddot{u}_r^I \end{Bmatrix} + \begin{bmatrix} k_r^{BB} & k_r^{BI} \\ k_r^{IB} & k_r^{II} \end{bmatrix} \begin{Bmatrix} u_r^B \\ u_r^I \end{Bmatrix} = \begin{Bmatrix} R_r^B \\ 0 \end{Bmatrix} \quad (1)$$

The superscripts B and I denote interface and interior, respectively. R_r^B is the interface reaction force.

Based on the Rayleigh-Ritz analysis, we use the auxiliary mode $\{G_h\}$ and the principal mode $\{\tilde{x}_r^N\}$ of the free interface to describe the displacement $\{u_r\}$ in the free-interface method. From Refs. [3-6] we know that

$$[G_h]_r = [G]_r - [\tilde{x}_{er}^N][e]_r^{-1}[\tilde{x}_{er}^N]^T = \begin{bmatrix} G_r^{BB} & G_r^{BI} \\ G_r^{IB} & G_r^{II} \end{bmatrix} \quad (2)$$

In the equation, $[\tilde{x}_{er}^N]$ is the set of elastic modes in $\{\tilde{x}_r^N\}$, with the corresponding eigenvalue matrix

$$[\Omega_e]_r = [\lambda_1 \quad \lambda_2 \quad \dots \quad \lambda_n]_r \quad (3)$$

The subscript n is the number of reserved elastic modes. To calculate the complete flexibility matrix $[G]_r$, apply the "pseudo-method" to the free interface substructures.

The principle mode $\{\tilde{x}_r^N\}$ is a set of low order eigenvectors taken from the characteristic equation of Eq. (1) according to the criterion

$$\omega_r = (\alpha)^{P-p} \omega_{\max} \geq \omega_r \quad (4)$$

We require $\{\tilde{x}_r^N\}$ to be normalized. In Eq. (4), α is determined as a statistical parameter. The exponent P denotes the total "level" number, while p denotes the "level" at which the substructures undergoing synthesis are found. ω_{\max} is the maximum accurate angular frequency of the entire structure that one desires to obtain.

Based on the free-interface method given in Refs. [3-8], neglecting residual inertia, we assume that

$$\{u_i\} = \{G_i^R\} \{R^R\} + \{\tilde{\Phi}_i^N\} \{p_i^N\} \quad (5)$$

According to Ref. [5] and Ref. [6], by starting out from Eq. (5), one can eliminate entirely the components along the interface coordinates, in the general coordinates described below. However, in order to unify the synthesis schemes of the free-interface and fixed-interface methods so as to simplify the procedure, we change Eq. (5) into one in the "pseudo-fixed-interface" mode:

$$\{u_i\} = \{\tilde{\Phi}_i^C : \tilde{\Phi}_i^N\} \left\{ \begin{array}{c} u_i^C \\ p_i^N \end{array} \right\} = \{\Phi_i\} \{p_i\} \quad (6) \quad / \underline{30}$$

In the equation, $\{\tilde{\Phi}_i^C\}$ and $\{\tilde{\Phi}_i^N\}$ are named "pseudo-restricted mode" and "pseudo-fixed-interface principal mode," respectively. Then, the equation of motion in the general coordinates $\{p_i\}$ is obtained by the usual method. For the equations involved, see Refs. [7] and [8].

Now, take several "0th" level substructures to assemble a "1st" level substructure $\langle 1, r \rangle$. Take the synthesized coordinates of $\langle 1, r \rangle$ to be

$$\{q_{\langle 1, r \rangle}\} = [\tilde{q}_{\langle 1, r \rangle}^T \ p_1^{TT} \ \dots \ p_r^{TT} \ \dots \ p_s^{TT}]^T \quad (7)$$

The superscript T denotes matrix transformation. $\{\tilde{q}_{\langle 1, r \rangle}^B\}$ is made up of $\{u_1^I\} \ \dots \ \{u_r^I\}$ and independent components in $\{u_1^B\} \ \dots \ \{u_s^B\}$. From geometric considerations, we have

$$\{p_i\} = [T_i] \{q_{\langle 1, r \rangle}\} \quad (8)$$

$$\{u_i^B\} = [T_i^B] \{q_{\langle 1, r \rangle}\} \quad (9)$$

from which we can write

$$\{u_r^B\} = [T_r^B] \{\tilde{q}_{<1,r>}^B\} \quad (10)$$

$$\{u_r^B\} = [T_r^B] \{\tilde{q}_{<1,r>}^B\} \quad (11)$$

We give [T] the general term of "assembling matrix." To clarify how we arrived at Eqs. (10) and (11), we use the substructures 4 and $\hat{2}$ in <1, 2> of Fig. 2 as examples:

$$\begin{Bmatrix} u_3^B \\ u_4^B \\ u_2^B \end{Bmatrix} = \begin{bmatrix} 0 & I & 0 \\ 0 & 0 & I \\ \frac{1}{2}D_4 & 0 & 0 \end{bmatrix} \begin{Bmatrix} u_2^I \\ u_3^B \\ u_5^B \end{Bmatrix} = [T_4^B] \{\tilde{q}_{<1,r>}^B\} \quad (12)$$

$$\begin{Bmatrix} u_3^B \\ u_4^B \end{Bmatrix} = \begin{bmatrix} \frac{1}{2}D_4 & 0 & 0 \\ \frac{1}{2}I & 0 & 0 \end{bmatrix} \begin{Bmatrix} \frac{1}{2} \\ u_3^B \\ u_5^B \end{Bmatrix} = [T_2^B] \{\tilde{q}_{<1,r>}^B\} \quad (13)$$

For the definition of $[\frac{1}{2}D_r]$ see Ref. [11]. $\{u_r^B\}$ is the column vector of the $\hat{r} \sim r$ interface coordinates.

We have, based on the concept of the generalized Ritz method described above, the displacement of the assembled substructure <1, r> in terms of the displacement functions that are continuous only in each original substructure. Now, we derive the stiffness matrix and mass matrix of <1, r> from its strain energy and kinetic energy, respectively, and obtain

$$[K_{<1,r>}] = \sum_r [T_r]^T [\hat{k}_r] [T_r] \quad (14)$$

$$[M_{<1,r>}] = \sum_r [T_r]^T [\hat{m}_r] [T_r] + \sum_r [T_r]^T [\hat{m}_r^{**}] [T_r] \quad (15)$$

To avoid having to handle a great number of null elements, one should use the expanded forms of Eqs. (14) and (15) in the computation using the computer. One can also execute Eqs. (14) and (15) according to the finite element assembling procedure. Band-shaped $[K_{\langle 1,r \rangle}]$ and $[M_{\langle 1,r \rangle}]$ can be obtained from the latter. Note that the second term of Eq. (15) can be obtained without going through matrix operations, but merely by placing $[m_r^{II}]$ at the correct position in $[M_{\langle 1,r \rangle}]$ -- the position corresponding to $\{u_r^I\}$.

It is easy to obtain from the principle of virtual work the ^{/31} interface reaction force of the assembled substructures, $\{R_{\langle 1,r \rangle}\}$. Thus, the equation of motion of $\langle 1,r \rangle$ is

$$[M_{\langle 1,r \rangle}]\{\ddot{q}_{\langle 1,r \rangle}\} + [K_{\langle 1,r \rangle}]\{q_{\langle 1,r \rangle}\} = \{R_{\langle 1,r \rangle}\} \quad (16)$$

Regard Eq. (16) as the direct equation of motion of substructure $\langle 1,r \rangle$ of the "1st" level, and make subdivisions similar to Eq. (1). Then, analyze the static and dynamic modes of all the "1st" level substructures in the manner the "0th" level substructures were analyzed, and take several "1st" level substructures to assemble a "2nd" level substructure. The analysis is the same as before except that one has to replace r and $\langle 1,r \rangle$ with $\langle 1,r \rangle$ and $\langle 2,r \rangle$, respectively, and to formally eliminate from the right-hand side of Eq. (15) the second term that is associated with rigid substructures (on the premise that all the rigid substructures have been assembled into the "1st" level substructure).

The equation of motion of the single assembled substructure (which is given the name $\langle e \rangle$) of the final level that is obtained by repeating the above procedure of synthesizing the levels one by one is the equation of motion of the entire structure. It has the following form:

$$[M_{\langle e \rangle}]\{\ddot{q}_{\langle e \rangle}\} + [K_{\langle e \rangle}]\{q_{\langle e \rangle}\} = \{0\} \quad (17)$$

We should point out that, if in the above "multi-level synthesis" all the "0th" level substructures are assembled into one substructure, then we have the prevalent "single-level synthesis."

As "multi-level synthesis" allows the assembling of only a few substructures (or assembled substructures) at a time, and as the interface coordinates of the substructures of the previous level always have some components that degenerate into interior coordinates in the present level, each synthesis can be kept on a small scale.

III. Improved Assembling Method II - "Successive Synthesis"

The main idea of "successive synthesis" is to synthesize the general equation of motion of a substructure (or assembled substructure) with the direct equation of motion of another substructure (or assembled substructure) and to obtain the equation of motion of the total structure by such successive assembling of each of the direct equations of motion of the (assembled) substructures.

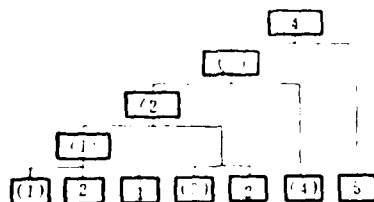


Figure 3. A tree-type substructure system for successive synthesis.

Figure 3 shows a tree-type substructure system for successive synthesis applied to the system shown in Figure 1. In the figure, () denotes the substructure whose general equation of motion is used in the synthesis, and < > denotes assembled substructure.

We obtain from the usual synthesis procedure the general equation of motion of substructure r

$$[\hat{m}_{(r)}]\{\ddot{p}_{(r)}\} + [\hat{k}_{(r)}]\{p_{(r)}\} = \{\hat{R}_{(r)}\} \quad (18)$$

Note that successive synthesis can be regarded as one mode of multi-level synthesis. Hence, its frequency criterion is still taken to be Eq. (4).

Synthesize Eq. (18) and the direct equation of motion of substructures $r+1$ and \hat{r}

$$[m_{r+1}]\{\ddot{u}_{r+1}\} + [k_{r+1}]\{u_{r+1}\} = \{R_{r+1}\} \quad (19)$$

$$[\hat{m}_r^B]\{\ddot{u}_r^B\} = \{R_r^B\} \quad (20)$$

The synthesized coordinates are

$$\{q_{\langle r \rangle}\} = [q_{\langle r \rangle}^{BT} \ q_{\langle r \rangle}^{IT}]^T$$

$\{q_{\langle r \rangle}^B\}$ includes those components of $\{u_{\langle r \rangle}^B\}$ and $\{u_{\langle r+1 \rangle}^B\}$ that constitute the interface coordinates of substructure $\langle r \rangle$ and the $\{u_r^I\}$ of the rigid substructures that are located on the edges. $\{q_{\langle r \rangle}^I\}$ is naturally made up of the independent components of $\{u_{\langle r \rangle}^B\}$, $\{u_{r+1}^B\}$ and $\{u_r^I\}$ ($\hat{r} = \hat{1}, \hat{2}, \dots$) that have degenerated (with respect to $\langle r \rangle$) into interior coordinates as well as $\{u_{r+1}^I\}$ and $\{p_{\langle r \rangle}^N\}$. For example, for the assembled substructure $\langle 1 \rangle$,

$$\{q_{\langle 1 \rangle}^B\} = [u_1^{IT}, u_3^{BT}]^T, \quad \{q_{\langle 1 \rangle}^I\} = [u_2^{IT}, u_1^{BT}, p_{\langle 1 \rangle}^{NT}]^T \quad /32$$

Now we establish the following assembling matrix $[T]$:

$$\{p_r\} = [T_{\langle r \rangle}]\{q_{\langle r \rangle}\}, \quad \{u_{r+1}\} = [T_{r+1}]\{q_{\langle r \rangle}\}, \quad \{u_r^B\} = [T_r^B]\{q_{\langle r \rangle}\} \quad (21)$$

The stiffness matrix and mass matrix associated with $\langle r \rangle$ are obtained in a similar manner as Eqs. (14) and (15):

$$[K_{\langle r \rangle}] = [T_{\langle r \rangle}]^T [\hat{k}_{\langle r \rangle}] [T_{\langle r \rangle}] + [T_{r+1}]^T [k_{r+1}] [T_{r+1}] \quad (22)$$

$$[M_{\langle r \rangle}] = [T_{\langle r \rangle}]^T [\hat{m}_{\langle r \rangle}] [T_{\langle r \rangle}] + [T_{r+1}]^T [m_{r+1}] [T_{r+1}] + \sum_i [T_i]^T [\hat{m}_i^{\text{ext}}] [T_i] \quad (23)$$

Similarly, we can obtain the interface force $\{R_{\langle r \rangle}\}$ of $\langle r \rangle$. Note that Eqs. (22) and (23) are band-shaped matrices whose bandwidths reach a minimum in chain type structures. Therefore, the direct equation of motion for $\langle r \rangle$ is

$$[M_{\langle r \rangle}] \{\ddot{q}_{\langle r \rangle}\} + [K_{\langle r \rangle}] \{q_{\langle r \rangle}\} = \{R_{\langle r \rangle}\} \quad (24)$$

The next step is to synthesize the general equation of motion of Eq. (24) with the direct equation of motion of $r + 2$,

$$[m_{r+2}] \{\ddot{u}_{r+2}\} + [k_{r+2}] \{u_{r+2}\} = \{R_{r+2}\} \quad (25)$$

(If $r + 2$ has connected to it a rigid substructure $\hat{r} + 1$ then set up $[m_{\hat{r}+1}^{\text{II}}]$ and $[\hat{r}+1 D_{r+2}]$ of $\hat{r} + 1$ to be used in the synthesis.) The synthesis procedure is as described above. In this manner, the equation of motion of the single assembled substructure $\langle e \rangle$ obtained by the successive assembling of all the substructures is the equation of motion of the total structure. Its form is necessarily similar to Eq. (17).

IV. Discussion, Example and Conclusion

Compared to the prevalent single-level synthesis, the two improved assembling methods presented in this paper have the advantage of keeping each synthesis on a fairly small scale. Thus, they are very useful for calculation of dynamic problems

of large complex structures on a computer with small interior capacity.

Although the method of successive analysis requires a larger number of syntheses than multi-level synthesis, it requires a small number of eigenvalue problem analyses, and thus has a slightly higher accuracy. Nevertheless, under the condition of the frequency criterion given by Eq. (4), the accuracy of multi-level synthesis is also very satisfactory. (See Table 1, ⑥) We should point out that to relatively increase the accuracy of multi-level synthesis, one should fully utilize its ability to assemble several substructures at once, and reduce the number of eigenvalue problem analyses to a minimum. Furthermore, under most conditions, the method of successive synthesis has a better ability to reduce the bandwidths of the stiffness matrix and the mass matrix. It has, therefore, a higher computation efficiency in general. However, successive synthesis is inferior to multi-level synthesis in that it cannot be applied to the modes of natural parts. When using the method of successive synthesis, one should use the general equation of motion of identical substructures and symmetrical substructures in the synthesis so as to be able to reduce the amount of computation work based on the "identity" and "symmetry" characteristics. In summary, the best effect can be obtained by a tactful combination of multi-level synthesis and successive synthesis. Hence, a combined "multi-level successive synthesis" possesses the effectiveness and flexibility that "single-level synthesis" lacks.

When using the rigid substructure technique, it is not necessary to perform a series of matrix operations following the procedure given in Ref. [11], but just to establish the matrices $[m_r^{II}]$ and $[r_r D_r]$. To save computer time, we suggest that all rigid substructures be directly assembled into the "1st" level substructures.

We calculated the frequency and vibration modes of an aircraft (Figure 4) using the fixed-interface mode of the multi-level

synthesis. Two schemes were used for subdividing the structure, one with 6 substructures and the other with 4 substructures. The method of successive synthesis was applied to the 4-substructures scheme¹ of Figure 4, using the fixed interface mode. The results of these calculations are tabulated in Table 1 along with the results of finite element solution for the entire aircraft and single-level synthesis. The errors of each method are given with reference to the values obtained from the finite element method, taken to be accurate.

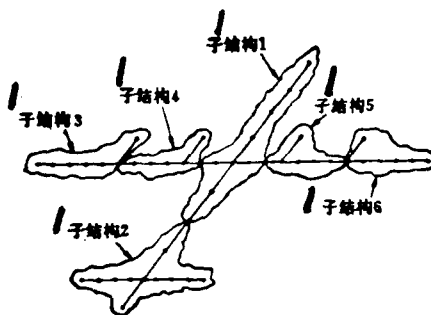


Figure 4. A dynamic substructure model of an aircraft.

Key: 1) Substructure.

From the error analysis for ④ - ⑥ in Table 1, we see that /34 the result of computation not only depends on the order of accuracy imposed on it but also is greatly affected by the selection of the frequency cut-off condition. Obviously, it is not reasonable to use the same cut-off frequency for every level. Comparison of ③ and ⑥ shows that the accuracy obtained by using Eq. (4) as the frequency criterion in the multi-level synthesis is not any lower than that of the single-level synthesis.

1. Combine substructures 3 and 4, and substructures 5 and 6 to form new substructures. This gives a 4-substructures scheme.

Table 1. Comparison of accuracies of two improved substructural assembling methods with those of other synthesis methods.

1 序号	4. 基于子结构固定界面法										逐步法										半自由界面法 (取固定界面法)											
	2. 半自由界面法					5. 子结构法					6. 子结构法 (固定界面法)					7. 逐步法					8. 半自由界面法					9. 半自由界面法						
	①	②	③	④	⑤	①	②	③	④	⑤	①	②	③	④	⑤	①	②	③	④	⑤	①	②	③	④	⑤	①	②	③	④	⑤		
误差	°	°	%	°	%	°	%	°	%	°	%	°	%	°	%	°	%	°	%	°	%	°	%	°	%	°	%	°	%	°	%	
1	15.7898	15.7898	0010	15.7905	0033	15.7905	0030	15.7924	0150	15.7903	0017	15.7905	0030	15.7898	0020	15.7898	15.7898	15.7898	15.7898	0018												
2	20.5348	20.5348	0015	20.5347	0001	20.5348	0005	20.5348	0005	20.5347	00005	20.5348	0005	20.5348	0018	20.5348	20.5348	20.5348	20.5348	0018												
3	25.4181	25.4181	0	25.4177	0080	25.4171	0040	25.4189	0100	25.4187	0022	25.4171	0010	25.4181	0	25.4189	25.4189	25.4189	25.4189	0008												
4	28.8475	28.8475	0	28.8478	0004	28.8481	0020	28.8447	0010	28.8477	0009	28.8471	0020	28.8475	0	28.8474	28.8474	28.8474	28.8474	0003												
5	30.7950	30.7950	0	30.7958	0018	30.7958	0030	30.7971	0020	30.7974	0013	30.7958	0030	30.7950	0	30.7950	30.7950	30.7950	30.7950	0												
6	34.5821	34.5825	0012	34.5840	0064	34.5860	0010	34.5900	0070	34.5847	0073	34.5850	0010	34.5822	0003	34.5814	34.5814	34.5814	34.5814	0020												
7	44.8113	44.8118	0007	44.8143	0087	44.8188	0100	44.8211	0200	44.8138	0078	44.8140	0080	44.8118	0008	44.8118	44.8118	44.8118	44.8118	0												
8	53.2328	53.2343	0018	53.2357	0042	53.2380	0200	53.2421	0300	53.2282	0090	53.2308	0100	53.2240	0009	53.2231	53.2231	53.2231	53.2231	0008												
9	53.5028	53.5030	0013	53.5182	0303	53.5212	0300	53.5553	0100	53.5117	0165	53.5208	0300	53.5032	0008	53.5024	53.5024	53.5024	53.5024	0009												
10	104.8811	104.8120	0090	104.8480	0550	104.8012	0100	105.7804	1.1300	104.8582	0717	104.7708	1000	104.8098	0210	104.5808	104.5808	104.5808	104.5808	0003												
11	128.2660	128.3792	0064	128.5082	1070	128.7816	0100	127.9917	7.5900	128.5117	1997	128.7883	0100	128.3227	0820	128.2556	128.2556	128.2556	128.2556	0												

13. 1. 除①②外, 都是采用“半自由界面法”的误差内值 $\alpha = 0.0001$, $\beta = 1.5$, $\omega_1 = 405$ 弧度 (注意, 第①②的 $\omega_1 = 300$ 弧度), 10^{-6} 控制收敛精度。
 2. 第③④⑤以 10^{-6} 控制收敛, 但采用本文程序内(4)式, $\alpha = 1.5$, $\omega_{max} = 133.33$ 弧度。
 3. 第⑥⑦是 10^{-6} 控制收敛。
 4. “Rubin法”是指对自由子结构的(CG)采用Rubin提出的计算式(4)。
 5. “虚刚度”指“虚刚度分析法”。
 6. 本表所有数据都是4子结构方案下计算的结果。

(See "Key" and "Notes" on next page.)

Key: 1) Non-zero order of frequency; 2) Finite element method; 3) Fixed-interface single-level synthesis; 4) Fixed-interface multi-level synthesis; 5) 6-substructures model; 6) 4-substructures model; 7) Successive synthesis (fixed-interface mode); 8) Single-level free-interface method (pseudo-fixed-interface method); 9) Without residual inertia [7]; 10) With residual inertia [8]; 11) Rubin method; 12) Psuedo-method; 13) Note:

Note:

- 1) Except for (6), the results have been obtained by using the single-level synthesis frequency criterion $\omega_t = \alpha \omega_{\max}$, $\alpha = 1.5$, $\omega_t = 405$ rad (200 rad for (3)), and 10^{-6} as convergence condition.
- 2) The convergence condition for (6) is also 10^{-6} , but Eq. (4) of this paper is used as frequency criterion, and $\alpha = 1.5$, $\omega_{\max} = 133.33$ rad.
- 3) The convergence condition for (4) is 10^{-10} .
- 4) "Rubin method" refers to the computation of [G] of free-interface substructure by means of the relation given by Rubin [4].
- 5) "Pseudo-method" refers to "pseudo-structure analysis."
- 6) All results have been calculated for the 4-substructure model if not otherwise indicated.

The values of μ obtained statistically in this paper are all lower than its conservative value 1.5. Also, (9) - (10) in Table 1 show that taking the residual inertia into consideration does little to improve accuracy of the results.

We want to thank Prof. Chao Ling-ch'en for proof-reading and making corrections on this paper, Prof. Huan Wen-hu and Assist. Prof. Chu Te-mao for their valuable suggestions, and Deputy Chief Engineer Kuan Te for his helpful instructions.

REFERENCES

1. W. C. Hurty, "Dynamic Analysis of Structural Systems for Using Component Modes," AIAA J. V. 3, n. 4, 1965.
2. R. R. Craig and M. C. C. Bampton, "Coupling of Substructures for Dynamic Analysis," AIAA J. V. 6, n. 7, 1968.
3. R. H. MacNeal, "A Hybrid Method of Component Mode Synthesis," Computers & Structures, V. 1, n. 4, 1971.
4. S. Rubin, "Improved Component-Mode Representation for Structural Dynamic Analysis," AIAA J. V. 13, n. 8, 1975.
5. R. R. Craig and C-J. Chang, "Free-Interface Methods of Substructure Coupling for Dynamic Analysis," AIAA J. V. 14, n. 11, 1976.
6. Wang Wen-liang, Tu Ts'uo-jun and Chen K'ang-yuan, "Critique on Modal Synthesis and a New Improvement," Acta Aeronautica Et Astronautica Sinica, No. 3, 1979.
7. Chu Te-mao, "Modal Synthesis in Structural Dynamic Analysis," Naching Institute of Aeronautics and Astronautics, 1979.

8. Chang Te-wen, "Free-Interface Modal Synthesis," Technical Papers on Boats and Blimps, Chinese Research Institute of Aeronautics and Astronautics, No. 1, 1980.
9. R. M. Hintz, "Analysis Methods in Component Mode Synthesis," AIAA J. V. 13, n. 8, 1975.
10. R. R. Craig and C-J. Chang, "On the Use of Attachment Modes in Substructure Coupling for Dynamic Analysis," AIAA/ASME 18th Struct. Struct. Dyn. & Materials Conf., 1977.
11. Chang Te-wen and Liu Kuo-kuang, "Modal Synthesis Including Analysis of Vibration and Response of Rigid Substructures," Research Papers of the 1980 Annual Conference, 1980.9, Chinese Society of Aeronautics and Astronautics, Shanghai, Technical Papers on Boats and Blimps, No. 1, 1980.

9-NODE QUADRILATERAL ISOPARAMETRIC ELEMENT

Wu Yungui

(Institute of Mechanics, Academia Sinica)

Abstract

Several authors [2-4] have presented numerical results which demonstrated the stiffening of 8-node and 12-node quadrilateral isoparametric elements when distorted 8-node or 12-node quadrilateral isoparametric element is significant. The results are not as good as those obtained by using quadrilateral element consisting of two or four linear strain triangles. The results obtained by distorted elements are essentially consistent with those obtained by undistorted elements if 9-node element is used as quadrilateral isoparametric element and Lagrange polynomials as interpolation functions. Numerical results show that 9-node isoparametric element is superior to 8-node isoparametric element, 12-node isoparametric element and quadrilateral element consisting of two or four linear strain triangles.

I. Introduction

Isoparametric elements are a fairly important type of finite elements. The usually adopted shape functions belong to the family of "Serendipity" functions [1]. In recent years, several authors have demonstrated the stiffening of 8-node and 12-node quadrilateral isoparametric elements when the elements are distorted from a rectangular shape, which has an adverse

Received in February 1982.

effect on the computed results. Stricklin, et al. [2] used a cantilever beam as example to compare the effect on computed results produced by five different element configurations. When the shape of the quadrilateral is severely distorted from a rectangular shape, the results obtained by using 8-node elements are not acceptable. The results also show that it is better to use the quadrilateral element formed by two or four linear strain triangles than the 8-node quadrilateral isoparametric element. Bäcklund [3] used 2×2 Gaussian integration points on the 8-node quadrilateral element and recalculated the example given in [2]. The calculations show that the results are slightly better than those obtained by using the 3×3 Gaussian integration points, but no substantial improvements have been achieved. The same problem was taken up by Gifford [4], using 12-node quadrilateral isoparametric elements to give the results for the maximum tip deflection and maximum stress as computed with 3×3 and 4×4 Gaussian integration points. Numerical results show that, even if 12-node elements are used, when the quadrilateral is distorted, the results are still not as good as those obtained by using quadrilateral elements formed by two or four 6-node triangles.

Through numerical examples, we have shown that the 9-node quadrilateral isoparametric elements with Lagrange polynomial as shape function are not only preferable to 8-node isoparametric elements, but also preferable to 12-node isoparametric elements as well as quadrilateral elements formed by 6-node triangles. As the computed results are not very sensitive to changes in the shape of the quadrilateral, the 9-node quadrilateral isoparametric element is a superior isoparametric element.

II. Computed Examples and Results

The shape function and computation procedure for 8-node and 9-node quadrilateral isoparametric elements have been

given in Refs. [1] and [5], and will not be repeated here. We give below the results of the computation carried out on these two examples.

Example 1: Figure 1 shows a cantilever beam [2-4] in /37
five different element configurations, under load P . The computed results given in Refs. [2-4] and the results we obtained using 8-node and 9-node elements in the computation are collected in Tables 1 and 2.

To examine the effect of mesh configuration and the accuracies of the two kinds of isoparametric elements under other load conditions, we list in Table 3 the numerical results of using 8-node and 9-node isoparametric elements in the calculations performed on the same beam under a moment M .

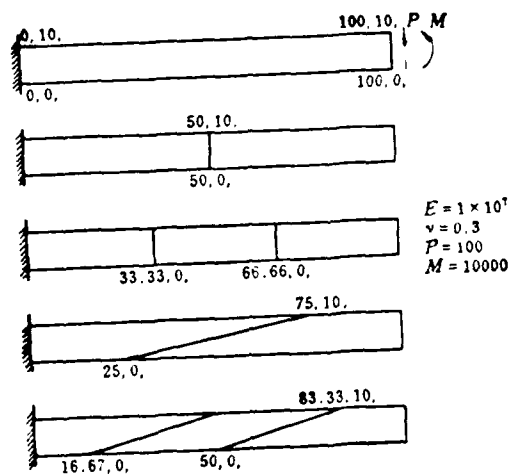


Figure 1. A cantilever beam and element configuration.

Table 1. Tip deflection of a cantilever beam under load P as shown in Figure 1 ($v = 0.04032$ by beam theory including shear strain).

Key: 1) Mesh; 2) Quadrilateral formed by triangles [2]; 3) Two triangles; 4) Four triangles; 5) 12-node quadrilateral [4]; 6) 8-node quadrilateral; 7) 9-node quadrilateral.

网格	2 三角形组成的四边形 (2)		5 12节点四边形 (4)		6 8节点四边形		7 9节点四边形	
	1 一个三角形	4 四个三角形	3 × 3	4 × 4	3 × 3	2 × 2	3 × 3	2 × 2
1	0.03001	0.03087	0.03761	0.03761	0.03054 0.03051 0.03054	0.03758 0.03755 0.03758	0.03101 0.03100 0.03101	0.04023 0.04027 0.04023
2	0.03719	0.03804	0.03875	0.03875	0.03720 0.03721 0.03720	0.03871 0.03872 0.03871	0.03817 0.03816 0.03817	0.04023 0.04027 0.04023
4	0.03871	0.03935	0.03926	0.03926	0.03877 0.03876 0.03877	0.03922 0.03922 0.03922	0.03937 0.03937 0.03937	0.04023 0.04027 0.04027
4	0.03185	0.03202	0.01970	0.01542	0.00644 0.00647 0.00643	0.01448 0.01463 0.01456	0.03165 0.03164 0.03167	0.04434 0.04194 0.04434
5	0.03824	0.03845	0.03165	0.02928	0.01766 0.01773 0.01766	0.03026 0.03112 0.03117	0.03326 0.03326 0.03326	0.04262 0.04131 0.04262

Table 2. Peak stresses at the root of a cantilever beam under load P as shown in Figure 1 (± 600.0 by beam theory). /38

Key: 1) Mesh; 2) 8-node; 3) 9-node; 4) 12-node [4].

1 网格	2 8节点 2 × 2	3 9节点 2 × 2	4 12节点 [4] 3 × 3	4 12节点 [4] 4 × 4
1	±600.0	±600.0	±600.0	±600.0
2	±600.0	±600.0	±600.0	±600.0
3	±600.0	±600.0	±600.0	±600.0
4	+262.9 -142.2	+605.6 -614.8	+668.2 -394.5	+480.2 -305.2
5	+440.3 -385.6	+603.8 -609.9	+859.2 -602.0	+782.7 -565.1

Table 3. Tip deflection and peak stresses of a cantilever beam under a moment M as shown in Figure 1 (2 x 2).

Key: 1) Mesh; 2) Tip deflection; 3) Maximum stress; 4) 8-node; 5) 9-node; 6) Beam theory.

1 网格	2 端部各点的位移			3 最大应力		
	4 8节点	5 9节点	6 梁理论	4 8节点	5 9节点	6 梁理论
1	0.05735 0.05728 0.05735	0.05000 0.05000 0.05000		±600.0	±600.0	
2	0.05848 0.05844 0.05848	0.05000 0.05000 0.05000		±600.0	±600.0	
3	0.05899 0.05895 0.05899	0.05000 0.05000 0.05000	0.05000	±600.0	±600.0	±600.0
4	0.02138 0.02297 0.02572	0.05000 0.05000 0.05000		+245.0 -89.3	±600.0	
5	0.04723 0.04713 0.04595	0.05000 0.05000 0.05000		+458.0 -404.5	±600.0	

Example 2: Figure 2 shows a cantilever beam in two element configurations, under load P or under a moment M. The results of computation using 8-node and 9-node elements are given in Table 4. The peak stresses in the table have been obtained by calculations using the method given in Ref. [6].

Figure 2. A cantilever beam and element configuration.

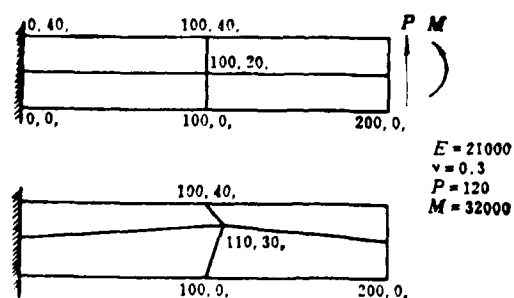


Table 4. Tip deflection and peak stresses of a cantilever beam /39
under load P or moment M as shown in Figure 2 (2 x 2).

Key: 1) Load; 2) Mesh; 3) Tip deflection; 4) Peak stress at the root; 5) 8-node; 6) 9-node; 7) Beam theory; 8) Concentrated force P; 9) Moment M.

1	2	3 端部各点的位移			4 根部最大应力		
		5 8节点	6 9节点	7 梁理论	5 8节点	6 9节点	7 梁理论
8	1	2.8983	2.9320	2.9486	± 92.01	± 90.64	± 90.00
		2.9030	2.9405				
		2.9069	2.9405				
		2.9030	2.9405				
		2.8983	2.9320				
	2	2.8575	2.9315	2.9486	+ 82.26 - 84.83	+ 87.91 - 90.92	± 90.00
		2.8469	2.9231				
		2.8265	2.9399				
		2.8449	2.9228				
		2.8547	2.9301				
9	1	5.6696	5.7114	5.7143	± 122.6	± 120.3	± 120.0
		5.6640	5.7109				
		5.6656	5.7094				
		5.6640	5.7109				
		5.6656	5.7114				
	2	5.6916	5.7176	5.7143	+ 116.9 - 105.5	+ 120.0 - 120.4	± 120.0
		5.6953	5.7098				
		5.6768	5.7111				
		5.6857	5.7087				
		5.6917	5.7176				

III. Discussion and Conclusion

The results of our computation show that it is preferable to use 2 x 2 Gaussian integration points for 9-node isoparametric elements. This is in agreement with the results of computation given in Refs. [3-5] for 8-node and 12-node isoparametric elements.

Although isoparametric elements may have any shape at all, rectangular shapes are preferable. The greater the deviation from the rectangular shape, the larger the error in the computed results. This phenomenon is especially apparent in the 8-node and 12-node isoparametric elements of the Serendipity family, while it is not noticeable in the 9-node isoparametric elements. For example, for the meshes 4 and 5 given in Table 1, the results obtained by using the isoparametric elements of the Serendipity

family have up to 60% error, which is totally unacceptable. The corresponding error in the stresses is also very large. On the other hand, when 9-node isoparametric elements are used, the errors are small, only a few percent. This is a major advantage of the 9-node element over the 8-node or 12-node element.

It is an important subject to mathematically analyze the effect of the shape of the elements on the results of computation. However, not much progress has been made in this direction. In Refs. [8] and [9], the method of Taylor's series expansion has been applied to the study of the effect of the shape of the element boundary on the accuracy of high-order elements, with the conclusion that when the elements have curved boundaries, the convergence of the high-order elements will be on the same order as that of the linear element. However, Ref. [10] gives an explanation of this phenomenon from a different angle of view, and disagrees with the above approach. The elements used in our calculations are quadrilaterals with the points on the straight sides located at the positions of the mid-points. The results of our calculations can not be explained from either of the above viewpoints.

The use of Lagrange polynomial as interpolation function for regular elements (rectangles and parallelepipeds) was first proposed by Argyris et al. [7]. Ref. [5] regards this kind of element as being inferior to the isoparametric elements belonging to the Serendipity family, which are currently very popular. However, the results of our calculation clearly show that the 9-node isoparametric elements are superior.

We point out in passing that the degree of freedom of the inner nodes of the 9-node elements can be eliminated via the method of matrix reduction after the stiffness matrix of the elements are formed. Thus, the interior capacity of computer required by the total stiffness matrix is the same for 8-node /40

and 9-node elements. Therefore, the interior capacity of computer demanded by these two kinds of elements is basically the same.

REFERENCES

1. Zienkiewicz, O. C., Irons, B. M., Ergatoudis, J., Ahmad, S., and Scott, F. C., Isoparametric and associated element families for two and three dimensional analysis in Finite element method in stress analysis, Holland, I and Bell, K eds. Chapter 13 Tapir Trondheim 1969.
2. Stricklin, J. A., Ho, W. S., Richardson, E. Q. and Haisler, W. E., On isoparametric vs. linear strain triangular elements. Int. Jour. Num. Methods in Eng. Vol. 11 1041-1043 1977.
3. Backlund, J., On isoparametric elements. Int. Jour. Num. Methods in Eng. Vol. 12 731 1978.
4. Gifford, L. M., More on distorted isoparametric elements. Int. Jour. Num. Methods in Eng. Vol. 14 290-191 1979.
5. Zienkiewicz, O. C., The finite element method, third edition. McGraw-Hill Book Company (UK) Limited 1977.
6. Hinton, E., Scott, F. C. and Ricketts, R. E., Local test squares stress smoothing for parabolic isoparametric elements. Int. Jour. Num. Methods in Eng. Vol. 9 235-238 1975.
7. Argyris, J. H., Buck, K. E., Fried, I., Gareczek, G., and Sharpf, D. W., Some new elements for matrix displacement methods. 2nd Conf. on Matrix Methods in struct. mech., Air Force Ints. of Techn., Wright Patterson Base, Ohio, Oct. 1968.

8. Fried, I., Accuracy of complex finite elements. AIAA Journal Vol. 10 347-349 1972.
9. Fried, I., Possible loss of accuracy in curved (isoparametric) finite elements - comment on a paper by Henshell, Walters and Warburton. Jour. Sound and Vibration. Vol. 23 507-510 1972.
10. Henshell, R. D., Walters, D. and Warburton, G. B., On possible loss of accuracy in curved finite elements. Jour. Sound and Vibration. Vol 23 510-513 1972.

APPLICATION OF LASER HOLOGRAPHIC INTERFEROMETRY
TO VIBRATION ANALYSIS OF
AEROCRAFT BEAM STRUCTURE MODEL

/41

Chin Juan-ch'an
(Ch'inhua University)

Wang Shen-hsiao, Ch'en Kuo-ping, Shen P'ei-ch'ing
(Hongan Corporation)

Abstract

This paper describes how to make use of laser holographic interferometry in vibration analysis of aircraft beam structure models. Various vibration modes for two kinds of simplified models (three-beam and five-beam) of the same wing have been photographed by means of laser holography. Meanwhile, their natural frequencies and node distributions have been obtained from theoretical calculations. The good agreement between the results demonstrates that both the experimental and the theoretical results are reliable.

The vibration analysis of three-beam and five-beam models for an aircraft wing beam construction shows that some difference exists between their five-order vibration modes. This indicates the existence of some difference in rigidity between the simplified models. The simplification of the simple three-beam models leads to some errors, and the five-beam model proves to be more trustworthy.

Received in June 1981.

I. Introduction

The beam structure is very commonly seen in aircraft structures, especially in the wings of the aircraft. The actual structure is usually a fairly complicated multi-beam structure that needs to be simplified for the purpose of computation or experimental studies. Suppose a reasonable model has been obtained. It is required that this model be simple and yet possess the mechanical properties (especially such dynamic properties as dynamic stiffness) of the original structure. In the process of simplification, however, it is inevitable that there will be some difference in stiffness distribution between the model and the original structure because of the assumptions, simplifications and combinations made. Hence, to test the validity of the model, it is necessary to perform theoretical and experimental vibration analysis on the model.

The objects of our study are the three-beam and five-beam models of the wing. (See Figure 1.) These simplified models have been obtained by idealizing the actual wing structure. This structure is one of a beam with variable cross-section. Obviously, the three-beam model promises simplicity in calculations and construction. Yet, how well does it represent the original structure? This question can only be answered by a vibration analysis. Thanks to the development in the techniques and methods of calculation, it is now possible to apply finite element analysis to the problem and obtain the natural frequencies and mode distributions of the structure via accurate theoretical calculations. As early as in the 60's, laser holographic interferometry was shown to be an effective tool in experimental vibration analysis. However, at present, it has not yet been very widely applied. We carried out experimental and theoretical vibration analysis on the above two models with the purpose of finding a simplified model that is reasonable as well as simple.

II. Vibration Analysis by Laser Holographic Interferometry

Vibration analysis by laser holographic interferometry is an optical method that possesses many merits:

1. The distribution of vibration modes of the entire wing model can be obtained in the same holographic picture. /42
2. The method has very high sensitivity, with the spacing between the fringes as small as 0.16 μm .
3. The measurement does not require contact with the wing model, thus eliminating the effect of the additional mass of the transducer when one is used.
4. The frequencies and vibration modes of various orders can be accurately determined, and the measurement is not affected by the frequency range.

Two commonly used methods of vibration analysis are the time-averaged method and the method of double-exposure of frequency glittering and pulses. As we are interested in obtaining the node distribution, we used the time-averaged method. In the reconstructed holographic image, the following relationship exists between the fringes and the amplitude of vibration:

$$I = K J_0^2 \left[\frac{2\pi}{\lambda} A(x, y) (\cos\theta_1 + \cos\theta_2) \right] \quad (1)$$

In the above equation, J_0 is the first-order Bessel function, λ is the wavelength of the laser used, $A(x, y)$ is the amplitude of vibration at various points on the object, θ_1 is the illumination angle, i.e., the angle between the beam illuminating the object and the direction of vibration, and θ_2 is the observation angle, i.e., the angle between the line joining the object and the photographic film and the direction of vibration.

The model (the bright frame) and the lines of equal amplitude can be observed on the time-averaged film. The data were used to analyze the behavior and structure of the wake.

The experimental models are four airframe models of the wing root of an aluminum alloy. The external dimensions of the two models are the same. The dimensions of the cross-section gradually decrease toward the tip. Its height is 410 mm (not including the root) and the width of the root is 270 mm. The two wing models were clamped onto a grooved platform at angles of 75°, respectively. The vibrations were produced with an electro-magnetic vibrator and were picked up with a P.W.T. piezoelectric crystal chip. The waveforms were observed on an oscilloscope, and the frequency was measured with a frequency meter. The experimental set-up is shown in Figure 1.

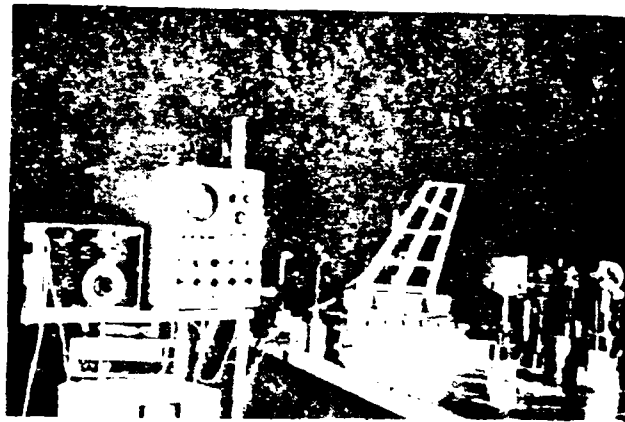


Figure 1. Experimental apparatus.

The experimental study was carried out on a shock-proof platform with the use of a 20 mW He-Ne laser. It was complicated by the large size of the model, the ladder-like surface, the large space occupied by the frame and the fact that the light reflected off the object was very weak. At first, we tried to increase the area from which light was reflected by covering the model with tissue paper soaked with tung-oil. This resulted in poor fringe quality and loss of fidelity. Later, we improved

our method of steadying the specimen and other elements in the optical path, precisely adjusted and stabilized the natural frequencies and monitored them with a piezoelectric crystal chip on the oscilloscope, and carefully adjusted the optical path to ensure an appropriate ratio of reference and object light intensities (approximately 4:1). We were thus able to obtain better quality holograms.

III. Experimental Results and Comparison with Calculated Results /43

The experimentally and theoretically obtained values of the natural frequencies of the two models and their errors are tabulated separately in Tables 1 and 2.

Table 1. Natural frequencies of three-beam model (Hz)

Key: 1) First-order frequency; 2) Second-order frequency; 3) Third-order frequency; 4) Fourth-order frequency; 5) Fifth-order frequency; 6) Measured value; 7) Calculated value; 8) Error.

	1 一阶频率	2 二阶频率	3 三阶频率	4 四阶频率	5 五阶频率
6 测量值	150	410	540	820	1155
7 计算值	144.4	384.6	519.8	735.7	979.6
8 误差	3.7%	6.2%	3.7%	10.2%	15.2%

Table 2. Natural frequencies of five-beam model (Hz)

Key: 1) First-order frequency; 2) Second-order frequency; 3) Third-order frequency; 4) Fourth-order frequency; 5) Fifth-order frequency; 6) Measured value; 7) Calculated value; 8) Error.

	1 一阶频率	2 二阶频率	3 三阶频率	4 四阶频率	5 五阶频率
6 测量值	136	420	510	810	1150
7 计算值	128.9	403.3	479.8	719.7	1129.9
8 误差	5.2%	4.0%	5.9%	9.3%	1.7%

our method of steadying the specimen and other elements in the optical path, precisely adjusted and stabilized the natural frequencies and monitored them with a piezoelectric crystal chip on the oscilloscope, and carefully adjusted the optical path to ensure an appropriate ratio of reference and object light intensities (approximately 4:1). We were thus able to obtain better quality holograms.

III. Experimental Results and Comparison with Calculated Results /43

The experimentally and theoretically obtained values of the natural frequencies of the two models and their errors are tabulated separately in Tables 1 and 2.

Table 1. Natural frequencies of three-beam model (Hz)

Key: 1) First-order frequency; 2) Second-order frequency; 3) Third-order frequency; 4) Fourth-order frequency; 5) Fifth-order frequency; 6) Measured value; 7) Calculated value; 8) Error.

	1 一阶频率	2 二阶频率	3 三阶频率	4 四阶频率	5 五阶频率
6 测量值	150	410	540	820	1155
7 计算值	144.4	384.6	519.8	735.7	979.6
8 误差	3.7%	6.2%	3.7%	10.2%	15.2%

Table 2. Natural frequencies of five-beam model (Hz)

Key: 1) First-order frequency; 2) Second-order frequency; 3) Third-order frequency; 4) Fourth-order frequency; 5) Fifth-order frequency; 6) Measured value; 7) Calculated value; 8) Error.

	1 一阶频率	2 二阶频率	3 三阶频率	4 四阶频率	5 五阶频率
6 测量值	136	420	510	800	1150
7 计算值	128.9	403.3	479.8	719.7	1129.9
8 误差	5.2%	4.0%	5.9%	9.3%	1.7%

The above data show that the measured values are very close to the calculated values. In particular, the errors for the first three orders are all within 6%. The calculated values are generally lower than the measured values. This is attributable to the fact that it is difficult to ensure complete steadiness of the root during the course of the experiment.

Figures 2 and 3 show the vibration modes of the two simplified models obtained by holographic reconstruction and the corresponding node distributions obtained by calculation with the help of a computer. Comparison of these results shows that the tendencies of the location and shape of the nodal lines are the same for the two methods, except for the fifth-order vibration of the three-beam model, whose reconstructed nodal lines lie on the side beams while the calculated nodal lines extend to the root region. There is also an appreciable difference in the measured and calculated frequency values for this mode of vibration.

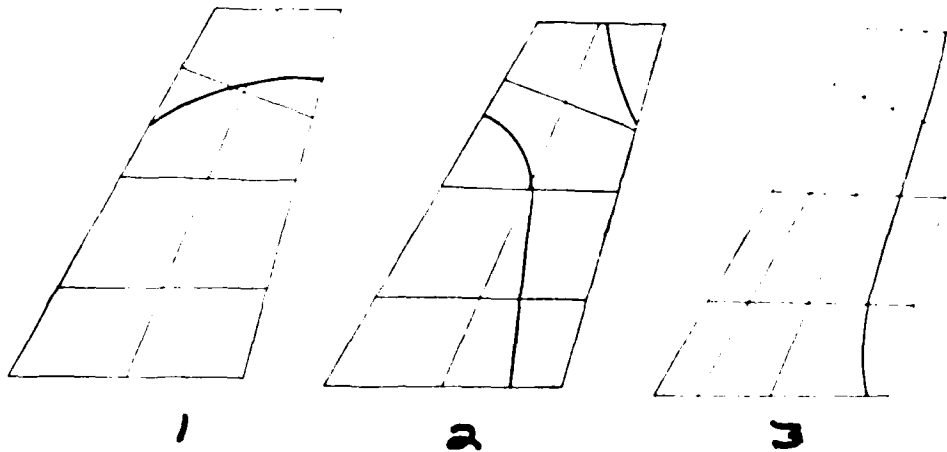
It is worth noting that the fifth-order vibration mode is different in form for the two models. That of the three-beam model is of the torsion form, while that of the five-beam model is of the bending form. This difference is borne out by both the measurement and the calculation. Analysis indicates that there is a reduction in torsional stiffness associated with the three-beam model. Hence, even though this simple model has the merits of ease of construction and simplicity of calculation, it suffers from loss of fidelity in simulation and dynamic stiffness, and therefore should not be used. Analysis of the experiment shows that laser holographic interferometry is an effective and direct method of vibration analysis.

Figure 2. Three-beam wing model

/44



(a) Vibration modes by holographic reconstruction.
Key: 1) Third-order; 2) Fourth-order; 3) Fifth order.



(b) Node distribution by calculation
Key: 1) Third-order; 2) Fourth-order; 3) Fifth order.

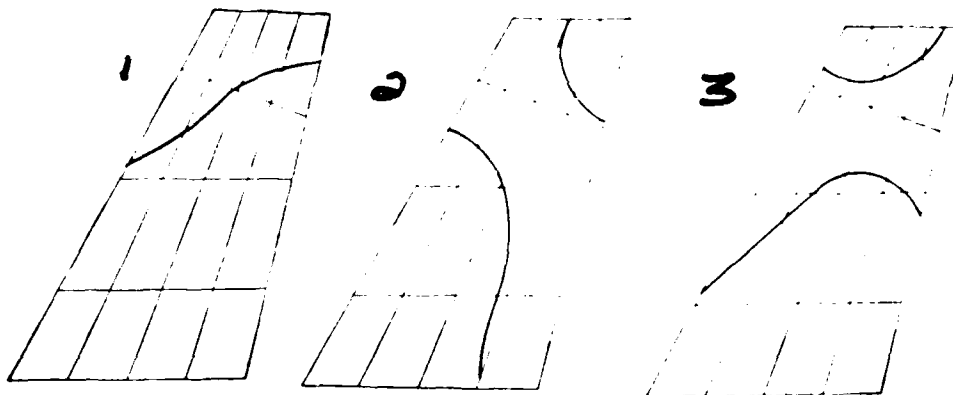
Figure 3. Five-beam model

/45



(a) Vibration modes by holographic reconstruction.

Key: 1) Third-order; 2) Fourth-order; 3) Fifth order.



(b) Node distribution by calculation.

Key: 1) Third-order; 2) Fourth-order; 3) Fifth order.

Other comrades who also participated in this work include Liu Ming-kuan, Chang Hua-shan, Chang Wei-pao and Liu Ch'un-yang.

REFERENCES

1. Application of Holographic Interferometry and Scattered-Fringe Interferometry in Experimental Mechanics, Department of Mechanical Engineering, Ch'inghua University, 1979.
2. Application of Laser Holography in Dynamic Stiffness Model Tests, "Chi Ch'uang," No. 2., 1978.

ON EXPERIMENTAL METHODS FOR DETERMINING
CRITICAL SPEEDS

/47

Yan Litang and Li Qihan
(Beijing Institute of Aeronautics and Astronautics)

Abstract

In this paper the experimental methods for determining the critical speeds of rotor systems are investigated. The methods reviewed here are the peak amplitude method and those based on the characteristics of critical speeds, such as the 90 degree phase lagging, and the rapid change of phase angle.

The peak amplitude method commonly used will introduce significant error in practice if the shaft is out of round or initially bent, or it is observed under the condition of acceleration. Even if the tests are performed at constant speeds the undamped critical speed will still be much higher in case of heavily damped rotors, while the method based on the 90 degree phase shift is more suitable for these cases.

For the lightly damped rotors, which are just the cases for many practical rotors, the method based on the rapid change of phase angle when passing through critical speed is more applicable, since the rotors may be more safely tested with acceleration which does not affect the measured results of critical speeds by using this method.

A modified Nyquist plotting procedure is presented, in which a trial weight is put on the node section of the higher order mode shape, and necessary tests are made only at some speeds near the critical. The vibration vectors without error are then obtained and a circular polar plot can be made. With the aid of the plot the critical speed can be calculated in accordance with the fact that the increment of speed is nearly proportional to the increment of phase

lagging angle in the vicinity of a critical speed.

It is suggested that the first critical may be experimentally determined at lower speeds for the rotors with asymmetric stiffness; these are the cases for many real rotors. The sub-critical is measured in this method and its double is then the first order critical speed. It is known that at sub-critical the vibration frequency is twice the speed, while at critical the vibration frequency is equal to the speed. Therefore, it is possible to distinguish the sub-critical from the first critical by comparing the measured frequency with speed. This method is considered as a safer and simpler method.

Finally the feasibility of the method to determine the critical speeds in the static states of the rotors is described.

ABSTRACT

In this paper the experimental methods for determining the critical speeds of rotor systems are investigated. We have reviewed the peak amplitude method and the method based on the 90° phase lag and the abrupt change of phase in the vicinity of the critical speed. We have included a method for determining critical speed that is a modification of the vibration mode circle method that is usually applied to the problem of flexible shaft balancing. A convenient and safe method for determining the critical speed using low speeds is proposed. Finally, the method for determining the critical speed with the rotor not rotating is discussed. The principles on which the various methods are based are elucidated with physical concepts and simple mathematical expressions. The merits, demerits and range of application of each method are examined.

I. Introduction

The problem of the critical speed has long been recognized, and has been extensively studied. Research on critical speeds is usually centered on the method of computation and on ways to eliminate damages associated with them. Not many studies were made on experimental methods for determining critical speeds. In fact, there are many situations where it is not possible to take into consideration all the important factors when calculating for the critical speeds of rotors with sophisticated structures. In these cases, the accuracy of computed results is low. Hence, experimental methods for determining critical speeds are of great significance.

The critical speed of the rotor bearing system refers to the rotational speed of the rotor at which resonance in the transverse direction is caused by an imbalance in the rotor that is undergoing steady rotation. Unless otherwise stated, this is taken to be the critical speed in the absence of damping. Rotating bearings are widely used in modern aircraft engines and commonly used experimental equipment. Therefore, the rotors are usually lightly damped, and not much difference exists between the critical speed in the presence of damping and that in the absence of damping.

Some aircraft engines use low-stiffness elastic bearings, or have low-stiffness bearing structures. At the first- and second-order critical speeds of such a rotor system, the bending of the shaft is small. The distortion occurs mainly at the bearings. Some papers refer to these two critical speeds as rigid-body (modal) critical speeds. At the third- and higher-order critical speeds, there are more pronounced bending distortions of the shaft. These critical speeds are referred to as bending critical speeds. Thus the vibration modes at the critical speeds are differentiated. Others refer to rigid-body critical speed as bearing resonance, and regard the bending critical speed

as the true critical speed of the rotor. In these papers, the bending critical speeds are differentiated by the ratio of the amount of shaft bending to the total distortion, while several values of the stiffness ratio ($2KL^3/EJ$) are used to differentiate among the rigid-body critical speeds of shafts of uniform cross-section on elastic bearings. In our opinion, it is more appropriate to refer to the first- and second-order critical speeds as rigid-body critical speeds than as bearing resonances, the latter implying that only the bearings resonate while the rotor does not. In fact, the rotor-bearing system is one whole system in which it is not possible to have local resonance of the bearings only. Even if the amplitude of vibration of the rotor is very small or zero, this should be regarded as a particular mode of resonance rather than simply a bearing resonance, not to mention the fact that at the so-called bearing resonance, even though the rotor is hardly bent, its vibrational displacement or rotational angle is nevertheless appreciable.

We can go one step further in the generalization, and regard the rotor, the bearings and the casing as forming one whole unit--the engine. The critical speed is thus the rotational speed of the rotor at which imbalance in the rotor causes a transverse resonance of the engine. The vibrational modes are specified by the amplitudes of vibration of the rotor, bearing, and casing. One should not call those modes with large casing vibrational amplitude casing resonance, and those with large rotor vibrational amplitude, critical speed. /48

Resonances attributable to aerodynamic or other sources of oscillation in the engine may not be referred to as critical speeds. It is not difficult to distinguish these from the resonances arising from rotor imbalance. One only needs to see if the resonance frequency is equal to the rotational speed. Of course, occasionally, the frequency of resonance due to some other source of oscillation may equal rotor speed, but such coincidences are rare.

II. A Commonly Used Method for Determining Critical Speeds-- the Peak Amplitude Method

In this method, the rotational speed corresponding to the peak amplitude of a rotor undergoing steady-state motion is taken to be its critical speed. The amplitude at the critical speed is usually very large, and it is not possible to maintain the critical speed. Therefore, it is common practice to take measurements during acceleration or deceleration past the critical speed, which inevitably affects the results. The critical speed measured during acceleration tends to be on the high side, while that measured during deceleration tends to be on the low side. Hence, better results are obtained by taking the average of these values. As acceleration and deceleration have their associated difficulty in control and measurement, and do not have the same magnitude of effect on the rotational speed, taking the average of their effects does not necessarily produce accurate results.

This method of measuring the critical speed of a rotor undergoing steady-state motion is applicable to rotors with small imbalance or high damping only. At high damping, however, the results obtained with this method tend to be on the high side even though the measurements are made under steady-state conditions. Moreover, deviation from the cylindrical shape or initial bending of the shaft will also result in measurement errors.

III. Determination of Critical Speed from the Phase of Vibration

Many rotors have a phase lag of 90° at critical speed, irrespective of the amount of damping. At low damping, the phase lag undergoes an abrupt change in the vicinity of the critical speed. This is the so-called "inflection" phenomenon.

The critical speed can be determined from these two characteristics.

1. Determination of critical speed from rotor "inflection"

Because the phenomenon of "inflection" is equally pronounced whether the rotor is accelerated past the critical speed at low acceleration or steady-state measurements are made in the vicinity of the critical speed, the measurements are made with the rotor being accelerated past the critical speed for the sake of convenience and simplicity. The source of the reference signal is marked on the shaft. The phase difference between the peak value of shaft vibration and the reference signal is measured with a phase-gain meter, and the region of rotational speeds in which the phase lag undergoes an abrupt change is located, and the critical speed is thus determined. If a phase-gain meter is not available, one can record the vibration waveform on an oscillogram and study its characteristics (Figure 1). The location of the critical speed is determined by finding the speed for which the ratio of the distance between the vibration peak and the reference signal to the wavelength has the largest variation. In Figure 1 $(a/b)_3 - (a/b)_2$ is the largest; therefore, the critical speed lies somewhere between n_2 and n_3 . If, while passing through the critical speed, the shaft undergoes an appreciable bending distortion, then one can attach a sensitive strain gauge to the surface of the shaft along the direction of the length of the shaft and record the strain signal ϵ (Figure 2) on an oscillogram. The rotational speed at which the average strain on the shaft incurs a change in sign for the first time is the desired critical speed. As the rotor can be accelerated past the critical speed, the problem of maintaining the critical speed is avoided. The method of measuring shaft strain has the added advantage of eliminating error due to deviation of the shaft from a cylindrical shape or that due to initial bending.

/49

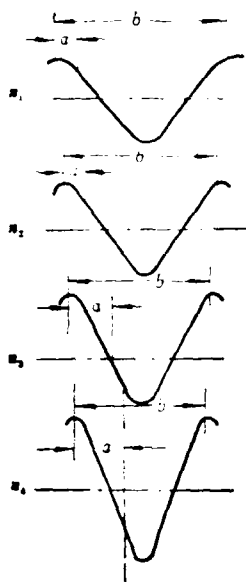


Figure 1. Oscillogram of different speeds in the vicinity of n_{cr} for determining n_{cr} .

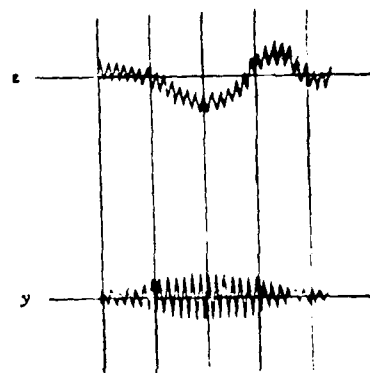


Figure 2. Variation of strain on the shaft passing through n_{cr} , showing the phase change.

2. Determination of critical speed from the 90° phase lag

The phase lag is determined by measuring the angle between the direction of the force causing imbalance and that of the steady-state vibration. The rotational speed at which this angle equals 90° is the critical speed. There are many ways of measuring the direction of the imbalance vector, as discussed in detail in studies related to rotor balancing [1]. The direction of vibration can be determined by making a reference mark on the shaft and using a phase-gain meter for the measurement, or by recording and studying the oscillogram. Because acceleration and deceleration past the critical speed will cause a corresponding increase or decrease in the phase lag [2], this method should be used only for steady-state measurements, and is applicable to relatively heavily damped rotors. As the phase lag is determined from measurement of the direction of the vibration vector, the

accuracy of the result will be affected by deviation of the shaft from the cylindrical shape.

3. Determination of critical speed using the vibration mode circle

We illustrate below the principle of the method of vibration mode circle using as example a rotor of single concentrated mass. The equation of motion of this rotor is

$$m\ddot{Z} + b\dot{Z} + kZ = Fe^{i\omega t} \quad (1)$$

where m is the concentrated mass of the rotor, Z is the radius of motion of the rotor, b is coefficient of viscous damping, F is the imbalance force $m\omega^2 \epsilon$, ϵ is eccentricity of mass, and k is the transverse stiffness coefficient at the location of the concentrated mass. The steady-state solution of the above equation is given by

$$Z = \{(\omega^2 \epsilon) / (\omega_c^2 - \omega^2 - 2i\mu\omega\omega_c)\} e^{i\omega t} \quad (2)$$

where $\mu = b/2m\omega_c$, and $\omega_c^2 = k/m$ is the critical speed. Writing Z as

$$Z = (x + iy)e^{i\omega t}$$

one obtains

$$x^2 + \left[y + \frac{\omega_c^2}{4\mu\omega_c} \right]^2 = \left[\frac{\omega_c^2}{4\mu\omega_c} \right]^2 \quad (3)$$

For a given rotor, $\mu\omega_c$ and ϵ have given values, and at a fixed rotational speed, the above equation describes a circle. When ω is varied, the figure is no longer a circle, but closely approximates a circle. If we take a few points $\omega \approx \omega_c$, the curve obtained should be close to a circular arc. Using this arc to complete the circle will enable us to obtain a circle closely approximating the vibration mode circle for $\omega = \omega_c$.

As there are other factors that need to be taken into consideration in practice, the plot of the measured vector Z does not yield accurate results. Instead, we make use of three vectors in the measurement. First, the vibration vector \bar{A}_x is measured for a given rotational speed n_1 . Then a trial weight is added at a chosen cross-section, and the vibration vector \bar{A}_2 is determined for the same rotational speed. Therefore, the vibration vector due to the imbalance caused by the trial weight is given by

$$\bar{A}_m = \bar{A}_2 - \bar{A}_1 \quad (4)$$

If the error vector is the same in both measurements, then it is eliminated in the process of subtraction, and the \bar{A}_m obtained is a very accurate quantity. The error vectors of deviation of shaft from the cylindrical shape and of initial bending are constant quantities. If the trial weight is placed at the node of a higher-order mode of vibration then the error caused by the higher-order vector is also constant. We illustrate this method with the following example.

Take an angular position in a plane perpendicular to the shaft as the reference direction specified by 0° . This is the direction in which the trial weight is applied. Obtain the \bar{A}_m vectors On_1 , On_2 , On_3 and On_4 for the four rotational speeds n_1 , n_2 , n_3 , and n_4 in the vicinity of the critical speed n_c . Plot these vectors, and make a circle passing through n_1 , n_2 , n_3 and n_4 (Figure 3). The rotational speed corresponding to point C is the desired critical speed. α_1 is the phase lag at n_1 . As the phase lag can be regarded as having a linear relationship with rotational speed in the narrow region in the vicinity of the critical speed, especially for lightly damped rotors, we have

$$\frac{n_s - n_1}{n_3 - n_1} = \frac{90 - \alpha_1}{\alpha_3 - 90} = \frac{\gamma_1}{\gamma_3} \quad (5)$$

AD-A131 828

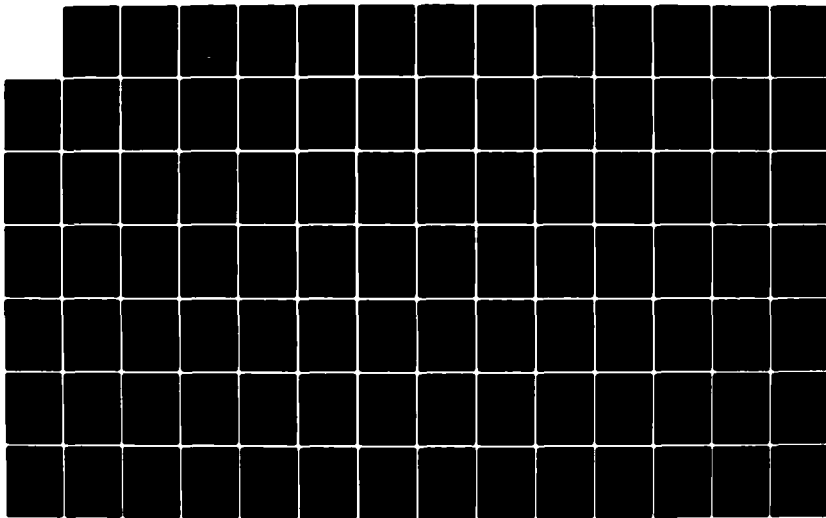
ACTA AERONAUTICA ET ASTRONAUTICA SINICA(U) FOREIGN
TECHNOLOGY DIV WRIGHT-PATTERSON AFB OH S LU ET AL.
28 JUL 83 FTD-ID(RS)T-0266-83

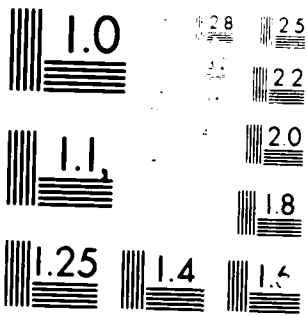
2/3

UNCLASSIFIED

F/G 20/4

NL





NATIONAL BUREAU OF STANDARDS
 NATIONAL BUREAU OF STANDARDS

From this, the critical speed is calculated to be

/50

$$\omega_c = (\pi_1 \gamma_1 + \pi_2 \gamma_2) / (\gamma_1 + \gamma_2) \quad (6)$$

Here the speeds at which the measurements are made need not be equally spaced, so as to avoid the critical speed. If \bar{A}_m contains error vectors of constant magnitude, then the circle maintains its shape while it is shifted in position. If \bar{A}_m contains other errors, then the figure will deviate slightly from the circular shape, and the critical speed obtained contains a slightly larger error.

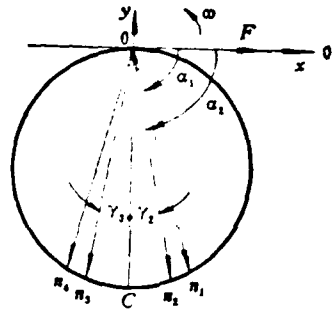


Figure 3. Illustration of plotting \bar{A}_m circle to determine n_{cr} .

IV. Method for Determining Critical Speed at Low Rotational Speed

For a rotor with asymmetrical stiffness under the action of the gravitational force, there exists a sub-critical speed, i.e., the amplitude becomes very large at a rotational speed equal to half the first-order critical speed. Hence, it is possible to obtain the critical speed by measuring the sub-critical speed and multiplying the result by 2. Unevenness in the wall thickness of the shaft and asymmetry in the tightness at the connections are some of the factors giving rise to asymmetry in stiffness. In practice, these factors are inevitable, and such rotors will incur displacements at the frequency of 2ω under the action of

the gravitational force. This is equivalent to a rotor with uniform stiffness under the action of an oscillating force of frequency 2ω . The frequency of the resonance caused by this force is equal to ω_{c1} . The resonance occurs at a rotational speed of $\frac{1}{2}\omega_{c1}$, and is not accompanied by the phenomenon of "inflection." These facts can be used to distinguish the sub-critical from the critical speed (Figure 4). Does there exist a sub-critical speed for the second-order critical speed? The second-order speed arises from the dipole moment. Only when the relation $k_{x1} \approx k_{y2} \neq k_{y1} \approx k_{x2}$ holds for two locations on the shaft separated by a relatively large distance, which is equivalent to the action of a dipole moment varying at the frequency of 2ω , can there be a second-order critical speed. Such situations are rarely encountered, but are not absolutely impossible. First- and second-order sub-critical speeds can also arise from static or dynamic imbalance. However, because of the small amplitudes, these are difficult to measure. The sub-critical speed occurs at a low speed, and the vibrations associated with it are small. Therefore, this method can be applied in steady-state measurements to find the critical speed that is higher than the operating speed, and hence has a definite superiority over other methods.

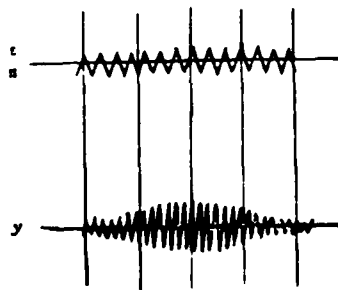


Figure 4. Schematic oscillogram at sub-critical speed, showing the vibration frequency is double the rotational speed.

V. Feasibility of Determining Critical Speed with the Rotor not Rotating

The effect on the natural frequencies of the moment of inertia of a rotor that is not rotating but undergoing bending vibration in a plane is different from that of the mass spin moment of a rotor undergoing synchronized rotation. The stiffness of the connections of a rotor made up of many parts that operate under the conditions of high speed and high temperature is different from that of a rotor that is not rotating and is at normal temperatures. Hence, the transverse resonance frequency of a rotor vibrating in a plane at normal temperatures is in general not equal to its critical speed. However, in cases where the moment of inertia is very small, and where the stiffness of /51 the connections of the rotor does not vary very much with speed and temperature, the transverse resonance frequency can be a good approximation to the critical speed. Although fairly large errors sometimes result from determining the critical speed by measuring the transverse resonance frequency of a rotor vibrating in a plane, this method is nevertheless valuable as a means to obtain a rough estimate of the critical rotational speed because of its simplicity.

Conclusion

In this paper we have discussed the merits, demerits and range of applicability of various methods of experimentally determining the critical speeds of a rotor.

In cases where neither the imbalance in the rotor system nor the damping is large, the critical speed can be accurately and conveniently determined by acceleration past the critical speed and making use of the "inflection" phenomenon.

For the lightly damped rotor with large imbalance or pronounced errors in shaft shape, or if there is mixing in of a higher order vibration, one can use the method of the vibration mode circle, and eliminate the effect of constant error vectors.

For the heavily damped rotor, with the exception of the case where there is crowding of several orders of critical speeds, the critical speed can be determined from the characteristic of a 90° phase lag between the direction of the imbalance and the direction of steady-state vibration.

In the case of a rotor with asymmetrical stiffness, where the sub-critical phenomenon is pronounced, the critical speed can be determined from the sub-critical speed measured under the conditions of low-speed steady-state motion or low acceleration. The special merit of this method lies in the low speeds used.

The critical speed of those rotors with small moment of inertia, in which the stiffness of the connections will not be greatly affected by high temperatures or high speeds, can be determined from the resonance frequency of the two-dimensional bending vibration of the rotors.

We have repeatedly used all of the above methods except the method of the vibration mode circle, and have accumulated a fair amount of experience.

REFERENCES

1. Yen Li-tang: "On the Balancing of High-Speed Rotors in Engines," Scientific Research Reference Materials of Beiching Institute of Aeronautics and Astronautics, BH-C306, 1978, 7.

2. H. L. Hassenpflug, R. D. Flack, E. J. Gunter: "Influence of Acceleration on the Critical Speed of A Jeffcott Rotor," Trans. of the ASME, Journal of Engineering for Power, Vol. 103, No. 1, pp. 108-113.
3. R. E. D. Bishop and A. G. Parkinson: "On the Isolation of Modes in the Balancing of Flexible Shafts," Proceedings of the Institution of Mechanical Engineers, Vol. 177, No. 1-20, 1963.
4. D. B. Herlotz, translated by Yen Li-tang, Hsieh Chu-hsu et al: "Theories and Computations on Aircraft Engine Vibrations," Beiching Institute of Aeronautics and Astronautics Engine Structure Research and Instruction Room, 1979.
5. Translated by Ting Shih: "Critical Speeds of Shafts," China Industries Publishing House, 1962.

Liu Wei
(Chilin University)

Hsiung Ch'ang-ping
(Beijing Institute of Aeronautics and Astronautics)

Abstract

It is important but also difficult to study three-dimensional elastoplastic finite element analysis of aeroengine structures, which have a complex configuration and various heavy loads. The stress distribution in the engine structure is a necessary datum for fracture mechanics and fatigue damage. For this reason the stresses in elastic and plastic zones deserve to be taken into account in many engineering fields.

In order to ensure adequate accuracy, a three-dimensional 20-nodes isoparametric element is selected and a straightforward numerical solution method--an efficient method of frontal solution--is adopted. For saving computational time and reducing main memory space, a cubic fourteen points Gaussian integral is applied. Moreover, with the aim of economizing man-power and gaining quite high accuracy the cubic finite element meshes are automatically generated.

The programming is also discussed in general, including constitutive equations, solution algorithm and strategy for solving large problems. Practice has shown that the program written by the authors is very advantageous to solving elastoplastic problems.

Two typical specimens for experimental investigation are provided: a notched thick plate in which the local stresses are higher

Received October 1981

than the nominal applied stresses, and a thick plate with a central hole in which the stress distribution along the inside edges is also higher than that of the other places. The theoretical analyses and the experimental results coincided favorably.

I. Introduction

Recently great interest has been shown in the problem of /53 elastoplasticity in this and other countries, and a lot of research has been carried out on this subject. The appearance of finite element analysis and the use of computers have made possible great progress in the study of elastoplasticity, so that improved and more nearly accurate knowledge has been obtained about structural design limits, plastic stress fatigue, extension of the tip of a crack, etc.

The increment equation for elastoplastic finite elements as obtained from the variational principle [1, 4, 5] can be solved by the method of initial load, by varying the stiffness, or by the method of first- or second-order self-rectification [2]. Accurate results can be obtained by taking Prager's effect into consideration, while using various theories [6, 7, 9] on hardening in the computation, and by step-wise linearization of the non-linear equations, along with continual modifications.

The structure of the various complex parts of an aeroengine can be realistically analyzed only by means of three-dimensional elements. The stress distribution is very complicated, and the equations are of high orders, hindering the task of elastoplastic analysis. With these points in mind, we have made improvements both in the design of the program and in the computational method, so that problems of a medium scale can be handled on the FELIXC-256 machine.

II. Fundamental Equations

The well-known equation of elastoplastic stress is

$$\{\sigma\} = [D^p] \{\varepsilon\} \quad (1)$$

In the equation, $[D^{ep}] = [D^e] + [D^p]$, $[D^e]$ is the constant-coefficient elasticity matrix, and $[D^p]$ is a function of stress. Therefore, the stress $\{\sigma\}$ and the strain $\{\varepsilon\}$ are non-linearly related. $[D^p]$ is expressed as [1]:

$$[D^p] = - \frac{[D^e] \left\{ \frac{\partial f}{\partial \sigma} \right\} \left[\frac{\partial f}{\partial \sigma} \right]^T [D^e]}{\frac{1}{\lambda} + \left[\frac{\partial f}{\partial \sigma} \right]^T [D^e] \left\{ \frac{\partial f}{\partial \sigma} \right\}} \quad (2)$$

Under the condition of combined load addition and removal, it is appropriate to use the increment theory in the description of the structural equation and the computation of circulative stress. The increment form of Eq. (1) is /54

$$\{d\sigma\} = [D^p] \{d\varepsilon\} \quad (3)$$

Computations on the hardening materials used in engines are usually performed with the help of various hardening models, such as the isotropic hardening model, the moving hardening model, and the modified hardening model. Fig. 1(a) shows the

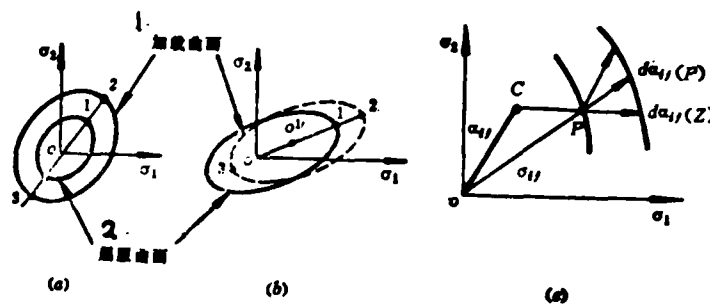


Figure 1. Three hardening models

Key: 1) Curved surface representing added load; 2) Curved surface representing submission.

isotropic hardening model. The curved surface representing submission expands outward uniformly in the plastic flow, and maintains its original shape, orientation and location of the origin. Hence, the submission function on this surface is given by:

$$f(\sigma_{ij}) = K = F(W_p) \quad (4)$$

In the above equation, K is a certain constant, and $F(W_p)$ is plastic work. This model cannot be used to compute Prager's effect, but is easy to apply. Figure 1(b) gives the moving hardening model [6], in which the shape and size of the submission surface remain the same, but the origin is displaced along the direction of the plastic strain increment. Prager's effect can be taken into account here. The submission function of this model is given by

$$f(\sigma_{ij} - \alpha_{ij}) = K^2 = \text{const} \quad (5)$$

where α_{ij} denotes the amount of displacement of the origin in the various directions, and $d\alpha_{ij} = C d\epsilon_{jj}^p$. Figure 1(c) shows the model [7] obtained by modifying the moving hardening model. The contortion of the curved surface can be taken into account with this model, where the plastic flow is in the direction of the sum vector \vec{CP} of the increment vector \vec{OC} of the origin and the stress vector \vec{OP} . The submission function of this model is

$$f(\sigma_{ij} - \alpha_{ij}) = K^2 \quad (6)$$

In the equation, K is not a constant, and $d\alpha_{ij} = (\sigma_{ij} - \alpha_{ij})d\mu$, $d\mu > 0$.

The non-linear increment equation derived from the variational principle can be written as

$$\{K'\} \{\Delta\delta\} = \{\Delta F\} - \{\Delta R\} \quad (7)$$

In the above equation, $\{\Delta R\}$ is equivalent to a kind of virtual load. It is the stress-strain function in the previous iteration, i.e.,

$$\{\Delta R\} = \int_v [B]^T [L^*] \{\Delta e\} dv \quad (8)$$

Thus we see that every time Eq. (7) is solved, the $\{\Delta R\}$ in it is always related to the stress-strain increment.

It is in general considered appropriate to use three-dimensional 20-node isoparametric elements to analyze a three-dimensional structure. However, the three-dimensional problem requires a large interior capacity of the computer. The computation is time-consuming, and is complicated by the iterative procedure applied to the solution of the nonlinear equations. Hence, we have adopted the following measures:

- 1) Reduce the number of integration points from the usual 27 to only 14. It has been shown via examples [18] that the results obtained by the two methods differ only by about 1 part in a thousand, while the latter cuts computational time to one-half of that required by the former.
- 2) Improve the method of frontal solution. The use of the method of frontal solution enables one to fully utilize the peripherals of the machine. When solving for the stiffness coefficient, one can store most of the data on magnetic disk, leaving in the interior only a small amount of information immediately needed in the computation. Thus, the elasticity and plasticity can be handled side by side, and whether the method of initial load or that of varying stiffness is employed, only a small amount of variables needs to be input. /55
- 3) Calculate the stress at the Gaussian points. It can be shown that the most accurate values for stress are those

obtained at these points. As the order in which the material enters into plasticity is also calculated at these points, it is not necessary to calculate the stress at the nodal points. We have thus eliminated the computation required to extrapolate the stress from the Gaussian points to the nodal points.

- 4) The finite element mesh information is automatically generated. This method of automatic information generation is applicable to all complex three-dimensional structures. All one needs to do is to input a few characteristic values of the shape, and the mesh information of the element can be obtained by applying the frontal solution method to the sequence number of the elements and the nodes and the coordinates of the nodes. This information is sequentially recorded on the magnetic disk.

III. Results and Analysis

To examine the reliability and accuracy of our method, we did experiments on the plasticity of two typical types of thick plates, and carried out many calculations.

1. Experiment and calculations on a thick plate with a hole in the center: The dimensions of the plate and the stress-strain curve for a point at the edge of the hole are shown in Figure 2. The material used is Lyl2-CZ. The computed points and the experimental points all fall on a smooth curve. When the symmetry of the structure is employed in the computation, a quarter-model is used, which is divided into 32 solid isoparametric elements, with a proper increase in density near the edges of the hole.

The points of measurement are taken to be on the Gaussian points of the elements as much as possible. To ensure the accuracy

of the positions of the points of measurement, the symmetry of the structure is employed to disperse these points in the corresponding regions on the opposite sides.

Figure 3 gives the diagram of extension of the plastic region under the conditions of the various stress ratios σ_m/σ_s , as obtained separately from computation and experiments. As the stress is concentrated at the edges of the hole, submission starts when $\sigma_m/\sigma_s = 0.59$. With the increase in load, the computed diagram of extension of the plastic region agrees completely with that obtained experimentally. In the figure, "." denotes a calculated point or an experimental point.

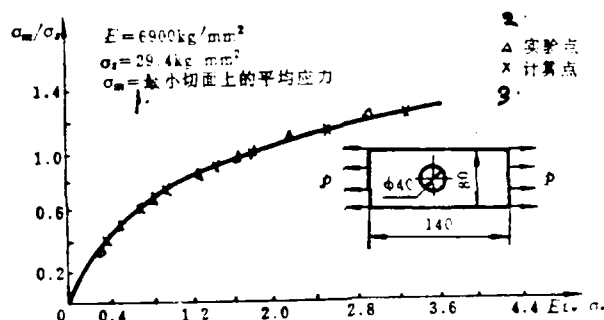


Figure 2. A stress-strain curve of a given point on the edge of a central hole in a plate.

Key: 1) Average stress on the smallest tangential surface;
2) Experimental point; 3) Calculated point.

2. Experiment and calculations on a thick plate notched on two opposite sides: The dimensions of the plate and the experimental curve for a point on the edge of a notch are shown in Figure 4. As above, a quarter model is adopted, and 32 elements are taken. Application of the strain gauge and other procedures are the same as for the first example. The points on the edges of the notch go into the state of plasticity first

when the stress ratio is 0.59. Figure 5 shows the extension of the region of plasticity for various stress ratios (σ_m/σ_s). The calculated curves agree extremely well with the experimental curves. The results are very satisfactory.

In this country, experiments on elastoplastic stress-strain measurements have mainly been limited to the two-dimensional problem. Little work on the three-dimensional problem has been done. To ensure the reliability of the data, we attack the problem in steps: solve for elasticity \rightarrow solve for plane elastoplasticity \rightarrow do experiments on plane elastoplasticity \rightarrow compute for three-dimensional elastoplasticity. After these reliable experiments and calculations have been performed, the results can be used as a basis for studying the complex problem of engine structure using our method. /56

The methods commonly used in this country for measuring plastic strain include the method of microscopic study of hardening [17], the grating fringe method and the use of a strain gauge. The method of microscopic study of hardening consists of the determination of stress-strain values from measurements on hardening of the plastic region with the help

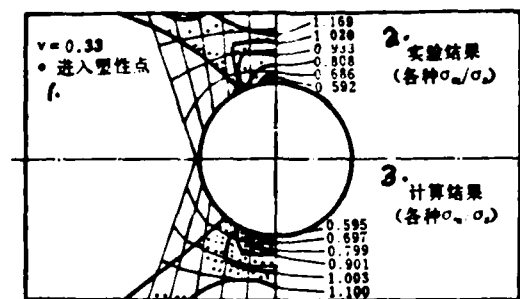


Figure 3. Comparison of the calculated curves with the experimental ones of a plate with a central hole.

Key: 1) Point of entrance into plasticity; 2) Experimental results (for various σ_m/σ_s); 3) Computed results (for various σ_m/σ_s).

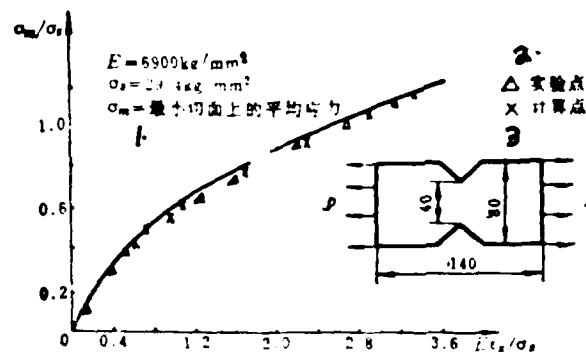


Figure 4. A stress-strain curve of a given point on the edge of a notch in a thick plate notched on opposite sides.

Key: 1) Average stress on the smallest tangential surface;
2) Experimental point; 3) Calculated point.

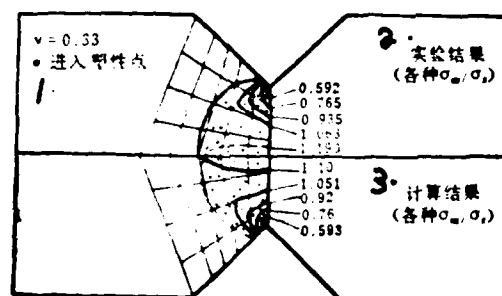


Figure 5. Comparison of the calculated curves with the experimental ones of a notched plate.

Key: 1) Point of entrance into plasticity; 2) Experimental results (for various σ_m/σ_s); 3) Computed results (for various σ_m/σ_s).

of an electronic microscope. This method is not realizable in /57 ordinary laboratories, because of the equipment required and the amount of time and difficulties involved. In the grating fringe

method, one measures by means of optical photography the large plastic deformation of a metal during the process of punching and hot crushing. This method is more suitable for measuring large plastic deformations. Neither of these two methods can be conveniently applied to measurements on small local plastic deformations.

Based on our past experience with point-type strain gauges (1 x 1 mm) and careful investigations, we have chosen specially designed point-type strain gauges made with copper-foil wires. Before applying the strain gauges to the specimen, the positions of the calculated points are first located. The specimen is washed and dried, and the strain gauges are attached to it by means of a metallic adhesive. Care is taken so that the specimen is not exposed to heat or moisture, and measurements are taken right after the strain gauge is attached.

The experiments are performed on a 10-ton universal testing machine. The load is evenly increased after the material enters into plasticity. The instruments used are the common pre-adjusted balance box and static resistance strain indicator. The value of strain is recorded after each addition of load. Because measurements have to be made at a large number of points (in both the x and y directions), the data have to be recorded by many people at the same time so as to prevent data drifting. Repeated tests show that accurate results can be obtained for regions with small plastic deformation. When the plastic deformation is large, the strain gauge itself may enter plastic deformation, and in some cases come off the specimen. Therefore, we see that the method employed depends on the material being tested and the range of plastic deformation involved.

3. Three-dimensional extension of the plastic region on the tip of a type I crack: The rule of extension of plastic regions is a key point of interest in the study of plastic breakdown criteria. We choose the three-dimensional model

shown in Figure 6. Its dimensions are $2b \times 2c \times t = 15 \times 15 \times 8$ (mm). The material is Lyl2-CZ, and the physical parameters are the same as those given in example 1.

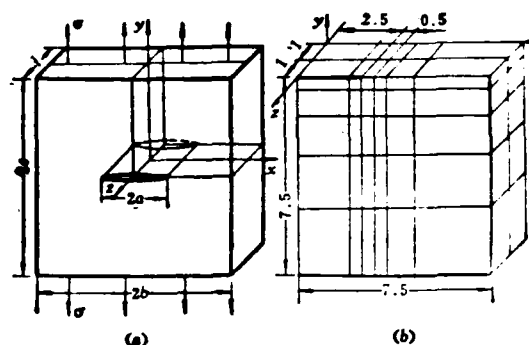


Figure 6. Three dimensional calculation model of a type I crack.

Making use of the symmetry of the structure, we carry out calculations on one-eighth of the model. The mesh of the elements is as shown in Figure 6(b). The crack has length $2a = 5$ mm, and is under a uniform tensile stress. The mesh is decreased toward the tip of the crack, with the smallest side measuring 0.5 mm. The finite element meshes are automatically generated by means of a geometric series. In all, there are 60 elements and 424 nodes. The elements have regular shapes, and the ratios of their length, width and height are within the allowable range of values, so that desirable element characteristics are ensured.

Figure 7(a) shows the extension of the plastic region along the direction of the thickness of the plate. The curves extend from the center to the sides, and have a flaring shape. With increasing load (σ_m/σ_s numbered 1, 2, 3 and 4), the plastic region gradually goes deeper into the plate. Figure 7(b) shows the extension of the plastic region on the surface of the thick plate near the tip of the crack. It can be seen from the figure that the plastic region on the surface of a three-dimensional plate

is very similar to that of the two-dimensional problem. This is due to the fact that the stress condition on the surface of the three-dimensional plate closely approximates that on a plane. Figure 7(c) is a typical solid diagram of a three-dimensional plastic region. This plastic region is symmetrical with respect to the tip of the crack, and extends outward forming a "kidney" shape. The size of the "kidney" shape undergoes an appreciable change along the thickness of the plate.

We now compare the two-dimensional plastic region of the type I crack with the three-dimensional result. The stress field is known to be:

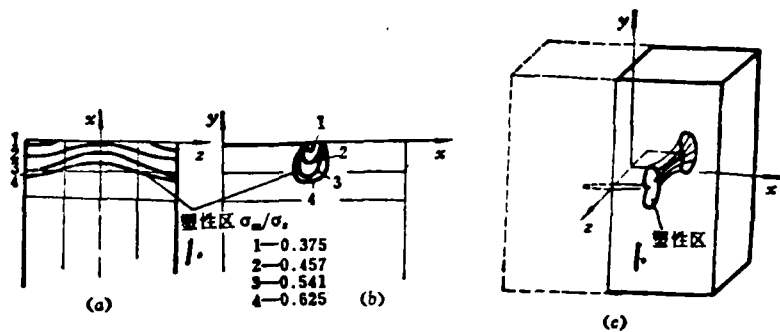


Figure 7. Three dimensional extension of a plastic region.

Key: 1) Plastic region.

$$\begin{aligned}
 \sigma_x &= \frac{K_I}{\sqrt{2\pi r}} \cos \frac{\theta}{2} \left(1 - \sin \frac{\theta}{2} \sin \frac{3\theta}{2} \right) \\
 \sigma_y &= \frac{K_I}{\sqrt{2\pi r}} \cos \frac{\theta}{2} \left(1 + \sin \frac{\theta}{2} \sin \frac{3\theta}{2} \right) \\
 \tau_{xy} &= \frac{K_I}{\sqrt{2\pi r}} \sin \frac{\theta}{2} \cos \frac{\theta}{2} \cos \frac{3\theta}{2} \\
 \sigma_z = \tau_{xz} = \tau_{yz} &= 0
 \end{aligned} \tag{9}$$

After the specimen enters into plasticity, the V. Mises criterion is applied:

$$\bar{\sigma}_s = \frac{1}{\sqrt{2}} \{ (\sigma_x - \sigma_y)^2 + (\sigma_y - \sigma_z)^2 + (\sigma_z - \sigma_x)^2 + 6(\tau_{xy}^2 + \tau_{yz}^2 + \tau_{xz}^2) \}^{1/2} \tag{10}$$

Substituting Eq. (9) into Eq. (10), we obtain:

$$r = \frac{K_1^2}{2\pi\sigma_y^2} \cos \frac{\theta}{2} \left(1 + 3 \sin \frac{2\theta}{2} \right) \quad (11)$$

where r is a dimension of the plastic region. The "kidney"-shaped region is obtained by plotting in polar coordinates, as shown in Figure 8. When $\theta = 0^\circ$

$$r_0 = -\frac{K_1^2}{2\pi\sigma_y^2} \quad (12)$$

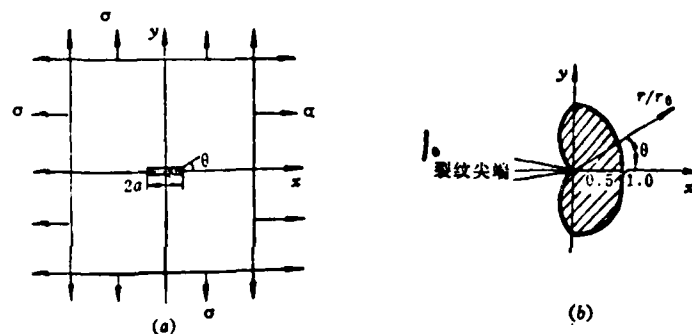


Figure 8. Two-dimensional plastic region of a crack under uniform tensile stress.

Key: 1) Tip of crack.

IV. Conclusions

1. The study in this paper is based on the study of plane and axially symmetric elastoplasticity. This is why we have been able to reduce the difficulty associated with the three-dimensional elastoplastic problem and increase the reliability and accuracy of the results.

2. In order to facilitate the application of three-dimensional computation of elastoplasticity to practical engineering

problems, we have adopted a series of measures to minimize interior memory requirements, reduce computing time and increase accuracy of computation. These measures may represent a breakthrough in the study of the three-dimensional non-linear problems of materials.

3. The present method and procedure can be used in the computation of three-dimensional problems of different types of complex structures, in calculations performed on parts with complex load (bulk load, surface load and concentrated load), and in finding the dimensions and rule of extension of the plastic region of the tip of a crack (type I, II or III). To realize the various objectives, one only needs to change the automatic element partition and the characteristics of the load. No changes need to be made when the method is applied to the problem of plane and axially symmetric elastoplasticity.

4. When the necessary changes have been made, this method can also be applied to the calculation of circulative loads and the study of plastic fatigue.

5. Because of limited machine capability, we have not been able to include the high-temperature effects (which require the calculation of the temperature field). However, the present method provides an important basis for the study of such high-temperature effects on engine plasticity and deformation.

REFERENCES

1. Plastic Stress-Strain Matrix and its Application for the Solution of Elastic-Plastic Problems by Finite Element Method, Y. Yamada, N. Yoshimorai and T. Sakarar, Int. J. Mech. Sci. Vol. 10, 343-354, 1968.
2. Numerical Methods for the Solution of Nonlinear Problems in Structural Analysis, Jr. R. Tillerson, J. A. Stricklin, W. E. Haisler, ASME AMD-6, 1973.
3. Assumptions, Models and Computational Method for Plasticity, H. Armen, Int. J. Comp. and Struct. Vol. 10, Nos. 1/2, 1979.
4. Dual Analysis in Elasto-Plasticity, Finite Elements in Nonlinear Mechanics, C. Nyssen, P. Beskers, 1977 (1).
5. Variational Principles for Elasto-Plastic Continua, Eggers, J. Struct. Mech. 3(4), 1974-1975, p. 345-358.
6. The Theory of Plasticity: A Survey of Recent Achievements, W. Prager, Proceedings of the Institution of Mech. Eng., Vol. 169, 1955.
7. A Modification of Prager's Hardening Rule. H. Ziegler, Quarterly of Applied Mathematics, Vol. 17, No. 1, 1959.
8. Finite Element Analysis of Elastic-Plastic Materials Displaying Mixed Hardening. K. Axelsson and A. Samuelsson, Int. J. Num. Math. Engng., Vol. 14, 211-115, 1979.
9. On the Description of Anisotropic Work-Hardening, Z. Mroz, J. of the Mech. and Phy. of Solids, Vol. 15, p. 163, 1967.
10. The Finite Element Method in Engineering Science, O. C. Zienkiewicz, McGraw-Hill, New York, 1971.

11. A Frontal Solution Program for Finite Element Analysis, B. M. Irons, Int. J. Num. Meth. Engng., Vol. 1, 5-32, 1970.
12. Concepts and Applications of Finite Element Analysis, D. Cook, 1973.
13. Three-dimensional Stress Analysis of Crowned Hollow Cooled Blades, Hsiung Ch'ang-ping, Hsiao Chun-hsiang et al., Technology and Practice, No. 2, 1980.
14. Finite Element Stress Analysis of Axially Symmetric Elastoplasticity, Structures Team of the Structural Mechanics Laboratory of Cheng Chou Institute of Mechanics, Department of Mathematics of Fudan University, 1979.
15. Principle and Application of Finite Element Analysis, Chu Po-fang, Shueili Publishing House, 1979.
16. An Effective Computational Method of Finite Element Analysis, Huang Ming-yu, Kao T'ieh-mei et al., Numerical Calculations and Computer Applications, Vol. 1, No. 1, 1980.
17. A Study of the Strain and Stress at the Tip of a Crack, Yu Chih-sheng and Ch'en Ch'ih, Chin Shu Hsueh Pao, Vol. 14, No. 3, 1978.
18. Applications of Finite Element Analysis, Hsiung Ch'ang-ping and Hsiao Chun-hsiang, Peiching Hang K'ung Hsueh Yuan Hsueh Pao, 1981, 3.

Jen Szu-tsung
(Northwestern Polytechnical University)

Chao Yung-k'ang
(Paoch'eng Instrument Factory)

Abstract

A new type of inertial navigation system combining the customary platform type with the strapped-down type is put forward. In this system the azimuth rate platform without azimuth-stabilizing loop, coordinate resolver and azimuth synchronizer is adopted. The azimuth angles of platform and vehicle will be obtained by an integrator from azimuth rate signals measured by an azimuth gyroscope supported on a horizontal gimbal. This type of inertial navigation system is suitable for vehicles without large-pitching maneuver, such as transports and aerodynamic and ballistic missiles.

Operational principles of the azimuth rate platform, mechanization equations, distinguishing features of initial alignment, and calibration and compensation for drifts of gyroscopes are discussed in this paper. Error propagation characteristics caused by various error sources for navigation positioning, velocity and attitude are simulated on a digital computer. Simplicity in platform structure, small volume and weight, high reliability, possibility of calibration and compensation for drifts of the azimuth gyroscope are the distinctive advantages of this inertial navigation system.

Moreover, by using a specific optical system and referring to given azimuth angles of landmarks and geographical latitudes, it is possible to accomplish not only fast alignment, but also calibration and compensation of horizontal gyroscope.

I. Statement of the Problem and Brief Description of Platform Structure

The inertial navigation and guidance systems widely used in aeronautics, navigation and aerodynamic missiles are of diverse kinds. Basically, however, these can be grouped into two major types: the platform type and the strapped-down type.

The fundamental characteristic of the platform type system is that it has a stabilizing loop which, via a gimbal, separates the inertial components from the motion of the vehicle. Thus the inertial components operate under favorable conditions and have relatively small dynamic ranges. In particular, the effect of gravitational acceleration is reduced to a minimum in semi-analytical systems working in the ground coordinate system, and the relations used in the calculations are simpler, with the result that the systems work with high accuracy. Nevertheless, the platform type system has certain disadvantages, such as complexity of structure, high manufacturing cost, relatively large volume and heavy weight, and a large number of gimbals and conducting rings that have an adverse effect on reliability.

The inertial components of the strapped-down type system are directly attached to the vehicle. Thus the system has a simple structure, high reliability, and high accuracy due to the fact that attitude information need not be transformed via electro-mechanical elements. However, such a system operates under unfavorable conditions, especially when the vehicle undergoes violent motions, with exacting requirements on the dynamic range, and especially on the gyroscope. Moreover, because the direction of the relative gravitational field of the inertial components is constantly changing, compensation for error and gravitational effect is a complicated process. This places a higher requirement on computer wordlength, speed and memory capacity. Thus, the accuracy of the strapped-down system cannot be ensured without great difficulties.

For most vehicles, owing to specific reasons related to structure and dynamics, there is a large difference between the angular rate of the rolling motion and that of the course-changing motion. For example, the rolling angular rate of an airplane may reach or exceed 360 degree/second while its course-changing angular rate is usually around 2-3 degree/second, with /62 a maximum value not over 10 degree/second. Hence, even if one can say that an angular rate of 10 degree/second can be sensed with a regular inertial gyroscope without great difficulty, this is not the case with angular rates exceeding 360 degree/second. In order to fully utilize the merits of the platform type and strapped-down type inertial navigation systems, we present below a new azimuth rate inertial navigation system that has a simplified platform, reduced manufacturing cost and improved reliability. The platform of this system does not contain the azimuth-stabilizing loop, the coordinate resolver and azimuth synchronizer. The azimuth angles of the platform and the vehicle are obtained by an integrator from the azimuth rate signals measured by an azimuth gyroscope supported on a horizontal gimbal.

When this type of system was first proposed in 1978, it was named "strapped-down azimuth inertial navigation system" or "semi-strapped-down inertial navigation system." Generally speaking, to simplify the platform, one could also have a "strapped-down pitching system" or even an "azimuth and pitching strapped-down system" that contains only one rolling-stabilization axle. However, one needs to take into consideration the fact that it is most advantageous to use this type of system in the semi-analytical inertial navigation system with horizontal coordinates that has low azimuth angular rate. This system is fundamentally similar to "rotating azimuth," "free azimuth" and "floating azimuth" systems. In addition, when the platform has an error in attitude, the azimuth gyroscope is not completely "fixed" to the vehicle, so that the term "strapped-down" loses its meaning. Therefore, we switched to the name "azimuth rate" or "analytical azimuth" inertial navigation system.

The external features of the rate azimuth platform are as shown in Figure 1. The platform can be made up of two gyroscopes with two degrees of freedom, or one angular rate with one degree of freedom and one gyroscope with two degrees of freedom, or one angular rate with one degree of freedom and two integrating gyroscopes each with one degree of freedom.

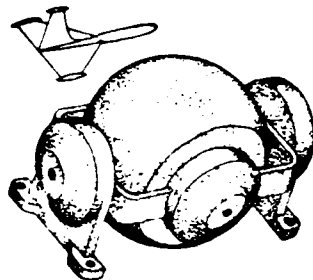


Figure 1. Configuration of the azimuth rate platform.

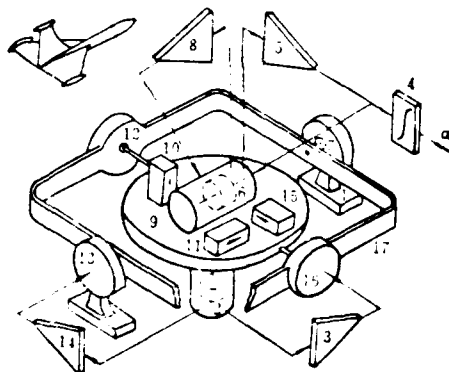


Figure 2. Scheme of the azimuth rate platform.

Figure 2 is a schematic diagram of the azimuth rate platform made of two gyroscopes with two degrees of freedom. The two gyroscopes, 2 and 6, and the three accelerometers, 10, 11 and 15, are mounted on the platform 9 to form the inertial measuring component supported by the horizontal gimbal 17, which is, in turn,

supported by stands attached to the vehicle 1. In its normal operating mode, the axle of gyroscope 2 is vertically oriented. It stabilizes the pitching and rolling axles of the platform via the corresponding amplifiers 3 and 14, and the corresponding stabilizing circuits 16 and 13. The main axle of gyroscope 6 is orthogonal to that of gyroscope 2, and brings about self-locking via the amplifiers 5 and 8 in the feed-back loops. It operates at the given rate. The feed-back current of the circuit around the azimuth axle is a measure of the rate of change of the azimuth angle. Thus, the azimuth angle can be obtained by passing this signal through the integrator 4. As the support axle of the horizontal gimbal is parallel to the longitudinal axis of the vehicle, the angle-sensing component 7 can output rolling signals. Similarly, the pitching signals are obtained from the angle-sensing component 12. It is clear that the structure of the platform is thus very much simplified. However, if the pitching angle is expected to exceed 60° , one needs to add to it an external rolling loop and the corresponding stabilizing circuit so that its operation will not be affected by the dynamic motion of the vehicle.

If the azimuth rate inertial navigation system is not to be used in vehicles that undergo full-cycle rolling and pitching, then there will be no need to use conducting rings, and soft conducting wires can be used in all parts of the platform. This will result in a simplified platform structure, ease of maintenance and improved reliability.

/63

As the azimuth rate gyroscope operates under conditions similar to those in a strapped-down system, it may have an increased error in the assigned coefficients and increased non-linearity as compared to the gyroscope in an ordinary platform because of the large dynamic range. Nevertheless, the accuracy of the azimuth gyroscope operation can be easily ensured because of a reduced gravitational effect brought about by the shock-proofing action of the horizontal gimbal, and the fact that the

platform is basically horizontal. Furthermore, when the pulsed rebalancing loop is used, additional errors due to transformation can be avoided.

II. Mechanization Equations and Block Diagram of Structure

Choose the geographical coordinate system NWV, where N stands for north, W stands for west, and V stands for the skyward direction. As shown in Figure 3, the ideal platform system $X_T Y_T Z_T$ rotates about the vertical axis V, along with the vehicle. The angle formed by X_T and the meridian N is the azimuth angle of the platform, α .

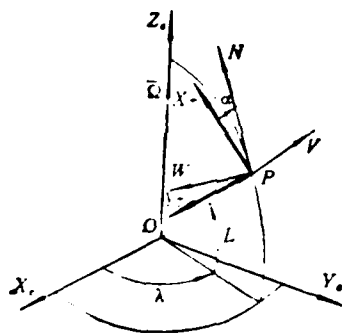


Figure 3. Coordinate system.

The velocity of the platform relative to the earth is determined by the following set of equations:

$$\begin{aligned} \dot{V}_x &= f_x - (2\Omega_y + \omega_y)V_z + (2\Omega_z + \omega_z)V_y \\ \dot{V}_y &= f_y - (2\Omega_z + \omega_z)V_x + (2\Omega_x + \omega_x)V_z \\ \dot{V}_z &= f_z - (2\Omega_x + \omega_x)V_y + (2\Omega_y + \omega_y)V_x - g \end{aligned} \quad (1)$$

where f_i is the force as sensed by the accelerometer;

Ω_i is a component of the angular rate of the earth's spin;

- ω_i is a component of the angular velocity of the rotation of the platform relative to earth;
- g is gravitational acceleration; and b denotes the angular rate of the platform due to the motion of the vehicle.

The computation for the navigation can be carried out with the help of the relation that holds among the directional cosine matrix $[C]$, its rate of change, and ω_i , where the longitude λ , latitude L and azimuth angle α are the angles indicating the relative orientation of the platform system with respect to the geographical coordinates:

$$[\dot{C}] = [C][\omega] \quad (2)$$

In the above equation,

$$[C] = \begin{bmatrix} \sin \lambda \sin \alpha & \sin \lambda \cos \alpha & \cos L \cos \lambda \\ -\sin L \cos \lambda \cos \alpha & \sin L \cos \lambda \sin \alpha & \cos L \sin \lambda \\ -\cos \lambda \sin \alpha & -\cos \lambda \cos \alpha & \sin L \\ -\sin L \sin \lambda \cos \alpha & \sin L \sin \lambda \sin \alpha & \cos L \\ \cos L \cos \alpha & -\cos L \sin \alpha & \sin L \end{bmatrix} \quad (3)$$

/64

$$[\omega] = \begin{bmatrix} 0 & -\omega_z & 0 \\ \omega_z & 0 & -\omega_x \\ -\omega_y & \omega_x & 0 \end{bmatrix} \quad (4)$$

Obviously, ω_x and ω_y are the control quantities as calculated by the computer from V_Y and V_X and the curvature of the earth, and they are applied to the gyroscope to keep it level; whereas ω_{zb} can only be obtained by subtracting Ω_{zb} from the azimuth rate feed-back control rate ω_{czb} , i.e.,

$$\omega_{zb} = \omega_{czb} - \Omega_{zb} \quad (5)$$

Furthermore, if one considers the height information from atmospheric pressure and the information given by the vertical accelerometer as forming one combined height system, then the

mechanization of the azimuth rate inertial navigation system can be represented by the block diagram shown in Figure 4.

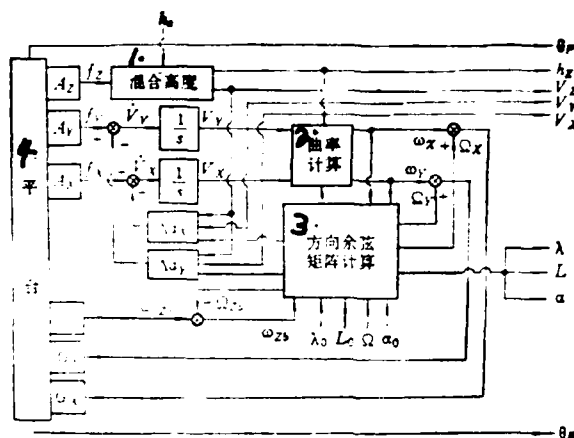


Figure 4. Block diagram of the azimuth rate inertial navigation system.

Key: 1) Combined height system; 2) Curvature computation; 3) Computation of directional cosine matrix; 4) Platform; 5) A_i , G_i --accelerometer and gyroscope of the corresponding axle; h_a --height information from atmospheric pressure; θ_p , θ_R --pitching and rolling attitude information; λ_0 , L_0 --initial latitude and longitude; Ω --angular rate of earth's spin.

III. Distinguishing Features of the Initial Alignment of the Azimuth Rate Platform

If imperfections in the structure are neglected, then the azimuth of the ideal platform system will be that of the parked vehicle. Thus, if the azimuth of the parked vehicle is specified by means of some signs or marks placed on the runway or parking area, then not only can fast alignment be achieved, but calibration and compensation can be carried out for all the gyroscopes. In order to explain the problem, we need to set up the attitude

error equations first. When the attitude error angles are considered as small quantities, one obtains

$$\dot{\bar{\varphi}} = \bar{\omega}_p - C_T^p \bar{\omega}_T \quad (6)$$

In the above equation, $\bar{\varphi}$ is the vector representing the attitude error angle. $\bar{\omega}_T = \bar{\Omega} = [\Omega_X \ \Omega_Y \ \Omega_Z]^T$ is the angular velocity vector of the ideal platform.

$$C_T^p = \begin{bmatrix} 1 & 0 & -\varphi_y \\ 0 & 1 & \varphi_x \\ \varphi_y & -\varphi_x & 1 \end{bmatrix} \quad \text{is the attitude error matrix.}$$

$\bar{\omega}_p = \bar{\omega}_c + \bar{\omega}_{zpp} + \bar{E}$ is the vector representing the angular rate of rotation of the platform system.

$\bar{\omega}_c = [\omega_{xc} \ \omega_{yc} \ 0]^T$ is the control applied to the platform. /65

$\bar{\omega}_{zbp} = [0 \ 0 \ \Omega_{zbp}]^T = [0 \ 0 \ \varphi_y \Omega_X - \varphi_x \Omega_Y + \Omega_Z]^T$ is the angular rate of rotation of the platform due to the vehicle. $\bar{E} = [E_X \ E_Y \ 0]^T$ is the angular rate of drifting of the platform.

Substituting the appropriate relations into Eq. (6), one obtains

$$\begin{aligned} \dot{\varphi}_x &= \omega_{xc} - \Omega \cos L \cos \alpha + \varphi_y \Omega \sin L + E_x \\ \dot{\varphi}_y &= \omega_{yc} - \varphi_x \Omega \sin L + \Omega \cos L \sin \alpha + E_y \\ 0 &= \Omega_{zbp} - \varphi_y \Omega \cos L \cos \alpha + \varphi_x \Omega \cos L \sin \alpha - \Omega \sin L \end{aligned} \quad (7)$$

This equation shows that the azimuth attitude error undergoes no change during the initial alignment of the azimuth rate platform. This clearly reflects the fundamental characteristics of the initial alignment of the system. Eq. (7) can be represented by means of the block diagram shown in Figure 5. The coefficients K_1 , K_2 and K_3 directly determine the dynamic characteristics of the leveling process, and therefore should be carefully chosen to meet the basic requirements of transit time and interference-proofing.

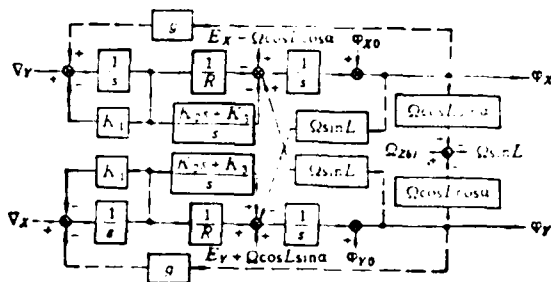


Figure 5. Block diagram of initial alignment loops.

Under steady-state conditions, one obtains from Eq. (7)

$$\omega_{x_s}(\infty) = E_x - \Omega \cos L \cos \alpha \quad (8)$$

$$\omega_{y_s}(\infty) = E_y + \Omega \cos L \sin \alpha$$

From this, the azimuth angle is calculated to be

$$\alpha_s = \operatorname{tg}^{-1} \frac{\omega_{y_s}(\infty)}{\omega_{x_s}(\infty)} = \operatorname{tg}^{-1} \frac{\Omega \cos L \sin \alpha + E_y}{\Omega \cos L \cos \alpha - E_x} \quad (9)$$

Obviously, the drift of the platform has a direct effect on the accuracy of the calculation of the azimuth angle. Assume that

$\alpha_c = \alpha + \Delta\alpha$, and let $\omega_{x_c}(\infty) = \Omega \cos L \cos \alpha_c$ and $\omega_{y_c}(\infty) = \Omega \cos L \sin \alpha_c$. Then, one obtains from Eq. (8)

$$\Omega \cos L \sin \alpha \Delta\alpha = E_x \quad (10)$$

$$\Omega \cos L \cos \alpha \Delta\alpha = E_y$$

Multiplying the above equations by $\sin \alpha$ and $\cos \alpha$, respectively, and adding, one obtains the computational error of the azimuth angle

$$\Delta\alpha = \frac{E_x \sin \alpha + E_y \cos \alpha}{\Omega \cos L} = \frac{E_n}{\Omega \cos L} \quad (11)$$

In the above equation, $E_W = E_X \sin \alpha + E_Y \cos \alpha$ is the effective westward drift of the platform. This conclusion is exactly the same as that arrived at for other systems.

To calculate the compensation for the drift, one can first calculate and compensate with respect to the angular rate of the earth's spin, and then find the effective northward drift to be

$$E_N = \omega_x(\infty) \cos \alpha_0 + \omega_y(\infty) \sin \alpha_0 \approx E_X \cos \alpha_0 + E_Y \sin \alpha_0 \quad (12)$$

Projecting this onto the corresponding axle, one obtains the compensation for the drift to be

$$\begin{aligned} \hat{E}_X &= E_N \cos \alpha_0 \approx E_X \cos^2 \alpha_0 - E_Y \sin \alpha_0 \cos \alpha_0, \\ \hat{E}_Y &= -E_N \sin \alpha_0 \approx E_Y \sin^2 \alpha_0 - E_X \cos \alpha_0 \sin \alpha_0. \end{aligned} \quad (13)$$

The errors in the compensation thus obtained are given by /66

$$\delta E_X = \hat{E}_X - E_X = -(E_X \sin \alpha_0 + E_Y \cos \alpha_0) \sin \alpha_0 \quad (14)$$

$$\delta E_Y = \hat{E}_Y - E_Y = -(E_X \sin \alpha_0 + E_Y \cos \alpha_0) \cos \alpha_0$$

i.e., they are dependent on the effective westward drift which cannot be determined by measurements.

After the platform is leveled, $\Omega_{zb} = \Omega \sin L$ is a known quantity. Given the gyration coefficient K_G of the gyroscope, one can find the compensation for the drift of the azimuth of the platform from the equation $I(\infty) = K_G \Omega_{zb} - E_Z$ relating the controlling current and the azimuth angular rate:

$$\hat{E}_Z = K_G \Omega \sin L - I(\infty) \quad (15)$$

If the azimuth of the runway or certain landmarks is specified beforehand, then the azimuth angle of the platform or the longitudinal axle of the vehicle can be readily determined with a

leveling device, a sighting device or some other special optical system. Thus, not only can one achieve fast alignment, but it will also be possible to calibrate the drift of the platform along the horizontal axle. In fact, assuming the measured azimuth angle introduced into the computer is α_c , one obtains from Eq. (8)

$$\begin{aligned}\bar{E}_x &= \omega_{x_0}(\infty) + \Omega \cos L \cos \alpha - \Omega \cos L \cos \alpha_c, \\ \bar{E}_y &= \omega_{y_0}(\infty) - \Omega \cos L \sin \alpha + \Omega \cos L \sin \alpha_c,\end{aligned}\tag{16}$$

Obviously, if the azimuth angle contains no error, the control quantity under equilibrium will be equal to the drift of the platform. When the error in azimuth is $\Delta\alpha$, one can obtain from the relation $\alpha_c = \alpha + \Delta\alpha$ the error in compensation for the drift:

$$\begin{aligned}\delta\bar{E}_x &= \Omega \cos L \sin \alpha \Delta\alpha \\ \delta\bar{E}_y &= \Omega \cos L \cos \alpha \Delta\alpha\end{aligned}\tag{17}$$

Of course, when the moment-measuring device has high accuracy and the error of the platform structure is small, the compensation is equal to the drift of the gyroscope. It is clear that the accuracies of the azimuth of the platform and the compensation for drift are mainly dependent on the accuracy with which the azimuth of the longitudinal axis of the vehicle with respect to the runway or landmark is measured, and on the accuracy with which the azimuth of the runway or landmark itself has been determined, plus the mounting accuracy of the platform with respect to the vehicle. It can be seen from Eq. (17) that when $\alpha = 0$, $\delta\bar{E}_x = 0$; while when $\alpha = 90^\circ$, $\delta\bar{E}_y = 0$. These relations are exactly the same as those that hold in the calibration of the customary platforms. Furthermore, the accuracy of the latitude introduced into the computer also has an effect on the accuracy of compensation. For example, neglecting the error in latitude, when $L = \alpha = 45^\circ$, in order to keep $\delta\bar{E}_x$ and $\delta\bar{E}_y$ below $0.02^\circ/\text{hr.}$, one needs to ensure that the error in azimuth $\Delta\alpha \leq 12'$. This shows that the present method has a definite practical significance

in cases where the length of the runway or the distance between the landmarks is not very short and where the accuracy of mounting the platform on the vehicle is relatively high. Of course, if the accuracy of the measurement of the azimuth angle can be made to reach about 6' by means of optical methods, then one will be able to compensate for platform drifts approximating 0.01°/hr.

IV. Computer Simulation of Navigation Error

In order to obtain a better understanding of the performance of the azimuth rate inertial navigation system, we perform computations using Eqs. (1) and (2) and the corresponding error relations under the following conditions: the errors in the calibration coefficients of the gyroscope and accelerometer $\Delta K_G = \Delta K_a = 1 \times 10^{-4}$; errors in the structure $\delta_1 = \vartheta_1 = 20''$; gyroscope drifts $\epsilon_X = \epsilon_Y = 0.01^\circ/\text{hr.}$, $\epsilon_Z = 0.02^\circ/\text{hr.}$; deviation of the zero position of the accelerometer $\nabla_X = \nabla_Y = 1 \times 10^{-4}g$; initial velocity $V_{X0} = V_{Y0} = 0$; errors in initial attitude $\varphi_{X0} = \varphi_{Y0} = 5 \times 10^{-4}$ radians; initial values of the theoretical position $L_0 = 40^\circ 05'$, $\lambda_0 = 116^\circ 36'$, $\alpha_0 = 45^\circ 00'$; initial values of the calculated position $L_{c0} = 40^\circ 07'$, $\lambda_{c0} = 116^\circ 38'$, $\alpha_{c0} = 45^\circ 03'$. We assume that the flight course is described by the following parameters:

ers:

	1. (米/秒 ²)	2. (秒)
$a_x =$	3.3	$0 < t \leq 30$
	2.0	$30 < t \leq 60$
	1.0	$60 < t \leq 200$
	0.0	$200 < t \leq 4284$
	-1.0	$4284 < t \leq 4464$
	-3.3	$4464 < t \leq 4500$

	3. (度/秒)	2. (秒)	/67
$\omega_{2x} =$	0.0	$0 < t \leq 60$	
	1.5	$60 < t \leq 240$	
	0.0	$240 < t \leq 4170$	
	-1.5	$4170 < t \leq 4290$	
	0.0	$4290 < t \leq 4500$	

	1. (米/秒 ²)	2. (秒)
$a_y =$	0.0	$0 < t \leq 60$
	$\omega_{2x} V_x$	$60 < t \leq 240$
	0.0	$240 < t \leq 4170$
	$\omega_{2x} V_x$	$4170 < t \leq 4290$
	0.0	$4290 < t \leq 4500$

	3. (米/秒)	2. (秒)
$V_z =$	0.0	$0 < t \leq 30$
	$V_{xtg} 3.5'$	$30 < t \leq 60$
	$V_{xtg} 1.0'$	$60 < t \leq 490$
	0.0	$490 < t \leq 2970$
	$-V_{xtg} 1'$	$2970 < t \leq 4248$
	$-V_{xtg} 3'$	$4248 < t \leq 4464$
	0.0	$4464 < t \leq 4500$

1. 2) (deg) : 3) (degrees/sec)

Key: 1) (m/sec²); 2) (sec); 3) (degree/sec).

The most important results of the computation are shown in Figures 6-10.

Figure 6 shows the flight course of the airplane from taxiing along and lifting off the runway, through circling and cruising, and finally to turning and landing, and the corresponding calculated values. It is clear that the difference between the calculated and theoretical values varies with different flight directions and distances.

Figure 7 gives the time history of position deviation. It can be seen that it undergoes an oscillatory variation. The amplitude of the error in longitude $\Delta\lambda$ is larger than that of the error in latitude ΔL . This is because with increasing latitude, the longitude corresponding to the same distance error will be larger.

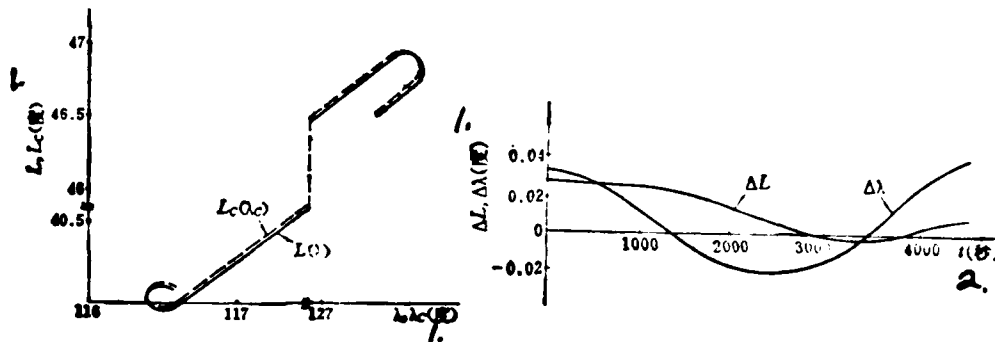


Figure 6. Flight course.
Key: 1) (degree); 2) (sec)

Figure 7. The time history of position deviation.

Figure 8 gives the time history of attitude deviation. It can be clearly seen that the attitude error of the platform undergoes large variations with different azimuth angles owing to the lifting and landing maneuvering. However, its maximum

value is still within the allowable range. In the linear, constant-speed cruising stage, the variation is a periodic oscillation.

/68

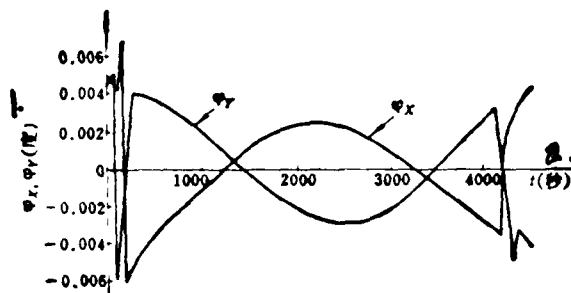


Figure 8. The time history of attitude deviation.

Key: 1) (degree); 2) (sec).

The time history of azimuth deviation is shown in Figure 9. It is clear that the variation of the azimuth deviation is rather slow, with its maximum value not exceeding 0.06 degrees. If one considers that the initial deviation is 3', then the actual variation in the deviation is even smaller. At higher latitudes, the variation in the deviation is slightly larger. This is also in agreement with the general rule. On the whole, this gives a higher accuracy than that of the output obtained by means of such transforming elements as the synchronizer. This explains why the strapped-down system has a smaller attitude deviation than the platform system that outputs via electro-mechanical elements.

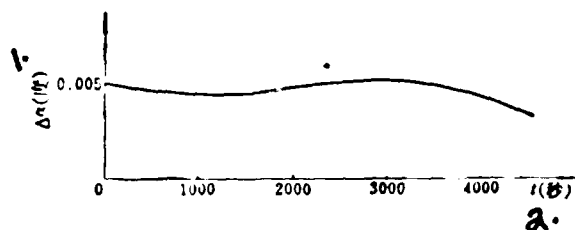


Figure 9. The time history of azimuth deviation.

Key: 1) (degree); 2) (sec).

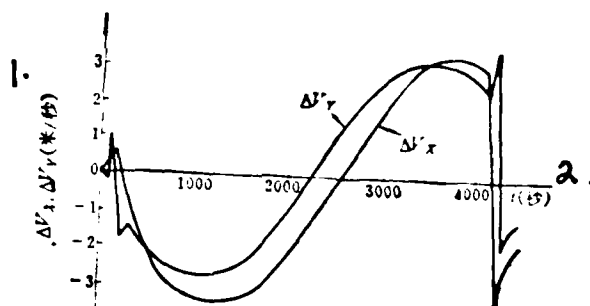


Figure 10. The time history of velocity deviation.

Key: 1) (m/sec); 2) (sec).

Figure 10 gives the time history of velocity deviation. It can be seen that during lifting and landing, the velocity deviation undergoes large variations because of its dependence on the angular rate of circling. However, its period of variation can be calculated from the cruising stage.

V. Conclusion

/69

From the above, it can be seen that the azimuth rate inertial navigation system is better suited for vehicles that do not undergo large pitching and rolling. The system combines the merits of the platform-type and strapped-down-type inertial navigation systems, and avoids certain shortcomings of each of these systems. This type of platform has simplicity in structure (using a small number of components), small volume and weight, high reliability, and the ability to provide azimuth rate signals of the flight instrument directional damping passage. Thus it eliminates the need for a directional damping gyroscope, and is capable of providing more nearly accurate flight direction signals.

Another unique feature of the system is that calibration and compensation can be carried out for platform drift on every alignment. An aspect also worth taking note of is that it is possible to achieve fast alignment, calibration and compensation for horizontal drift by means of a leveling device or other optical systems, making use of the known azimuth of the runway or landmarks.

As the azimuth rate of an ordinary vehicle approximates that of the rotation of the platform in the customary rotational azimuth inertial navigation system, no special requirements need to be placed on the computer of the system. Naturally, the software system approximates that of an ordinary semi-analytical inertial navigation system.

Finally, we would like to point out that, relatively speaking, the disadvantage of the azimuth rate inertial navigation system is that it is not suitable for fighters that perform special stunts. As the platform itself does not have rotational degree of freedom about the azimuth axle, it is not convenient to carry out dual-position calibration and alignment, but only alignment for a single position.

REFERENCES

1. J. C. Hung, Strapped-Down-Type Navigation Platforms, translated by Wang K'ai-Yuan, K'o Hsueh Publishing House, 1979.
2. Technical Description of FERRENTI FIN1018C Inertial NAV/ATTACK Equipment, FERRENTI LTD., 1979.
3. Jen Szu Ts'ung, "Analysis of an Initial Alignment Scheme for a Drifting-Azimuth Inertial Navigational System, Inertial Navigation and Components, No. 2, 1980.

OPTIMAL GUIDANCE LAWS FOR MISSILES WITH
SECOND-ORDER CHARACTERISTICS

/71

Li Chung-ying

(Beihing Institute of Aeronautics and Astronautics)

ABSTRACT

The problem of optimal intercept guidance laws for missiles has been studied by a lot of authors at home and abroad. [1, 3, 4, 5] But the mathematical models for missiles were assumed too simple, i.e., either as an ideal particle or as a first order delay link [1].

As a primary contribution this paper has made researches on the optimal intercept guidance laws based on a mathematical model with second order characteristics. By taking minimum control energy consumption as the performance index, the optimal intercept guidance laws have been derived from the minimum principle in the following two cases of terminal state:

1. The terminal miss-distance is zero;
2. The final state is a zero-control intercepting curved surface.

The conjugate state equations and the state equations have been solved by use of Laplace Transformation. Through considerably complex computation, the optimal intercept guidance laws have been deduced in the following analytical forms

1. $u^*(t_0) = -K(\xi, \omega, t_f)(x_{10} + x_{10}t_f) - L(\xi, \omega, t_f)x_{2,1}$
2. $u^*(t_0) = -K_L(\xi, \omega, T, \mu)(x_{1f} + x_{10}t_f) - L_L(\xi, \omega, T, \mu)x_{2,0}$

Through appropriate selection of the terminal time t_f or the time of lead T , the results obtained above may be transformed

Received in May 1981.

into the optimal guidance laws which are composed of the proportional navigation with varied coefficients and the correctional terms associated with acceleration and the angular rate of change of the line-of-sight. These results are similar to those of missiles with first order delay link in form and have no need of any additional parameter. However, the computation is more complex and the results are more accurate.

Finally, the optimal intercept guidance laws are studied in the case of the proper frequency of a missile ω approaching to infinity, i.e., in the case of an ideal particle. The results are the same as those obtained by the other authors.

Notation

x_1	relative position vector of missile and target
x_2	relative velocity vector of missile and target
x_3	relative acceleration vector of missile and target
x_4	rate of change of relative acceleration vector
u	missile control vector
\bar{u}	optimum missile control vector
ξ	relative damping coefficient of missile
ω	proper frequency of missile
λ_i	degenerate-state vector
v, k	Lagrange multiplier, undetermined constant vector
t_0, t_f	initial time, final time
T	time required to reach zero-control intercepting curved surface
μ	time between reaching the zero-control intercepting curved surface and hitting the target

- $\dot{\gamma}$ angular velocity of the line-of-sight between missile and target
 $\ddot{\gamma}$ rate of change of the angular velocity of the line-of-sight
 α, β real values chosen according to need

I. Statement of the Problem

The dynamical model of the relative motion of the missile and the target is described by

$$\begin{cases}
 \dot{x}_1 = x_2 & x_1(t_0) = x_{10} \\
 \dot{x}_2 = x_3 & x_2(t_0) = x_{20} \\
 \dot{x}_3 = x_4 & x_3(t_0) = x_{30} \\
 \dot{x}_4 = -\omega^2 x_1 - 2\xi\omega x_4 + \omega^2 u & x_4(t_0) = 0
 \end{cases} \quad (1)$$

The performance index is

$$J(u) = \frac{1}{2} \int_{t_0}^{t_f} u^T \cdot u dt \quad (u^T \text{ 表示转置}) \quad (u^T \text{ indicates transposition}) \quad (2)$$

where $u \in \mathbb{R}^3$, and t_f is given beforehand. Let the target set be

$$\begin{cases}
 g_1(x_1(t_f), x_2(t_f), x_3(t_f)) = 0 \\
 g_2(x_1(t_f), \dot{x}_2(t_f), x_3(t_f)) \leq 0
 \end{cases} \quad (3)$$

The problem is to find the optimum guidance laws for the system described in (1), and guide the system from the given initial state (2) to the final state (3), keeping the performance index at its minimum value.

We will find the optimum guidance law for two different target sets in the following.

II. Minimum-Energy Guidance Laws for the Case Where the Terminal Miss-Distance is Zero

The target set is described by

$$x_1(t_f) = 0$$

The other parameters of the terminal state have no restrictions placed on them.

Based on the maximum principle [2], we write the Hamiltonian for the problem as

$$H = \frac{1}{2} u^T u + \lambda_1^T x_1 + \lambda_2^T x_2 + \lambda_3^T x_3 + \lambda_4^T (-\omega^2 x_3 - 2\xi\omega x_4 + \omega^2 u) \quad (4)$$

where $\lambda_1, \lambda_2, \lambda_3, \lambda_4$ are the degenerate-state vectors of the dynamical system (1).

The degenerate-state equations for the system are

$$\begin{cases} \lambda_1(t) = 0 \\ \lambda_2(t) = -\lambda_1(t) \\ \lambda_3(t) = -\lambda_2(t) + \omega^2 \lambda_4(t) \\ \lambda_4(t) = -\lambda_3(t) + 2\xi\omega \lambda_4(t) \end{cases} \quad (5)$$

The interception conditions of the system are given by

$$\begin{cases} \lambda_1(t_f) = v \\ \lambda_2(t_f) = 0 \\ \lambda_3(t_f) = 0 \\ \lambda_4(t_f) = 0 \end{cases} \quad (6)$$

On the basis of the minimum principle, the optimum guidance laws and the corresponding degenerate-state parameters should make the Hamiltonian function a minimum. From

$$\frac{\partial H}{\partial u} = 0$$

we obtain

$$\ddot{\lambda}_4(t) = -\omega^2 \lambda_4(t) \quad (7)$$

From Eq. (7) one can see that, in order to obtain the optimum guidance laws, one must find the state vector $\lambda_4(t)$.

From the first two equations in Eq. (5) and the corresponding boundary conditions one can obtain

$$\begin{aligned} \lambda_1(t) &= v \\ \lambda_2(t) &= v(t_f - t) \end{aligned}$$

Hence,

/73

$$\lambda_3(t) = -v(t_f - t) + \omega^2 \lambda_4(t) \quad (8)$$

Now, find the first derivative of the fourth equation of Eq. (5), and obtain

$$\ddot{\lambda}_4(t) = -\lambda_3(t) + 2\xi\omega\dot{\lambda}_4(t)$$

Substituting Eq. (8) into the above equation, one obtains

$$\ddot{\lambda}_4(t) - 2\xi\omega\dot{\lambda}_4(t) + \omega^2\lambda_4(t) = v(t_f - t) \quad (9)$$

from equation (7) we know that to find the rule of optimal control we must only determine that $\lambda_4(t)$ will work. In equation (9) let

hence equation (9) becomes

$$\ddot{\lambda}_4(\tau) + 2\xi\omega\dot{\lambda}_4(\tau) + \omega^2\lambda_4(\tau) = v\tau \quad (9')$$

then

When $\tau = 0$, $t = t_f$ and $\lambda_4(0) = 0$. Assume $\dot{\lambda}_4(0) = 0$.

Eq. (9') is a second-order ~~nonhomogeneous~~ linear differential equation with constant coefficients. Using Lagrange's transformation,

one finds its solution to be

$$\lambda_4(\tau) = \frac{v\tau}{\omega^2} - \frac{2\xi v}{\omega^2} + \frac{ve^{-t\omega\tau}}{\omega^2} \left[2\xi \cos \Omega \tau + \frac{2\xi^2 - 1}{(1 - \xi^2)^{1/2}} \sin \Omega \tau \right] \quad (10)$$

where

$$\Omega = \omega(1 - \xi^2)^{1/2}$$

Substituting Eq. (10) into Eq. (7), one obtains the optimal control law

$$\begin{aligned} \bar{u}(t) = -v \left\{ (t_f - t) - \frac{2\xi}{\omega} + \frac{1}{\omega} e^{-t\omega(t_f - t)} \left[2\xi \cos \Omega(t_f - t) \right. \right. \\ \left. \left. + \left(\frac{2\xi^2 - 1}{1 - \xi^2} \right)^{1/2} \sin \Omega(t_f - t) \right] \right\} \end{aligned} \quad (11)$$

To completely determine the optimal control law, we need to determine the constant vector v . For this purpose, we have to insert Eq. (11) into ^{system mode equation set} Eq. (1), and solve for the state parameters.

We obtain from the third equation of Eq. ^{set} (1)

$$\ddot{x}_3(t) = \dot{x}_4(t)$$

Substituting the fourth equation of Eq. ^{set} (1) into the above equation, we get

$$\ddot{x}_3(t) = -\omega^2 x_3(t) - 2\xi \omega \dot{x}_3(t) + \omega^2 \bar{u}(t)$$

Now, substitute the third equation of Eq. ^{set} (1) into the above equation, and we obtain

$$\ddot{x}_3(t) + 2\xi \omega \dot{x}_3(t) + \omega^2 x_3(t) = \omega^2 \bar{u}(t)$$

Substituting Eq. (11) into the above equation, we obtain

$$\ddot{x}_2 + 2\xi\omega x_2 + \omega^2 x_2 = -v\omega^2 \left\{ (t_f - t) - \frac{2\xi}{\omega} + \frac{1}{\omega} e^{-t_0''/\tau} \left[2\xi \cos \Omega(t_f - t) + \frac{2\xi^2 - 1}{(1 - \xi^2)^{1/2}} \sin \Omega(t_f - t) \right] \right\} \quad (12)$$

This is again a second-order uneven linear differential equation with constant coefficients that can be solved by means of the Lagrange transformation. The final results are

$$\begin{aligned} x_2(t) = & -v \left\{ (t_f - t) - \left[t_f^2 + \frac{(\xi\omega t_f + 1)^2}{\Omega^2} \right]^{1/2} e^{-t_0''/\tau} \sin(\Omega t + \psi_1) \right. \\ & - \frac{1}{4\omega(1 - \xi^2)^{1/2}} e^{-t_0''/\tau} \sin[\Omega(t_f - t) + \psi_2] \\ & - (a^2 + b^2)^{1/2} e^{-t_0''/\tau} \cos(\Omega t + \psi_3) - \frac{1}{4\omega(1 - \xi^2)^{1/2}} e^{-t_0''/\tau} \sin[\Omega(t_f - t) + \psi_4] \\ & \left. + \frac{\Omega}{4\xi\omega^2(1 - \xi^2)^{1/2}} e^{-t_0''/\tau} \cos[\Omega(t_f - t) + \psi_5] \right\} + x_{20} - \frac{1}{1 - \xi^2} e^{-t_0''/\tau} \cos(\Omega t + \psi_2) \end{aligned} \quad (13)$$

In the above equation

/74

$$\psi_1 = \operatorname{tg}^{-1} \left[\frac{2\xi(1 - \xi^2)^{1/2}}{2\xi^2 - 1} \right]$$

$$\psi_2 = \operatorname{tg}^{-1} \left[\frac{\Omega t_f}{\xi\omega t_f + 1} \right]$$

$$\psi_3 = \operatorname{tg}^{-1} \left[\frac{\xi\omega}{\Omega} \right]$$

$$\psi_4 = \operatorname{tg}^{-1} \left[\frac{1 + \xi^2}{1 - \xi^2} \operatorname{tg}(\Omega t_f + \psi_2) \right]$$

$$a = \frac{\Omega}{4\xi\omega^2(1 - \xi^2)^{1/2}} \cos(\Omega t_f + \psi_5)$$

$$b = \frac{(1 + \xi^2)\Omega}{4\xi\omega^2(1 - \xi^2)^{1/2}} \sin(\Omega t_f + \psi_5)$$

The above are all functions of the given parameters ξ and ω of the missile, and of the terminal time t_f , and are invariant for a given t_f .

Substituting Eq. (13) into the second equation of Eq. (1) and integrating, making use of the given initial condition, we obtain

$$\begin{aligned}
x_2(t) = & x_{20} + \frac{x_{30}}{\omega(1-\xi^2)} [e^{-i\omega t_0} \cos(\Omega t_0 + \psi_0 + \psi_s) - e^{-i\omega t} \cos(\Omega t + \psi_0 + \psi_s)] \\
& - \sqrt{\left(t_1 t - \frac{t^2}{2}\right) + \left[t_1^2 + \frac{(\xi \omega t_1 + 1)^2}{\Omega^2}\right]^{1/2}} \frac{e^{-i\omega t}}{\omega} \sin(\Omega t + \psi_1 + \psi_s) \\
& + \frac{(a^2 + b^2)^{1/2}}{\omega} e^{-i\omega(t_1 t_0)} \cos(\Omega t + \psi_3 + \psi_s) + \frac{e^{-i\omega(t_1 t_0)}}{4\omega^2(1-\xi^2)^{1/2}} \sin[\Omega(t_1 - t) + \psi_0 - \psi_s] \\
& - \frac{e^{-i\omega(t_1 t_0)}}{4\omega^2(1-\xi^2)^{1/2}} \sin[\Omega(t_1 - t) + \psi_0 + \psi_s] + \frac{\Omega e^{-i\omega(t_1 t_0)}}{4\xi\omega^3(1-\xi^2)^{1/2}} \cos[\Omega(t_1 - t) \\
& + \psi_0 + \psi_s] - \left(t_1 t_0 - \frac{t_0^2}{2}\right) + C_1(t_1, t_0, \xi, \omega) \}
\end{aligned} \tag{14}$$

In the above equation

$$\begin{aligned}
C_1(t_1, t_0, \xi, \omega) = & - \left[t_1^2 + \frac{(\xi \omega t_1 + 1)^2}{\Omega^2}\right]^{1/2} \frac{e^{-i\omega t_0}}{\omega} \sin(\Omega t_0 + \psi_1 + \psi_s) \\
& - \frac{(a^2 + b^2)^{1/2}}{\omega} e^{-i\omega(t_1 t_0)} \cos(\Omega t_0 + \psi_3 + \psi_s) - \frac{1}{4\omega^2(1-\xi^2)^{1/2}} \{e^{-i\omega(t_1 t_0)} \sin[\Omega(t_1 - t_0) \\
& + \psi_0 - \psi_s] - e^{-i\omega(t_1 t_0)} \sin[\Omega(t_1 - t_0) + \psi_0 + \psi_s]\} - \frac{\Omega e^{-i\omega(t_1 t_0)}}{4\xi\omega^3(1-\xi^2)^{1/2}} \cos[\Omega(t_1 - t_0) \\
& + \psi_0 + \psi_s]
\end{aligned}$$

$$\psi_s = \text{tg}^{-1} \left[\frac{\Omega}{\xi \omega} \right]$$

Substitute Eq. (14) into the first equation of Eq. (1) and integrate, making use of the corresponding initial condition. We obtain

/75

$$\begin{aligned}
x_1(t) = & x_{10} + x_{20}(t - t_0) + \frac{x_{30}}{\omega(1-\xi^2)} \left[e^{-i\omega t_0} (t - t_0) \cos(\Omega t_0 + \psi_0 + \psi_s) \right. \\
& \left. - \frac{e^{-i\omega t_0}}{\omega} \cos(\Omega t_0 + \psi_0 + 2\psi_s) + \frac{e^{-i\omega t}}{\omega} \cos(\Omega t + \psi_0 + 2\psi_s) \right] \\
& - \sqrt{\left(t_1 t - \frac{t^2}{2} - \frac{t_0^2}{6}\right) - \left[t_1^2 + \frac{(\xi \omega t_1 + 1)^2}{\Omega^2}\right]^{1/2}} \frac{e^{-i\omega t}}{\omega} \sin(\Omega t + \psi_1 + 2\psi_s) \\
& - \frac{(a^2 + b^2)^{1/2}}{\omega^2} e^{-i\omega(t_1 t_0)} \cos(\Omega t + \psi_3 + \psi_s) + \frac{e^{-i\omega(t_1 t_0)}}{4\omega^3(1-\xi^2)^{1/2}} \sin[\Omega(t_1 - t) + \psi_0 - 2\psi_s] \\
& - \frac{e^{-i\omega(t_1 t_0)}}{4\omega^3(1-\xi^2)^{1/2}} \sin[\Omega(t_1 - t) + \psi_0 + 2\psi_s] + \frac{\Omega e^{-i\omega(t_1 t_0)}}{4\xi\omega^4(1-\xi^2)^{1/2}} \cos[\Omega(t_1 - t) + \psi_0 + 2\psi_s] \\
& - \left(t_1 t_0 - \frac{t_0^2}{2}\right) t + C_1(t_1, t_0, \xi, \omega) t + \left(\frac{t_1 t_0^2}{2} - \frac{t_0^3}{3}\right) + C_2(t_1, t_0, \xi, \omega) \}
\end{aligned} \tag{15}$$

In the above equation,

$$\begin{aligned}
 C_0(t, t_0, \xi, \omega) = & -C_1(t, t_0, \xi, \omega)t_0 + \left[t_0^2 + \frac{(\xi\omega t_0 + 1)^2}{\Omega^2} \right]^{1/2} \frac{e^{-i\omega t_0}}{\omega^2} \\
 & \times \sin(\Omega t_0 + \psi_1 + 2\psi_4) + \frac{(a^2 + b^2)^{1/2}}{\omega^2} e^{-i\omega(t_0 - t_0)} \cos(\Omega t_0 + \psi_3 + \psi_4) \\
 & - \frac{e^{-i\omega(t_0 - t_0)}}{4\omega^2(1 - \xi^2)^{1/2}} \sin(\Omega(t_0 - t_0) + \psi_0 - 2\psi_4) + \frac{e^{-i\omega(t_0 - t_0)}}{4\omega^2(1 - \xi^2)^{1/2}} \sin(\Omega(t_0 - t_0) + \psi_0 + 2\psi_4) \\
 & - \frac{\Omega e^{-i\omega(t_0 - t_0)}}{4\xi\omega^2(1 - \xi^2)^{1/2}} \cos(\Omega(t_0 - t_0) + \psi_0 + 2\psi_4)
 \end{aligned}$$

The constant vector v can be determined from $x_1(t_f) = 0$.

$$\begin{aligned}
 v = & \left\{ x_{10} + x_{20}(t_f - t_0) + \frac{x_{30}}{\omega(1 - \xi^2)} \left[e^{-i\omega t_0}(t_f - t_0) \cos(\Omega t_0 + \psi_0 + \psi_4) \right. \right. \\
 & - \frac{e^{-i\omega t_0}}{\omega} \cos(\Omega t_0 + \psi_0 + 2\psi_4) + \frac{e^{-i\omega t_0}}{\omega} \cos(\Omega t_0 + \psi_0 + 2\psi_4) \left. \right\} \times \left\{ \frac{(t_f - t_0)^2}{3} \right. \\
 & - \left[t_0^2 + \frac{(\xi\omega t_0 + 1)^2}{\Omega^2} \right]^{1/2} \frac{e^{-i\omega t_0}}{\omega^2} \sin(\Omega t_0 + \psi_1 + 2\psi_4) - \frac{(a^2 + b^2)^{1/2}}{\omega^2} e^{-i\omega t_0} \cos(\Omega t_0 + \psi_3 + \psi_4) \\
 & + \frac{e^{-i\omega t_0}}{4\omega^2(1 - \xi^2)^{1/2}} \sin(\psi_0 - 2\psi_4) - \frac{1}{4\omega^2(1 - \xi^2)^{1/2}} \sin(\psi_0 + 2\psi_4) + \frac{\Omega}{4\xi\omega^2(1 - \xi^2)^{1/2}} \\
 & \left. \times \cos(\psi_0 + 2\psi_4) + C_1(t, t_0, \xi, \omega)t_f + C_0(t, t_0, \xi, \omega) \right\}^{-1}
 \end{aligned} \quad (16)$$

Substituting the value of v into Eq. (11), we obtain

$$\begin{aligned}
 \bar{u}(t) = & - \left\{ x_{10} + x_{20}(t_f - t_0) + \frac{x_{30}}{\omega(1 - \xi^2)} \left[e^{-i\omega t_0}(t_f - t_0) \cos(\Omega t_0 + \psi_0 + \psi_4) \right. \right. \\
 & - \frac{e^{-i\omega t_0}}{\omega} \cos(\Omega t_0 + \psi_0 + 2\psi_4) + \frac{e^{-i\omega t_0}}{\omega} \cos(\Omega t_0 + \psi_0 + 2\psi_4) \left. \right\} \times \left\{ (t_f - t) \right. \\
 & - \frac{2\xi}{\omega} + \frac{e^{-i\omega(t_f - t_0)}}{\omega} \left[2\xi \cos \Omega(t_f - t) + \frac{2\xi^2 - 1}{(1 - \xi^2)^{1/2}} \sin \Omega(t_f - t) \right] \left. \right\} \times \left\{ \frac{(t_f - t_0)^2}{3} \right. \\
 & - \left[t_0^2 + \frac{(\xi\omega t_0 + 1)^2}{\Omega^2} \right]^{1/2} \frac{e^{-i\omega t_0}}{\omega^2} \sin(\Omega t_0 + \psi_1 + 2\psi_4) - \frac{(a^2 + b^2)^{1/2}}{\omega^2} e^{-i\omega t_0} \cos(\Omega t_0 + \psi_3 + \psi_4) \\
 & + \frac{e^{-i\omega t_0}}{4\omega^2(1 - \xi^2)^{1/2}} \sin(\psi_0 - 2\psi_4) - \frac{1}{4\omega^2(1 - \xi^2)^{1/2}} \sin(\psi_0 + 2\psi_4) + \frac{\Omega}{4\xi\omega^2(1 - \xi^2)^{1/2}} \\
 & \left. \times \cos(\psi_0 + 2\psi_4) + C_1(t, t_0, \xi, \omega)t_f + C_0(t, t_0, \xi, \omega) \right\}^{-1}
 \end{aligned} \quad (17)$$

Let

$$\begin{aligned}
 F(t, t_0, \xi, \omega) = & - \left[t_0^2 + \frac{(\xi\omega t_0 + 1)^2}{\Omega^2} \right]^{1/2} \frac{e^{-i\omega t_0}}{\omega^2} \sin(\Omega t_0 + \psi_1 + 2\psi_4) - \frac{(a^2 + b^2)^{1/2}}{\omega^2} \\
 & \times e^{-i\omega t_0} \cos(\Omega t_0 + \psi_3 + \psi_4) + \frac{e^{-i\omega t_0}}{4\omega^2(1 - \xi^2)^{1/2}} \sin(\psi_0 - 2\psi_4) - \frac{1}{4\omega^2(1 - \xi^2)^{1/2}} \\
 & \times \sin(\psi_0 + 2\psi_4) + \frac{\Omega}{4\xi\omega^2(1 - \xi^2)^{1/2}} \cos(\psi_0 + 2\psi_4) + C_1(t, t_0, \xi, \omega)t_f \\
 & + C_0(t, t_0, \xi, \omega)
 \end{aligned}$$

/76

Under the condition that t_f is given, $F(t_f, t_0, \xi, \omega)$ is a constant quantity determined by the missile parameters ξ and ω , and the time t_0 . Thus, Eq. (17) can be simplified to

$$\begin{aligned} \bar{u}(t) = & - \left\{ x_{10} + x_{20}(t_f - t_0) + \frac{x_{30}}{\omega(1 - \xi^2)} \left[e^{-i\omega t_0}(t_f - t_0) \cos(\Omega t_0 + \psi_0 + \psi_s) \right. \right. \\ & - \frac{e^{-i\omega t}}{\omega} \cos(\Omega t_0 + \psi_0 + 2\psi_s) + \frac{e^{-i\omega t_f}}{\omega} \cos(\Omega t_f + \psi_0 + 2\psi_s) \left. \right\} \times \left\{ (t_f - t) \right. \\ & - \frac{2\xi}{\omega} + \frac{e^{-i\omega(t_f - t_0)}}{\omega} \left[2\xi \cos \Omega(t_f - t) + \frac{2\xi^2 - 1}{(1 - \xi^2)^{1/2}} \sin \Omega(t_f - t) \right] \left. \right\} \\ & \times \left\{ \frac{(t_f - t_0)^2}{3} + F(t_f, t_0, \xi, \omega) \right\}^{-1} \end{aligned} \quad (18)$$

The optimum guidance law at $t = t_0$ is

$$\begin{aligned} \bar{u}(t_0) = & - \left\{ x_{10} + x_{20}(t_f - t_0) + \frac{x_{30}}{\omega(1 - \xi^2)} \left[e^{-i\omega t_0}(t_f - t_0) \cos(\Omega t_0 + \psi_0 + \psi_s) \right. \right. \\ & - \frac{e^{-i\omega t}}{\omega} \cos(\Omega t_0 + \psi_0 + 2\psi_s) + \frac{e^{-i\omega t_f}}{\omega} \cos(\Omega t_f + \psi_0 + 2\psi_s) \left. \right\} \times \left\{ (t_f - t_0) \right. \\ & - \frac{2\xi}{\omega} + \frac{e^{-i\omega(t_f - t_0)}}{\omega} \left[2\xi \cos \Omega(t_f - t_0) + \frac{2\xi^2 - 1}{(1 - \xi^2)^{1/2}} \sin \Omega(t_f - t_0) \right] \left. \right\} \times \left\{ \frac{(t_f - t_0)^2}{3} \right. \\ & \left. + F(t_f, t_0, \xi, \omega) \right\}^{-1} \end{aligned} \quad (19)$$

Let

$$\begin{aligned} K(t_f, t_0, \xi, \omega) = & \left\{ (t_f - t_0) - \frac{2\xi}{\omega} + \frac{e^{-i\omega(t_f - t_0)}}{\omega(1 - \xi^2)} \sin[\Omega(t_f - t_0) + \psi_0] \right\} \\ & \times \left\{ \frac{(t_f - t_0)^2}{3} + F(t_f, t_0, \xi, \omega) \right\}^{-1} \\ L(t_f, t_0, \xi, \omega) = & \frac{1}{\omega(1 - \xi^2)} \left[e^{-i\omega t_0}(t_f - t_0) \cos(\Omega t_0 + \psi_0 + \psi_s) - \frac{e^{-i\omega t}}{\omega} \right. \\ & \times \cos(\Omega t_0 + \psi_0 + 2\psi_s) + \frac{e^{-i\omega t_f}}{\omega} \cos(\Omega t_f + \psi_0 + 2\psi_s) \left. \right] \times \left\{ (t_f - t_0) - \frac{2\xi}{\omega} \right. \\ & \left. + \frac{e^{-i\omega(t_f - t_0)}}{\omega(1 - \xi^2)} \sin[\Omega(t_f - t_0) + \psi_0] \right\} \times \left\{ \frac{(t_f - t_0)^2}{3} + F(t_f, t_0, \xi, \omega) \right\}^{-1} \end{aligned}$$

Eq. (19) can thus be written in the simplified form

$$\bar{u}(t_0) = -K(t_f, t_0, \xi, \omega)(x_{10} + x_{20}(t_f - t_0)) - L(t_f, t_0, \xi, \omega)x_{30} \quad (20)$$

By a proper choice of the time $t_f - t_0$, we can change the guidance law expressed by Eq. (20) into one that consists of a proportional guidance term with variable coefficients (that is, proportional to the angular velocity of the line-of-sight) and a modifying term that is related to acceleration and the angular acceleration of the line of sight. [1]

/77

When $\omega \rightarrow \infty$, the dynamic response of the missile disappears, i.e., there is neither oscillation nor delay in the response of the system. At this time, $F(t_f, t_0, \xi, \omega) = 0$.

$$K(t, t_0, \xi, \omega) = \frac{3}{(t - t_0)^2}$$

$$L(t, t_0, \xi, \omega) = 0$$

Therefore,

$$\bar{u}(t_0) = - \frac{3 [x_{10} + x_{20}(t_f - t_0)]}{(t_f - t_0)^2} \quad (21)$$

which is the optimum guidance law for the instantaneous response of the mass point. By choosing different values for $t_f - t_0$, one can obtain proportional guidance laws with different coefficients. [3]

III. Guidance Laws for the Case Where the Final State is a Zero-Control Intercepting Curved Surface

When the dynamic system (1) is guided towards the zero-control intercepting curved surface L , its target set is represented by [1, 2]:

$$\begin{cases} x_1(T) + \mu x_2(T) = 0, \mu \geq 0 \\ x_3(T) = 0 \end{cases} \quad (22)$$

Assume that the time T of entry into the zero-control intercepting curved surface L has already been chosen, while the time interval μ between the time of entry into the zero-control

intercepting curved surface and that of hitting the target is to be determined.

$x_3(T) = 0$ is necessary to keep the system within the curved surface L after it has been guided into it.

The performance index is still given by Eq. (2), and the Hamiltonian function H of the system remains the same. Hence, the dynamic system (1) has the same set of degenerate-state equations as described by Eq. (5), but the interception conditions are changed to

$$\begin{cases} \lambda_1(T) = v \\ \lambda_2(T) = v\mu \\ \lambda_3(T) = k \\ \lambda_4(T) = 0 \end{cases} \quad (23)$$

In the above, v and k are Lagrange multipliers, and are undetermined constant vectors. Solving Eq. (5) under these boundary conditions, we obtain

$$\begin{aligned} \lambda_1(t) &= v \\ \lambda_2(t) &= v(T + \mu - t) \\ \dot{\lambda}_3(t) &= -v(T + \mu - t) + \omega^2 \lambda_4(t) \\ \ddot{\lambda}_4(t) &= 2\xi\omega \dot{\lambda}_4(t) - \omega^2 \lambda_4(t) + v(T + \mu - t) \end{aligned}$$

On the basis of the results obtained in Section II, we have

$$\begin{aligned} \lambda_4(t) = \frac{v}{\omega^2} \left\{ (T + \mu - t) - \frac{2\xi}{\omega} + \frac{1}{\omega} e^{-\xi\omega(T+\mu-t)} \left[2\xi \cos \Omega(T + \mu - t) \right. \right. \\ \left. \left. + \frac{2\xi^2 - 1}{(1 - \xi^2)^{1/2}} \sin \Omega(T + \mu - t) \right] \right\} \end{aligned} \quad (24)$$

Substituting $\lambda_4(t)$ into Eq. (7), we obtain the optimum guidance law

$$\begin{aligned} \ddot{u}(t) = -v \left\{ (T + \mu - t) - \frac{2\xi}{\omega} + \frac{1}{\omega} e^{-\xi\omega(T+\mu-t)} \left[2\xi \cos \Omega(T + \mu - t) \right. \right. \\ \left. \left. + \frac{2\xi^2 - 1}{(1 - \xi^2)^{1/2}} \sin \Omega(T + \mu - t) \right] \right\} \end{aligned} \quad (25)$$

Substituting Eq. (25) into Eq. (1), we can solve for $x_3(t)$, $x_2(t)$ and $x_1(t)$ by the same procedure used in Section II. /78

$$\begin{aligned}
 x_3(t) = & -v \left\{ (T + \mu - t) - \left[(T + \mu)^2 + \frac{(\xi \omega (T + \mu) + 1)^2}{\Omega^2} \right]^{1/2} e^{-i\omega t} \sin(\Omega t + \psi_1) \right. \\
 & - \frac{e^{-i\omega(T+\mu-t)}}{4\omega(1-\xi^2)^{1/2}} \sin[\Omega(T + \mu - t) + \psi_0] - (a^2 + b^2)^{1/2} e^{-i\omega(T+\mu-t)} \\
 & \times \cos(\Omega t + \psi_3) - \frac{e^{-i\omega(T+\mu-t)}}{4\omega(1-\xi^2)^{1/2}} \sin[\Omega(T + \mu - t) + \psi_0] \\
 & \left. + \frac{\Omega e^{-i\omega(T+\mu-t)}}{4\xi\omega^2(1-\xi^2)^{1/2}} \cos[\Omega(T + \mu - t) + \psi_0] \right\} + \frac{x_{30}}{1-\xi^2} e^{-i\omega t} \cos(\Omega t + \psi_2) \quad (26)
 \end{aligned}$$

$$\begin{aligned}
 x_2(t) = & x_{20} + \frac{x_{30}}{\omega(1-\xi^2)} \left\{ e^{-i\omega t_0} \cos(\Omega t_0 + \psi_0 + \psi_4) - e^{-i\omega t} \cos(\Omega t + \psi_0 + \psi_4) \right. \\
 & - v \left\{ \left[(T + \mu) t - \frac{t^2}{2} \right] + \left[(T + \mu)^2 + \frac{(\xi \omega (T + \mu) + 1)^2}{\Omega^2} \right]^{1/2} \frac{e^{-i\omega t}}{\omega} \sin(\Omega t + \psi_1 + \psi_4) \right. \\
 & + \frac{(a^2 + b^2)^{1/2}}{\omega} e^{-i\omega(T+\mu-t)} \cos(\Omega t + \psi_3 + \psi_4) + \frac{e^{-i\omega(T+\mu-t)}}{4\omega^2(1-\xi^2)^{1/2}} \\
 & \times \sin[\Omega(T + \mu - t) + \psi_0 - \psi_4] - \frac{e^{-i\omega(T+\mu-t)}}{4\omega^2(1-\xi^2)^{1/2}} \sin[\Omega(T + \mu - t) + \psi_0 + \psi_4] \\
 & + \frac{\Omega e^{-i\omega(T+\mu-t)}}{4\xi\omega^3(1-\xi^2)^{1/2}} \cos[\Omega(T + \mu - t) + \psi_0 + \psi_4] - \left[(T + \mu)t_0 - \frac{t_0^2}{2} \right] \\
 & \left. \left. + C_1(T + \mu, t_0, \xi, \omega) \right\} \right\} \quad (27)
 \end{aligned}$$

$$\begin{aligned}
 x_1(t) = & x_{10} + x_{20}(t - t_0) + \frac{x_{30}}{\omega(1-\xi^2)} \left\{ e^{-i\omega t_0}(t - t_0) \cos(\Omega t_0 + \psi_0 + \psi_4) \right. \\
 & - \frac{e^{-i\omega t_0}}{\omega} \cos(\Omega t_0 + \psi_0 + 2\psi_4) + \frac{e^{-i\omega t}}{\omega} \cos(\Omega t + \psi_0 + 2\psi_4) \left. \right\} \\
 & - v \left\{ \left[(T + \mu) \frac{t^2}{2} - \frac{t^3}{6} \right] - \left[(T + \mu)^2 + \frac{(\xi \omega (T + \mu) + 1)^2}{\Omega^2} \right]^{1/2} \frac{e^{-i\omega t}}{\omega^2} \sin(\Omega t + \psi_1 + 2\psi_4) \right. \\
 & - \frac{(a^2 + b^2)^{1/2}}{\omega^2} e^{-i\omega(T+\mu-t)} \cos(\Omega t + \psi_3 + \psi_4) + \frac{e^{-i\omega(T+\mu-t)}}{4\omega^3(1-\xi^2)^{1/2}} \\
 & \times \sin[\Omega(T + \mu - t) + \psi_0 - 2\psi_4] - \frac{e^{-i\omega(T+\mu-t)}}{4\omega^3(1-\xi^2)^{1/2}} \sin[\Omega(T + \mu - t) + \psi_0 + 2\psi_4] \\
 & + \frac{\Omega e^{-i\omega(T+\mu-t)}}{4\xi\omega^4(1-\xi^2)^{1/2}} \cos[\Omega(T + \mu - t) + \psi_0 + 2\psi_4] - \left[(T + \mu)t_0 - \frac{t_0^2}{2} \right] t \\
 & \left. + C_1(T + \mu, t_0, \xi, \omega) t + \frac{(T + \mu)t_0^2}{2} - \frac{t_0^3}{3} + C_0(T + \mu, t_0, \xi, \omega) \right\} \quad (28)
 \end{aligned}$$

Letting $t = T$ in Eq. (28), we obtain

$$x_1(T) = x_1^0(T) - v \left\{ \frac{(T-t_0)^2}{3} + \frac{\mu(T-t_0)^2}{2} + \Delta x_1(T, \mu, \xi, \omega) \right\} \quad (29)$$

where

$$x_1^0(T) = x_{10} + x_{10}(T-t_0) + \frac{x_{30}}{\omega(1-\xi^2)} \left[e^{-i\omega t_0}(T-t_0)\cos(\Omega t_0 + \psi_0 + \psi_s) - \frac{e^{-i\omega T}}{\omega} \cos(\Omega t_0 + \psi_0 + 2\psi_s) + \frac{e^{-i\omega T}}{\omega} \cos(\Omega T - \psi_0 + 2\psi_s) \right]$$

$$\begin{aligned} \Delta X_1(T, \mu, \xi, \omega) = & - \left[(T+\mu)^2 + \frac{(\xi\omega(T+\mu)+1)^2}{\Omega^2} \right]^{1/2} \frac{e^{-i\omega T}}{\omega^2} \sin(\Omega T + \psi_1 + 2\psi_s) \\ & - \frac{(a^2+b^2)^{1/2}}{\omega^2} e^{-i\omega(2T+\mu)} \cos(\Omega T + \psi_s + \psi_s) + \frac{e^{-i\omega(2T+\mu)}}{4\omega^2(1-\xi^2)^{1/2}} \\ & \times \sin(\Omega\mu + \psi_0 - 2\psi_s) - \frac{e^{-i\omega\mu}}{4\omega^2(1-\xi^2)^{1/2}} \sin(\Omega\mu + \psi_0 + 2\psi_s) \\ & + \frac{\Omega e^{-i\omega\mu}}{4\xi\omega^2(1-\xi^2)^{1/2}} \cos(\Omega\mu + \psi_0 + 2\psi_s) + C_1(T+\mu, t_0, \xi, \omega) T \\ & + C_2(T+\mu, t_0, \xi, \omega) \end{aligned} \quad /79$$

Letting $t = T$ in Eq. (27), we obtain

$$x_2(T) = x_2^0(T) - v \left\{ \frac{(T-t_0)^2}{2} + \mu(T-t_0) + \Delta X_2(T, \mu, \xi, \omega) \right\} \quad (30)$$

where

$$\begin{aligned} x_2^0(T) = & x_{20} + \frac{x_{30}}{\omega(1-\xi^2)} [e^{-i\omega t_0}\cos(\Omega t_0 + \psi_0 + \psi_s) - e^{-i\omega T}\cos(\Omega T + \psi_0 + \psi_s)] \\ \Delta X_2(T, \mu, \xi, \omega) = & \left[(T+\mu)^2 + \frac{(\xi\omega(T+\mu)+1)^2}{\Omega^2} \right]^{1/2} \frac{e^{-i\omega T}}{\omega} \sin(\Omega T + \psi_1 + \psi_s) \\ & + \frac{(a^2+b^2)^{1/2}}{\omega} e^{-i\omega(2T+\mu)} \cos(\Omega T + \psi_s + \psi_s) + \frac{e^{-i\omega(2T+\mu)}}{4\omega^2(1-\xi^2)^{1/2}} \\ & \times \sin(\Omega\mu + \psi_0 - \psi_s) - \frac{e^{-i\omega\mu}}{4\omega^2(1-\xi^2)^{1/2}} \sin(\Omega\mu + \psi_0 + \psi_s) \\ & + \frac{\Omega e^{-i\omega\mu}}{4\xi\omega^2(1-\xi^2)^{1/2}} \cos(\Omega\mu + \psi_0 + \psi_s) + C_1(T+\mu, t_0, \xi, \omega) \end{aligned}$$

As the system should reach the target set at $t = T$, the following relation should be satisfied:

$$x_1(T) + \mu x_2(T) = 0$$

From Eqs. (29) and (30), we obtain

$$x_1^0(T) + \mu x_2^0(T) - v \left\{ \frac{(T-t_0)^3}{3} + \mu(T-t_0) + \mu^2(T-t_0) + \Delta X_1(T, \mu, \xi, \omega) + \mu \Delta X_2(T, \mu, \xi, \omega) \right\} = 0$$

from which we can solve for v .

$$v = \frac{x_1^0(T) + \mu x_2^0(T)}{\frac{(T-t_0)^3}{3} + \mu(T-t_0) + \mu^2(T-t_0) + \Delta X_1(T, \mu, \xi, \omega) + \mu \Delta X_2(T, \mu, \xi, \omega)} \quad (31)$$

Substituting Eq. (31) into Eq. (25), we obtain the optimum guidance law

$$\begin{aligned} \ddot{u}(t) = & -(x_1^0(T) + \mu x_2^0(T)) \cdot \left\{ (T + \mu - t) - \frac{2\xi}{\omega} + \frac{1}{\omega} e^{-\omega(T-t_0)} \right. \\ & \times \left[2\xi \cos \Omega(T + \mu - t) + \frac{2\xi^2 - 1}{(1 - \xi^2)^{1/2}} \sin \Omega(T + \mu - t) \right] \left. \right\} \cdot \left\{ \frac{(T-t_0)^3}{3} \right. \\ & \left. + \mu(T-t_0) + \mu^2(T-t_0) + \Delta X_1(T, \mu, \xi, \omega) + \mu \Delta X_2(T, \mu, \xi, \omega) \right\}^{-1} \end{aligned} \quad (32)$$

The optimum guidance law at $t = t_0$ is given by

$$\begin{aligned} \ddot{u}(t_0) = & -(x_1^0(T) + \mu x_2^0(T)) \left\{ (T + \mu - t_0) - \frac{2\xi}{\omega} + \frac{1}{\omega(1 - \xi^2)^{1/2}} e^{-\omega(T-t_0)} \right. \\ & \times \sin[\Omega(T + \mu - t_0) + \psi_0] \left. \right\} \cdot \left\{ \frac{(T-t_0)^3}{3} + \mu(T-t_0) + \mu^2(T-t_0) \right. \\ & \left. + \Delta X_1(T, \mu, \xi, \omega) + \mu \Delta X_2(T, \mu, \xi, \omega) \right\}^{-1} \end{aligned} \quad (33)$$

The above equation can be written as

$$\ddot{u}(t_0) = -K_L(T, \mu, \xi, \omega)(x_{10} + x_{11}(T + \mu - t_0)) - L_L(T, \mu, \xi, \omega)x_{10} \quad (34)$$

where

$$\begin{aligned}
K_L(T, \mu, \xi, \omega) = & \left\{ (T + \mu - t_0) - \frac{2\xi}{\omega} + \frac{1}{\omega(1-\xi^2)} e^{-i\omega(T+\mu-t_0)} \right. \\
& \times \sin[\Omega(T + \mu - t_0) + \psi_0] \Big\} \left\{ \frac{(T-t_0)^3}{3} + \mu(T-t_0)^2 + \mu^2(T-t_0) \right. \\
& \left. \left. + \Delta X_1(T, \mu, \xi, \omega) + \mu \Delta X_2(T, \mu, \xi, \omega) \right\}^{-1} \\
L_L(T, \mu, \xi, \omega) = & \frac{1}{\omega(1-\xi^2)} \left\{ e^{-i\omega t_0} (T + \mu - t_0) \cos(\Omega t_0 + \psi_0 + \psi_s) \right. \\
& - \frac{1}{\omega} e^{-i\omega t_0} \cos(\Omega t_0 + \psi_0 + 2\psi_s) + \frac{1}{\omega} e^{-i\omega T} \cos(\Omega T + \psi_0 + 2\psi_s) \\
& - \mu e^{-i\omega T} \cos(\Omega T + \psi_0 + \psi_s) \Big\} \left\{ \frac{(T-t_0)^3}{3} + \mu(T-t_0)^2 + \mu^2(T-t_0) \right. \\
& \left. \left. + \Delta X_1(T, \mu, \xi, \omega) + \mu \Delta X_2(T, \mu, \xi, \omega) \right\}^{-1}
\end{aligned}$$

The t_f in ψ_1 , ψ_3 , a and b in all the equations of this section should be replaced with $T + \mu$.

In the optimum guidance law given by Eq. (33) or Eq. (34), μ is still not determined. Only when μ is determined can one say that the guidance law has been completely determined. For this purpose, we make use of the condition $x_3(T) = 0$. Although we have taken $x_3(T) = 0$ into consideration while setting up the boundary conditions for the state equations, it has not really been used in the process of establishing the optimum guidance law as the latter is independent of λ_3 . To make sure that the system will stay within the zero-control intercepting curved surface after it enters this curved surface, we must choose μ such that $x_3(T) = 0$. Letting $t = T$ in Eq. (26), we obtain

$$\begin{aligned}
x_3(T) = & -v \left\{ \mu - \left[(T + \mu)^2 + \frac{(\xi\omega(T + \mu) + 1)^2}{\Omega^2} \right]^{1/2} e^{-i\omega T} \sin(\Omega T + \psi_s) \right. \\
& - \frac{e^{-i\omega(2T+\mu)}}{4\omega(1-\xi^2)} \left[\sin(\Omega\mu + \psi_0) - (a^2 + b^2)^{1/2} e^{-i\omega(2T+\mu)} \right. \\
& \times \cos(\Omega T + \psi_s) - \frac{e^{-i\omega\mu}}{4\omega(1-\xi^2)} \left[\sin(\Omega\mu + \psi_0) + \frac{\Omega e^{-i\omega\mu}}{4\xi\omega^2(1-\xi^2)} \right. \\
& \left. \left. \times \cos(\Omega\mu + \psi_s) \right] + \frac{x_{10}}{1-\xi^2} e^{-i\omega T} \cos(\Omega T + \psi_s) \right\} = 0
\end{aligned}$$

Substituting Eq. (31) into the above equation, we obtain

$$\begin{aligned}
& - (x_1^0(T) + \mu x_2^0(T)) \left\{ \mu - \left[(T + \mu)^2 + \frac{(\xi \omega (T + \mu) - 1)^2}{\Omega^2} \right]^{-1/2} e^{-i \omega T} \sin(\Omega T + \psi_1) \right. \\
& - \frac{e^{-i \omega T}}{4 \omega (1 - \xi^2)^{1/2}} \sin(\Omega \mu + \psi_1) - (a^2 + b^2)^{-1/2} e^{-i \omega T} \cos(\Omega T + \psi_2) \\
& - \frac{e^{-i \omega T}}{4 \omega (1 - \xi^2)^{1/2}} \sin(\Omega \mu + \psi_2) + \frac{\Omega e^{-i \omega T}}{4 \xi \omega^2 (1 - \xi^2)^{1/2}} \cos(\Omega \mu + \psi_2) \Big\} \\
& \times \left\{ \frac{(T - t_0)^3}{3} + \mu (T - t_0)^2 + \mu^2 (T - t_0) + \Delta X_1(T, \mu, \xi, \omega) \right. \\
& \left. + \mu \Delta X_2(T, \mu, \xi, \omega) \right\}^{-1} + \frac{x_{10}}{1 - \xi^2} e^{-i \omega T} \cos(\Omega T + \psi_1) = 0
\end{aligned} \tag{35}$$

This is a high-order transcendental equation which can be solved for μ by means of numerical methods. It is possible to have several values of μ that satisfy Eq. (35). In this case, the smallest positive value of μ should be chosen. Of course, it is also possible that no value of μ exists that satisfies Eq. (35). This corresponds to the case where the system has been guided to the zero-control intercepting curved surface but cannot be kept within that curved surface. Here, guidance toward the zero-control intercepting curved surface becomes meaningless. From a physical standpoint, however, the equation should have a solution because the control that causes the relative acceleration to be zero does exist.

When $\omega \rightarrow \infty$, the missile loses its second-order characteristics, and becomes a mass point that responds instantaneously. At this time, $K_L(T, \mu, \xi, \omega)$ and $L_L(T, \mu, \xi, \omega)$ of Eq. (34) become

$$K_L(T, \mu, \xi, \omega) = \frac{(T - t_0)^2}{3} + \mu (T - t_0)^2 + \mu^2 (T - t_0)$$

$$L_L(T, \mu, \xi, \omega) = 0$$

The optimum guidance law $\bar{u}(t_0)$ becomes

$$\bar{u}(t_0) = - \frac{x_{10} + x_{20}(T + \mu - t_0)}{\frac{(T - t_0)^2}{3} + \mu (T - t_0)^2 + \mu^2 (T - t_0)} (T + \mu - t_0) \tag{36}$$

This is the very result obtained for guiding an instantaneously responding mass point toward the zero-control intercepting curved surface L. [8]

IV. Conclusion

We have obtained above the optimum guidance laws Eq. (20) and Eq. (34) for two kinds of target sets for missiles with second-order characteristics. These two equations are similar in form. If we express the acceleration of the missile in terms of the rotational angular velocity and the rate of change of the angular velocity of the line of sight, and let

$$T - t_0 = - \frac{x_{1c}^T (\alpha x_{10} + \beta x_{20})}{x_{2c}^T (\alpha x_{1c} + \beta x_{2c})}$$

$$T + \mu - t_0 = - \frac{x_{10}^T (\alpha x_{1c} + \beta x_{2c})}{x_{20}^T (\alpha x_{10} + \beta x_{20})}$$

then both Eq. (20) and (34) can be written as [1]

/82

$$\begin{aligned} & \bar{u}(x_{10}, x_{20}, \bar{\omega}_0, \dot{\bar{\omega}}_0, \alpha, \beta, \xi, \omega, \mu) \\ &= -L_L(x_{10}, x_{20}, \alpha, \beta, \xi, \omega, \mu) \frac{x_{10}^2}{x_{10}^T (\alpha x_{10} + \beta x_{20})} \\ & \times \left[\frac{x_{20}^T (\alpha x_{10} + \beta x_{20})}{x_{10}^2} x_{10} + \dot{\bar{\omega}}_0 \times (\alpha x_{10} + \beta x_{20}) \right] + \left[K_L(x_{10}, x_{20}, \alpha, \beta, \xi, \omega, \mu) \right. \\ & \times \frac{x_{10}^2}{x_{2c}^T (\alpha x_{1c} + \beta x_{2c})} - 2L_L(x_{10}, x_{20}, \alpha, \beta, \xi, \omega, \mu) \\ & \left. \times \frac{x_{1c}^T x_{20}}{x_{1c}^T (\alpha x_{10} + \beta x_{20})} \right] \bar{\omega}_0 \times (\alpha x_{10} + \beta x_{20}) \end{aligned} \quad (37)$$

In the above equation, $\bar{\omega}$ and $\dot{\bar{\omega}}$ are the angular velocity and the angular acceleration of the line of sight, respectively; α and β are real numbers that can be chosen according to need.

It can be seen from Eq. (37) that, under the condition of a specified transit time, the optimum guidance law for a missile with second-order characteristics is made up of a proportional

guidance with variable coefficients and a modifying term that is related to the angular acceleration of the line of sight and the acceleration. Although it is fairly complicated to compute for the coefficients of this equation, these coefficients are known functions of x_{10} , x_{20} , α , β , ξ , ω , and μ . Therefore, armed with the advanced electronic technologies of today, one should be able to attack the problem without much difficulty. As the mathematical model chosen for the missile in this paper is one step beyond that given in the listed references, the resulting guidance laws certainly possess higher accuracies.

REFERENCES

1. Wang Ch'ao-chu, Optimum Intercept Guidance Laws, Hang K'ung Hsueh Pao, No. 4, 1979.
2. Academia Sinica Systems Department, Extreme-Values Control and Principle of Maximum Value, K'e Hsueh Publishing House, 1980.11.
3. Han Ching-ch'ing et al., Guidance Laws in the Problem of Interception, Kuo Fang Kung Yeh Publishing House, 1977.6.
4. R. G. Cottrell, "Optimal intercept guidance for short-range tactical missiles," AIAA J 9:7 (1971).
5. Garber, V. "Optimum intercept laws of acceleratory target," AIAA J Vol. 6 No. 11 (1968).

Chen Hsueh-yu

(Kueichou Electro-Mechanical Design Research Institute)

ABSTRACT

An optimal guidance law which considers dynamic factors of missile and target via first order inertial loop in three dimensional space is studied on the basis of the theory of differential games. An optimal feedback guidance law is given in vector form, and the control rigidity parameter "k" is introduced into the feedback gain. The "k" is a scalar with determinate physical meaning. It represents the response characteristics and controllability of the system. Hence, in addition to being a function of time the feedback gain is related with the characteristics of the system.

Finally, several problems are discussed in brief: first, the degeneration of the optimal guidance law proposed is discussed under certain conditions; then, for the convenience of realization, a suboptimal guidance law is given in finite rigidity case by means of further simplification; and also the controllability of the system is illustrated. In addition, the case of $\xi \neq 1$ is considered in Appendix.

With the progress in numerical techniques, the extensive use of microcomputers and microprocessors has provided favorable conditions for the utilization of numerical simulation techniques for the purpose of increasing the efficiency of tactical missiles in battles. Hence, with respect to the guidance system, it is desirable to obtain a better description

Received in December 1981.

of the system by taking into consideration some factors that affect guidance accuracy, and to achieve real-time control by synthesizing more effective guidance rules. In other words, the study of tactical missile guidance laws using modern control theories is of great significance.

To go one step further in the study of guidance laws so as to be able to more effectively intercept the targets, it is not sufficient just to consider kinetic factors, but one must also take into consideration the dynamical factors of the missiles and the targets. The simplest case is where these factors are considered simply as a first-order inertial loop, i.e., there is a time lag τ between the input of control and the output of payload. Two cases are usually considered with respect to the dynamics of the target, the first being that the target moves at constant acceleration and the payload is a constant. The second case involves an indeterminate situation where the motion of the target is different from moment to moment. In some cases of this type, the guidance law can be synthesized using the theory of differential games. [1, 2, 3]

The theory of differential games is one on the study of missile and target control via the principle of extreme values. The problem of interception involves the control of both the missile and the target. These have a common performance index, but each places a different requirement on this index. Effective interception requires that the missile control have a minimum index, while escape capability dictates a maximum index for target control. The problem at hand is to consider a problem of interception in the three-dimensional space on the basis of the theory of differential games, to assume the dynamical factors of the missile and the target as a first-order inertial loop, and then to synthesize the optimum guidance law for the missile. [3]

I. The Problem

Consider the following vectorial equations of motion for the missile and the target:

$$\begin{cases} \dot{r}_d(t) = v_d(t), \\ \dot{v}_d(t) = a_d(t), \\ a_d(t) = \frac{1}{\tau_1} u_d(t) - \frac{1}{\tau_1} a_d(t), \end{cases} \quad \begin{cases} \dot{r}_m(t) = v_m(t) \\ \dot{v}_m(t) = a_m(t) \\ a_m(t) = \frac{1}{\tau_2} u_m(t) - \frac{1}{\tau_2} a_m(t) \end{cases} \quad (1)$$

In the above equation, v , r and a denote the velocity, position and acceleration vectors, respectively, of the missile or the target. u is a control strategy, and is also a vector. The subscripts d and m denote missile and target, respectively. The geometrical relations among the vectors are as shown in Figure 1. /85

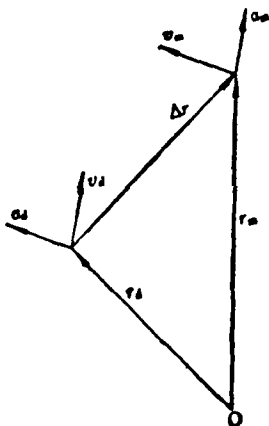


Figure 1. Geometry for intercept.

Based on Eq. (1) we can write the state equation for the intercept system as

$$\dot{x}_d(t) = F_d x_d(t) + G_d u_d(t), \quad \dot{x}_m(t) = F_m x_m(t) + G_m u_m(t) \quad (2)$$

In the above equation,

$$x'_d(t) = \{r_d(t), v_d(t), a_d(t)\}, \quad x'_m(t) = \{r_m(t), v_m(t), a_m(t)\};$$

"'" denotes transposition. $x_d(t)$ and $x_m(t)$ are 9-dimensional, so that the coefficient matrices are of order 9×9 , written simply as

$$F_d = \begin{bmatrix} 0 & 1 & 0 \\ 0 & 0 & 1 \\ 0 & 0 & -1/\tau_1 \end{bmatrix}, \quad F_m = \begin{bmatrix} 0 & 1 & 0 \\ 0 & 0 & 1 \\ 0 & 0 & -1/\tau_2 \end{bmatrix},$$

$$G_d' = [0 \ 0 \ 1/\tau_1]_{3 \times 9}, \quad G_m = [0 \ 0 \ 1/\tau_2]_{3 \times 9}$$

In the above equations, when not otherwise stated, 0 and 1 denote, respectively, a 3×3 "zero" matrix and a unit matrix, and τ_1 and τ_2 are, respectively, the delay time of the missile and that of the target. We can write $\tau_2 = \xi \tau_1$. In general, $\xi \geq 1$. Here, we take $\xi = 1$ and $\tau_2 = \tau_1 = \tau$. The case for $\xi \neq 1$ will be discussed elsewhere. In fact, the worst condition that one can have in interception is the instantaneous control of the target, which has a larger inertia, i.e., $\xi > 1$. Hence, by taking $\xi = 1$, we have placed a stricter condition on interception, which is appropriate [Appendix III]. Furthermore, we do not take into consideration restrictions of u_d and u_m , and take the performance index to be a general function of second degree [1]:

$$J = \frac{b}{2} ((r_d - r_m) \cdot (r_d - r_m)) \Big|_{t_f} + \frac{1}{2} \int_{t_0}^{t_f} [c_d^1(u_d \cdot u_d) - c_m^1(u_m \cdot u_m)] dt \quad (3)$$

In the above, b is the weighting factor of the terminal state, while t_f may be either given or not.

To obtain control of the feedback type, let $u_d(t)$ and $u_m(t)$ satisfy

$$J = \min_{u_d} \max_{u_m} \quad (4)$$

Our main purpose here is to find a control strategy $u_d(t)$ of the missile such that the miss-distance at the terminal time t_f is a minimum. Obviously, the problem described by Eqs. (2), (3) and (4) is one of extreme-value control of the linear index of second degree. We apply the method given in Ref. [1] to this problem.

First, we define a set of vectors in terms of the relative state variables:

$$\tilde{x}_d(t) \triangleq \phi_d(t_f, t)x_d(t), \quad \tilde{x}_m(t) \triangleq \phi_m(t_f, t)x_m(t) \quad (5)$$

In the above, $\phi_d(t_f, t)$ and $\phi_m(t_f, t)$ are, respectively, the basis matrix of F_d and F_m , from which we define another vector:

$$Z(t) \triangleq A(\tilde{x}_d(t) - \tilde{x}_m(t)) = A(\phi_d(t_f, t)x_d(t) - \phi_m(t_f, t)x_m(t)) \quad (6)$$

In the above equation, $A = \sqrt{B}$. Hence, Eq. (5) can be written as

$$J = \frac{1}{2} \|Z(t_f)\|_{S_f}^2 + \frac{1}{2} \int_{t_0}^{t_f} \left[\|u_d\|_{c_d^{-1}}^2 - \|u_m\|_{c_m^{-1}}^2 \right] dt \quad (7)$$

Differentiation of Eq. (6) yields

$$\dot{Z}(t) = B_d(t)u_d(t) - B_m(t)u_m(t) \quad (8)$$

In the above, $B_d(t) = A\phi_d(t_f, t)G_d$; $B_m(t) = A\phi_m(t_f, t)G_m$. The terminal condition is

$$S_f = \begin{bmatrix} 1 & 0 & 0 \\ 0 & 0 & 0 \\ 0 & 0 & 0 \end{bmatrix} \quad (9)$$

$$Z(t_f) = A(\tilde{x}_d(t_f) - \tilde{x}_m(t_f)) = A(\Delta x), \text{ for } (\Delta x)' = [\Delta r, \Delta v, \Delta a]$$

From Eq. (9), we can verify that the terminal requirement on the performance index is

$$\frac{1}{2} \|Z(t_f)\|_{S_f}^2 = \frac{A^2}{2} (\Delta r \cdot \Delta r)_f = \frac{b}{2} \|\Delta r\|_f^2 \quad (10)$$

Now we can construct the Hamiltonian of the problem on the basis of Eqs. (7) and (8):

$$\begin{aligned} H(Z, u_d, u_m, \lambda, t) &= L + \lambda'(\dot{Z}(t)) \\ &= \frac{1}{2} \|u_d\|_{c_d^{-1}}^2 - \frac{1}{2} \|u_m\|_{c_m^{-1}}^2 + \lambda'(B_d(t)u_d(t) - B_m(t)u_m(t)) \end{aligned} \quad (11)$$

The solution of the problem should satisfy the following necessary condition:

$$H(Z, \lambda, t) = \min_{u_d} \max_{u_m} H \quad (12)$$

or satisfy the accompanying equation

$$\dot{\lambda}' = -H_{\lambda} = 0 \quad (13)$$

Hence, λ = a constant vector, and

$$\lambda(t_f) = \frac{\partial(1/2 \|Z_f\|_{S_f}^2)}{\partial Z_f} = S_f Z(t_f) = A \begin{bmatrix} \Delta r \\ 0 \\ 0 \end{bmatrix}_{t=t_f}$$

$$H_{u_d} = 0, H_{u_m} = 0$$

The problem now becomes one of solving the boundary value problem of two points as described by Eqs. (8), (9) and (13). From the above conditions, we obtain

$$u_d^0(t) = -c_d B_d'(t) \lambda(t), \quad u_m^0(t) = -c_m B_m'(t) \lambda(t) \quad (14)$$

which is the optimal solution of the problem. From Eqs. (2) and (8), 14 becomes

$$G_d = G_m = G, \quad F_d = F_m = F, \quad B_d(t) = B_m(t) = B(t),$$

$$\phi_d(t_f, t) = \phi_m(t_f, t) = \phi(t_f, t) \quad /87$$

Hence, we write Eq. (14) as

$$u_d^0(t) = -c_d B'(t) \lambda(t), \quad u_m^0(t) = -c_m B'(t) \lambda(t) \quad (15)$$

From this we know that to obtain the optimal feedback guidance law we must first find $\lambda(t)$. Assume that

$$\lambda(t) = S(t) Z(t) \quad (16)$$

and substitute Eq. (15) into Eq. (8), taking Eq. (13) into consideration. We obtain

$$\dot{Z}(t) = -(c_s - c_m) B(t) B'(t) \lambda(t) \quad (16a)$$

Integration gives

$$\begin{aligned} Z(t) &= Z(t_f) - (c_s - c_m) \left[\int_{t_f}^t B(t) B'(t) S_f dt \right] Z(t_f) \\ &= [I + (c_s - c_m) B] Z(t_f) = P Z(t_f) \end{aligned} \quad (16b)$$

where

$$B = \int_{t_f}^{t_f} B(t) B'(t) S_f dt \quad (17)$$

$$(17a)$$

$$P = [I + (c_s - c_m) B]_{9 \times 9} \quad I \text{ is a } 9 \times 9 \text{ unit matrix}$$

From Eqs. (13), (16) and (17) it is not difficult to obtain

$$S(t) = S(t_f) P^{-1} \quad (18)$$

Now, we calculate $B(t)$, B and $\phi(t_f, t)$ separately, and find P . As long as P is not singular, the problem will have a solution. The basis matrix $\phi(t_f, t)$ can be expressed as [Appendix I]

$$\phi(t_f, t) = \exp \left[\int_{t_f}^{t_f} F dt \right] = e^{FT} \quad (19)$$

In this equation, $T = t_f - t$. Expand e^{FT} as $1 + FT + \frac{1}{2!} F^2 T^2 + \dots$, and define two simple functions

$$k \triangleq \frac{t_f - t}{\tau} = \frac{T}{\tau}, \quad E \triangleq 1 - e^{-k} \quad (19a)$$

Making use of the parameters k and E , Eq. (19) can be written, after some rearrangement and combination, as

$$\phi(t_f, t) = \begin{bmatrix} 1 & T & \tau^2(k - E) \\ 0 & 1 & \tau E \\ 0 & 0 & (1 - E) \end{bmatrix}_{9 \times 9} \quad (20)$$

The parameter "k" introduced here is the stiffness of the control system. In the discussions given below in Section III, we will talk about it in detail. It can be seen from Eq. (20) that the structure of the system is reflected by the basis matrix which is related not only to the time, but also to the control stiffness and inertia of the system. We will use the basis matrix to compute B and P below. Substituting Eq. (20) into Eq. (8) yields

$$B(t) = A \begin{bmatrix} 1 & T & \tau^2(k-E) \\ 0 & 1 & \tau E \\ 0 & 0 & (1-E) \end{bmatrix}_{3 \times 3} \begin{bmatrix} 0 \\ 0 \\ 1/\tau \end{bmatrix}_{3 \times 1} = A \begin{bmatrix} \tau(k-E) \\ E \\ 1/\tau(1-E) \end{bmatrix}_{3 \times 1} \quad (21)$$

Then, we can obtain the integral B [Appendix II]:

$$B = \int_0^t B(t)B'(t)S_d dt = \begin{bmatrix} (\tau^3/3)A^2(K_1+E_1) & 0 & 0 \\ -(\tau^2/2)A^2(K_2+E_2) & 0 & 0 \\ (\tau/2)A^2(K_3+E_3) & 0 & 0 \end{bmatrix}_{3 \times 3} = \begin{bmatrix} B_{11} & 0 & 0 \\ B_{12} & 0 & 0 \\ B_{13} & 0 & 0 \end{bmatrix}_{3 \times 3} \quad (22)$$

In the above equation,

/88

$$\begin{aligned} K_1 &= k^3 + 3k^2 + 3k + 3/2, \quad K_2 = k^2 - 2k, \quad K_3 = k^2 + 1 \\ E_1 &= (E - 2k - 1)^2, \quad E_2 = E^2, \quad E_3 = (E - k - 1)^2 \\ B_{11} &= [(\tau^3/3)A^2(K_1 + E_1)]_{3 \times 3}, \quad B_{12} = [-(\tau^2/2)A^2(K_2 + E_2)]_{3 \times 3} \\ B_{13} &= [(\tau/2)A^2(K_3 + E_3)]_{3 \times 3} \end{aligned}$$

From B, we can define the controllability matrix of the two components in the interception

$$W_d(t_n, t) = c_d B = c_d \int_0^t B(t)B'(t)S_d dt \quad (22a)$$

$$W_m(t_n, t) = c_m B = c_m \int_0^t B(t)B'(t)S_d dt \quad (22b)$$

Therefore, for $\xi = 1$, the difference between the controllability matrices lies only in c_d and c_m . In other words, one of the necessary conditions for a successful interception is $c_d > c_m$.

We only have to substitute Eq. (22) into Eq. (17a) to obtain the inverse of P . Let $c = c_d - c_m$. Then,

$$P^{-1} = \frac{1}{1+cB_{11}} \begin{bmatrix} 1 & 0 & 0 \\ -cB_{12} & (1+cB_{11}) & 0 \\ -cB_{13} & 0 & (1+cB_{11}) \end{bmatrix} \quad (23)$$

Finally, substitute Eqs. (21) and (16) into Eq. (15), taking account of Eqs. (18), (16) and (6), and we obtain the optimal guidance law:

$$\begin{aligned} u_s^0(t) &= -c_s B'(t) \lambda(t) = -c_s B'(t) S_t P^{-1} Z(t) \\ &= -\frac{c_s \tau (k-E) [\lambda r + T \lambda v + \tau^2 (k-E) \lambda v^2]}{1/A^2 + (c_s - c_m)(\tau^2/3)(\cdot)} \end{aligned} \quad (24)$$

In this equation, $[\cdot] = [(k^3 + 3k^2 + 3k + 3/2) + (E - 2k - 1)^2]$. If we take k^3 out of $[\cdot]$ and keep in mind that $T = \tau k$, then it will be easy to see that when $k \rightarrow \infty$, Eq. (27) becomes

$$u_s^0(t) = -\frac{c_s(t_f - t) [\lambda r + (t_f - t) \lambda v]}{1/A^2 + (c_s - c_m)(t_f - t)^2/3} \quad (25)$$

This is the very result given in Ref. [1] for a mass point in three-dimensional space. We can simplify Eq. (25) one step further. When $A^2 \rightarrow \infty$, i.e., the miss-distance is zero, we can obtain, under the condition of a single passage,

$$u_s(t) = \frac{3}{(1 - c_m/c_s)} V \dot{\sigma} \quad (25a)$$

In the above equation, V and $\dot{\sigma}$ are, respectively, the velocity of approach and the angular velocity of the line of sight. $3/[1 - c_m/c_d]$ is the effective navigation ratio, and Eq. (25a) is the familiar proportional guidance law.

Thus far, we have derived the optimal guidance law, Eq. (24), and shown that when the control stiffness becomes infinitely large, Eq. (24) degenerates to that for a mass point.

III. Discussions

A. Proportional Guidance Law [1]

From the above, we know that Eq. (25) is obtained when $k \rightarrow \infty$. Furthermore, under ideal conditions, $A^2 \rightarrow \infty$, $|\Delta r_f| \rightarrow 0$, and Eq. (25) degenerates to a proportional guidance law:

$$u_0^*(t) = - \frac{3}{1 - c_m/c_d} \left[\frac{\Delta r}{T^2} + \frac{\Delta v}{T} \right] \quad (26)$$

Note that Eq. (26) describes a three-dimensional situation. It /89 can be shown that for very small angles, the angle formed by the line of sight can be represented by the approximate relation $\sigma \approx \frac{\Delta v}{\Delta r} T$. Differentiation and substitution into Eq. (26) yields Eq. (25a). The range for $N = 3/[1 - c_m/c_d]$ is 3-6. In other words, when $c_m = 0$, $N = 3$, and when $c_d = 2c_m$, $N = 6$. This shows that the value of c_d should be taken such that $c_m < c_d < 2c_m$. The physical interpretation of this is that the mobility of the missile should be higher than that of the target, but not more than twice as high. Excessively high mobility presents difficulties to missile design, and is not rational.

Hence we know that the proportional guidance law is an optimal guidance law under given conditions. Some factors have been taken into consideration in deriving Eqs. (25) and (24), which can therefore be considered as modifications of Eq. (25a) in a certain sense.

B. Suboptimal Guidance Law

The suboptimal guidance law is obtained from the optimal guidance law through certain approximations and simplifications under given conditions. It is more convenient to realize in practical situations. It has been mentioned above that, when

the control stiffness is taken into consideration in the proportional guidance law, the stiffness is considered as being finite during the entire process of guidance, and the time constant of system is taken to be relatively stable, then an approximate guidance law can be obtained from Eq. (27) after elimination of the terms $1/k^2$, $1/k^3$, etc. We call this the "suboptimal" guidance law. In this case, in the denominator of Eq. (24), $[\cdot] \approx k^3[1 + 7/k]$. Considering that $A^2 \rightarrow \infty$, i.e., $|Z|_f \rightarrow 0$, we obtain

$$u_s(t) = (C_1^*(k, T), C_2^*(k, T), C_3^*(k, T))_{3,3}(\Delta x)_{3,1} \quad (27)$$

In the above equation

$$\begin{aligned} C_1^*(k, T) &= \left[\frac{-(k-E)}{1/3(1-c_m/c_d)(k+\tau)T^2} \right]_{3,3} \\ C_2^*(k, T) &= \left[\frac{-(k-E)k}{1/3(1-c_m/c_d)(k+\tau)T^2} \right]_{3,3} \\ C_3^*(k, T) &= \left[\frac{-(k-E)k^2}{1/3(1-c_m/c_d)(k+\tau)T^2} \right]_{3,3} = [0]_{3,3} \end{aligned}$$

Actually, in the process of missile guidance, k does not vary linearly with t . This is mainly because, in the entire air space, τ is closely related to height H and Mach number M . However, no matter how τ varies, k is not equal to 0. Nevertheless, as k is always very small in the last stage of guidance, Eq. (27) is not "suboptimal" throughout the entire process of guidance.

C. On the Introduction of k

We introduced the parameter k into Eq. (24) in Section II, and called it the control stiffness. k has a definite physical meaning, and reflects the response characteristics and controllability of the system.

In a control system, an increase in control stiffness produces the same effect as a decrease in inertia, both resulting

in an increase of the natural frequencies of the system. In other words, with the increase in k , the bandwidth of the system increases. It can thus be seen that k is a fairly important parameter of the system. Besides being related to the system time constant T_s , the amplification coefficient K_s and damping ζ_s , it obviously is a function of the parameters H and M in the entire air space involved in the interception. Hence, we can express k as $k = f_{k1}(T_s, K_s, \zeta_s, t)$ or $k = f_{k2}(H, M, t)$. In other words, k is not a simple function of t . Therefore, it is not reasonable to regard τ as a constant in Eq. (24), and determine k as a linear function of t . In fact, except in a very few cases, τ depends on H and M to a great extent. Thus we have a problem: Even though taking k as a linear function of t simplifies the form of the guidance law, there is a definite deviation from the actual situation. Would it be possible to remedy this inadequacy? The answer is positive, theoretically. The simplest method would be to regard τ as being a linear function of t within different height ranges, with τ increasing in value with the height. A finite number of linear $\tau - t$ relations can thus be synthesized for the different height ranges, which can be used to modify the value of k . Such a modification of the value of k is expected to make up for the loss resulting from taking τ as a constant.

The introduction of k and the use of k , E and T in place of the time factors t_f and t has given the resulting form clarity, simplicity and definite physical meaning, and facilitated the derivation and analysis. At the same time, it has imparted a new meaning to synthesis in the application and further study of guidance laws. /90

In Eq. (24) the feedback gain of the guidance law is a function of the parameters T , k and E . This shows that the gain is not just a function of time, but is directly related to the system control process time and the system control stiffness. Moreover, because T , k and E are simple functions of

t ($T = t_f - t$; $k = T/\tau$; $E = 1 - e^{-T/\tau}$), they can be easily obtained in the order $t \rightarrow \tau \rightarrow T \rightarrow k \rightarrow E$, no matter what form τ takes.

Furthermore, in studying guidance laws, the object is usually to increase the guidance accuracy and realize real-time control, so as to minimize control energy and terminal miss-distance. This, of course, requires a very accurate description of the system so that the guidance law synthesized will meet the practical demands. The fact is, however, that synthesis would be impossible without the introduction of some necessary simplifications of the system. For instance, if the dynamics of the missile are described by means of a linear system of higher than the third order, synthesis becomes very difficult. How to overcome this difficulty is a problem yet to be solved. One attempt could be to carry out a certain synthesis on k , based on the physical meaning of k and taking into consideration the various factors affecting k , and then use this k to improve the results obtained under the assumption of a first-order system. (Note that when complex characteristics are taken into consideration, the synthesis of k will be very difficult.) One could thus make up for the inadequacies that result from over-simplified assumptions, and at the same time avoid complications associated with the use of a high-order system. The introduction of k further improves the problem of divergence in the terminal stage of interception. How to synthesize the parameter k requires further study.

In summary, the introduction of the parameter k not only has resulted in a simplification in the form of the result, but has also given us insight into the methodological aspect of the problem.

D. About the Controllability Matrices $W_d(t_f, t)$ and $W_m(t_f, t)$

The controllabilities of the missile and the target in the intercept system are determined by Eqs. (22a) and (22b). The fact that these are simplified controllability matrices can be seen from the following transformation:

$$c_d B = c_d A^2 \exp(FT) G G' \exp(F'T) = c_d A^2 (W) (T(t)) (W)' = c_d A^2 W T \quad (28)$$

In the above,

$$(W) = [G, FG, \dots, F^{n-1}G],$$

$$(T(t)) = \begin{bmatrix} 1 & T & \dots & T^n/n! \\ T & T^2 & \dots & T^3/2! \\ \vdots & \vdots & \ddots & \vdots \\ T^n/n! & \dots & T^{2n}/n!n! \end{bmatrix}, (T) = \int_t^{t_f} (T(t)) dt$$

Obviously, W is the controllability matrix of F and G , and therefore W is also a type of controllability matrix. Bearing in mind that $B_d(t) = B_m(t) = B(t)$, we know that the relative controllability of W_d and W_m is dependent on c_d and c_m only. $W_d > W_m$ would mean $c_d > c_m$, which means that the controllability of the missile is higher than that of the target. Note, however, that $c_d > c_m$ does not refer simply to the control energy, but to the controllability matrix formed from c_d , c_m and B . Therefore, improvement of controllability involves not only the selection of c_d and c_m , but also taking proper account of the constraints on the changes in the state of the system. From the standpoint of energy consideration, both sides of the intercept system try to achieve their goals, viz. interception or escape, with minimum energy consumption. Hence, the weighting factors $1/c_d$ and $1/c_m$ are required to be large. On the other hand, the requirement of higher controllability of missile over target, for example, demands that $W_d > W_m$, thus insuring the interception of the target by the missile. However, this does not mean that one must have $W_d \gg W_m$. In fact, an excessively large W_d results in an excessively high control power and controllability reserve, which is not necessarily advantageous for a given system index J , noting

that we are interested in satisfying the condition of J at the lowest cost. Hence, it is not desirable to increase the value of W_d at will, which explains why in proportional navigation the effective navigation ratio is generally not greater than 6.

IV. Conclusion

/91

In the present paper, we have synthesized the optimal guidance law for a missile by applying the theory of differential games to three-dimensional space, and by considering the dynamic responses of the missile and the target as first-order inertial characteristics. We have also introduced into the result the concept of control stiffness. The system control stiffness k is regarded as a parameter in the feedback gain. The gain is thus not only a function of k , but also related to system characteristics. This makes it possible for us to establish a definite relationship among the gain and the other parameters of the system such as T_s , K_s , ξ_s , and even H and M , by a careful study of k . This relationship can be used to improve the effect of the guidance law. Therefore, the concept of k represents a new concept in synthesis, and has simplified and clarified the results, thus facilitating the derivation and analysis.

When $k \rightarrow 0$, the denominator of Eq. (24) does not contain $(t_f - t)$, and the problem of divergence in the last stage of interception becomes less severe [2].

Finally, we have briefly discussed the problem of degeneration of Eq. (24), and also given the suboptimal guidance law for the case of finite stiffness. Methods for synthesizing k need further studying.

We would like to thank Comrades Sung Chien and Wang Yen-tsu for proofreading this paper and for their valuable suggestions.

Appendix

I. Basis Matrix $\phi(t_f, t)$

From matrix theories, we know that when the coefficient matrix is a constant matrix,

$$\phi(t_f, t) = e^{FT}, \quad T = t_f - t \quad A1$$

Making use of the expansion $e^{FT} = 1 + FT + \frac{1}{2!}F^2T^2 + \dots$, and taking into account Eq. (19a), we obtain

$$e^{FT} = \begin{bmatrix} 1 & T & F_{11} \\ 0 & 1 & F_{12} \\ 0 & 0 & F_{13} \end{bmatrix} \dots \quad A2$$

In the above,

$$F_{11} = \frac{T^2}{2!} - \frac{1}{3!} \left(\frac{T^3}{\tau} \right) + \dots, \quad F_{12} = T - \frac{1}{2!} \left(\frac{T^2}{\tau} \right) + \dots, \quad F_{13} = -\frac{T}{\tau} + \frac{1}{2!} \left(\frac{T^2}{\tau^2} \right) - \dots$$

After rearrangement and combination, we obtain Eq. (20).

II. Finding the integral $B = \int_t^{t_f} B(t)B'(t)S_f dt$

Using Eqs. (9) and (21), and performing some simple integrations, i.e., $\int_t^{t_f} E dt$, $\int_t^{t_f} k dt$, $\int_t^{t_f} E^2 dt$, $\int_t^{t_f} k^2 dt$ and $\int_t^{t_f} k E dt$, it will be fairly easy to obtain B from k and E

$$B = A^2 \int_t^{t_f} \begin{bmatrix} \tau^2(k-E)^2 \\ \tau E(k-E) \\ (1-E)(k-E) \end{bmatrix} \begin{bmatrix} 0 \\ 0 \\ 0 \end{bmatrix} dt = \begin{bmatrix} B_{11} \\ B_{12} & 0 & 0 \\ B_{13} \end{bmatrix} \dots \quad A3$$

III. The Case of $\xi \neq 1$

Let $\xi \neq 1$, then $\tau_2 = \tau + \Delta\tau$. Omitting second-order infinitesimal quantities, we obtain

$$\dot{x}_m(t) = F_m x_m(t) + G_m u_m(t) + \begin{bmatrix} 0 \\ 0 \\ \Delta\tau/\tau^2 \end{bmatrix} (u_m(t) - u_m(t)) \quad A4$$

Obviously, the first two terms in A4 are the state equations of Eq. (2), and the last term is the difference arising from $\xi \neq 1$. Consider the linear relation $a_m(t) = \frac{t}{\tau} u_m(t)$ at $t < \tau$. Here, the difference term is $[0, 0, 1/\tau]' \Delta u(t)$ where $\Delta u(t) = \frac{\Delta \tau}{\tau^2} \times (t - \tau) u_m(t)$. In other words, $\xi \neq 1$ is equivalent to $\xi = 1$ with an increment $\Delta u(t)$ of the target strategy. Therefore, the worst possible condition for interception will be where $\tau_2 = 0$, i.e., $a_m(t) = u_m(t)$. Hence, omitting $\Delta u(t)$ and letting $\xi = 1$ places a more stringent condition on interception strategy.

REFERENCES

1. A. E. Bryson, Jr., Yu-Chi Ho, "Applied Optimal Control," 1975.
2. Kuan Chao-chih, "Looking at Tactical Missile Guidance from the Point of View of Modern Control Theory," "Tzu Liao Hui Pien," Chung Kuo Hang K'ung Hsueh Hui, 1979.
3. Kuan Chao-chih, "Some Problems in Modern Control Theory II," "Tzu Tung Hua Hsueh Pao," No. 2, Vol. 6, 1980.

DEFORMATION WORK DENSITY FRACTURE CRITERION
FOR COMPOSITE MATERIALS

/93

Hsüeh K'e-hsing and Chou Chin
(Aircraft Structural Mechanics Research Institute)

ABSTRACT

/100

A method for predicting the fracture strength of composite laminates with notches is an important research topic and very useful for engineering application.

An experimental research on C/EP and G/EP composite laminate specimens with a single notch, a centric circular hole or a sharp tipped crack was accomplished. It is proved that the results of J-integral analysis for isotropic materials [1] are applicable to determining the characteristic of length d_0 of the fracturing zone in composite materials after taking their anisotropy into account.

Based on the finite element analysis [2] of notched composite laminates and experimental observation [3], a new fracture criterion for composite laminates under a uniaxial tensile load is proposed as follows

$$\sigma_x(d_0, 0) \epsilon_x(d_0, 0) = \alpha \sigma_f \epsilon_f$$

This criterion is called the deformation work density fracture criterion for composite laminates as the deformation work density within a distance d_0 from the notch is taken as a main parameter.

In order to verify this model the tests for C/EP ($0^\circ/\pm 45^\circ/0^\circ/\pm 45^\circ/90^\circ$), and woven glass fiber/epoxy ($0^\circ/90^\circ$) composite laminates with a centric hole or a crack of different sizes have been completed. The fracture strength can be predicted by using this criterion and the characteristic length d_0 obtained from equation (11). Tables 3 and 4 show good agreement between the analytical results and the experimental data.

Received in December 1981.

I. FOREWORD

Although the stress fracture criteria "point stress criteria" and "average stress criteria" [4] proposed by Whitney and Nuismer in 1974 have been used in numerous engineering applications, the results of extensive tests [5] performed on these criteria show that the characteristic lengths chosen by the above said authors do not possess adequate generality. The distribution of the maximum major elastic stress $\sigma_y(x,0)$ around the notch in a sample under a uniaxial tensile load is usually regarded as the basis for establishing the stress criteria. However, the uniaxial tensile stress-strain relation of the multi-axial composite laminates that are widely used in engineering does not retain its linearity up to the point of fracture. Moreover, finite element analysis [2] and experiments [3] that take into account the gradual extension of damage due to the load have shown that a damage zone exists at the crack tip. In this zone, the strain gradient has very high values near the point of fracture. The stress is relaxed and a very complicated stress-strain relation holds. Such conditions have not been reflected in the stress fracture criteria. In addition, it has been proposed in [4] that the characteristic lengths d_0 and a_0 are constants of the material, independent of sample geometry and the distribution of stress. Yet, extensive tests have shown that the characteristic lengths as determined from the stress criteria are actually not constants of the material. In this paper, we do not consider the microscopic mechanism of fracture, but establish an engineering estimation method based on macroscopic phenomenology. We seek to formulate stress criteria and a method for determining the characteristic lengths on the basis of an analysis of the stress deformation field in the notch region, thereby providing a method for predicting the fracture strength.

II. DETERMINATION OF THE CHARACTERISTIC LENGTH d_0 OF THE FRACTURING ZONE

On the basis of the definition and properties of the J-integral, for the notched sample shown in Figure 1 that is under a uniaxial

tensile load, the J-integral has the simplest form if the loop of integration is allowed to close on itself via the inner surface of the notch [6]:

$$J = \int_{\Gamma} w dy = \int_{-\pi/2}^{\pi/2} w(\theta) \rho \cos \theta d\theta \quad (1)$$

For a given sample, $\rho = \text{constant}$. Let $\theta = 0$, $w(\theta) = w_0$, and the above equation simplifies to

$$J = A \rho w_0 \quad (2)$$

where

$$A = 2 \int_0^{\pi/2} \Phi(\theta) d\theta \quad (3)$$

$$\Phi(\theta) = \frac{w(\theta)}{w_0} \cos \theta \quad (4)$$

$$w_0 = \frac{\sigma_0 \epsilon_0}{1 + n} \quad (5)$$

σ_0 and ϵ_0 are, respectively, the stress and strain at the tip $\theta = 0$, $x = 0$ of the notch. ρ is the radius of curvature of the notch and n is the index of strain hardening.

Assume that the distribution of the deformation work density along the x-axis in the vicinity of the notch in a multi-axial composite laminated slab is the same as that for an isotropic slab, as shown below [1]:

$$\sigma_x(x, 0) \epsilon_x(x, 0) = \sigma_0 \epsilon_0 \left(\frac{\rho}{\rho + bx} \right) \quad (6)$$

In the above equation, b is a constant. Please refer to [4] for its significance and numerical values.

Both experiments and calculations indicate that the initiation of the fracture of composite laminates cannot be determined from the fact that σ_0 and ϵ_0 have reached their critical values σ_F and ϵ_F . Rather, it should be determined from the

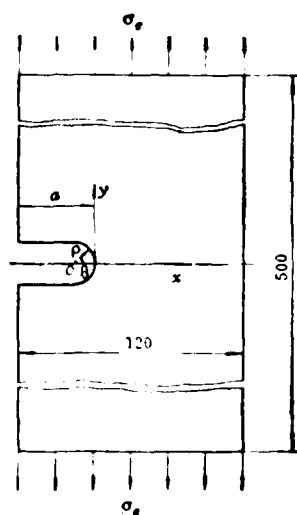


Figure 1. The notched specimen.

condition that the deformation work density $\sigma(d_0, 0)\epsilon(d_0, 0)$ at a definite distance $x = d_0$ from the tip of the notch has reached its critical value. Quantities σ_F and ϵ_F are the fracture stress and fracture strain, respectively, of a smooth sample under a load along the y direction. Substituting σ_F for $\sigma(d_0, 0)$, ϵ_F for $\epsilon(d_0, 0)$, in equation (6), we have

$$\sigma_F \epsilon_F = \sigma_0 \epsilon_0 \left(\frac{\rho}{\rho + b d_0} \right) \quad (7)$$

$$\sigma_0 \epsilon_0 = \frac{1}{\rho} (\rho + b d_0) \sigma_F \epsilon_F \quad (8)$$

From equations (2) and (5), one can obtain

$$J(\rho) = A(\rho + b d_0) \frac{\sigma_F \epsilon_F}{1 + n} \quad (9)$$

when $\rho \rightarrow 0$, this gives the value $J(0)$ of the J-integral at the initiation of the fracture of the notched sample:

$$J(0) = A b d_0 \left(\frac{\sigma_F \epsilon_F}{1 + n} \right) \quad (10)$$

from which one obtains the characteristic length

$$d_0 = \frac{1 + n}{A b \sigma_F \epsilon_F} J(0) \quad (11)$$

In equation (11), n , σ_F and ϵ_F can be obtained from uniaxial tension tests performed on the smooth sample. The value for b is taken to be the theoretical value 8 given in [1]. Only A and $J(0)$ remain as unknowns.

1. Determination of A. The value of A can be determined from the results of experimental J-integral analysis [6] performed on a sample with a single notch. We choose a composite slab made of two materials. Material I: C/EP [0°/+45°/0°/+45°/90°], (18 layers), approximately 2.1 mm thick. Material II: orthogonally woven glass fiber/epoxy (0°/90°), approximately 3 mm thick. The measured parameters of the materials along the x and y axes are listed in Table 1.

Figure 2 shows the uniaxial tension stress-strain curves for material I along 0° (y direction), 90° (x direction) and in the directions at 10°, 20°, 30°, 45° and 60° with respect to the y-axis. See Figure 1 and Table 2 for the shape and dimensions of the specimen with a single notch.

TABLE 1. The relevant parameters of materials of the specimens

/95

① 材料类别	E_y (kgf/mm ²)	E_z (kgf/mm ²)	\bar{G}_{yz} (kgf/mm ²)	$\bar{\nu}_{yz}$	σ_p (kgf/mm ²)	ϵ_p	n
② 材料 I	6750	3080	1692.5	0.396	60.63	0.0101	0.87
③ 材料 II	2300	2100	474.6	0.16	30.39	0.0193	1.25

Key: (1) Type of material; (2) - material I; (3) Material II

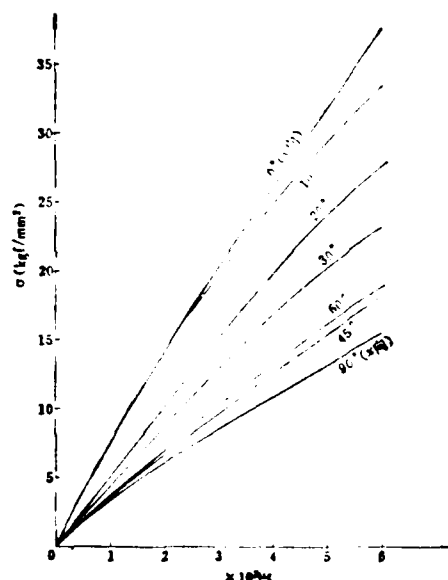


Figure 2. The uniaxial tension σ - ϵ curves in different directions for material I

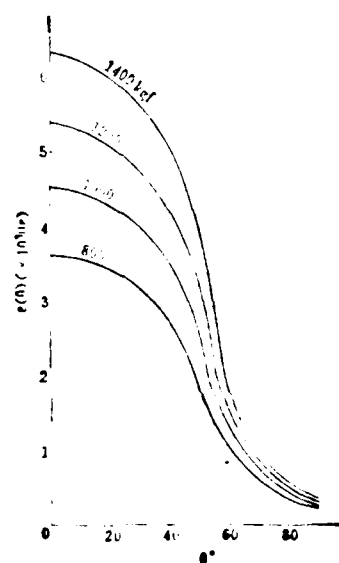


Figure 3. The $\epsilon(\theta)$ - θ curves of specimen no. 5 (material I)

In the tests, strain gauges were attached to the specimens along a circular arc at the root of the notch. The distribution of strain, $\epsilon(\theta)$ - θ curves, was measured (see Figure 3). After the anisotropy of the materials was taken into account, the distribution of deformation work density, the $w(\theta)$ - θ curves (Figure 4) and the $\phi(\theta)$ - θ curves (Figure 5) were obtained. Finally, numerical integration on the $\epsilon(\theta)$ - θ curves was performed, and the value of A was obtained from equation (3). The results of the measurements show that the value of A is very stable for various specimens. The average value of A for material I is 0.975, and for material II is 0.93.

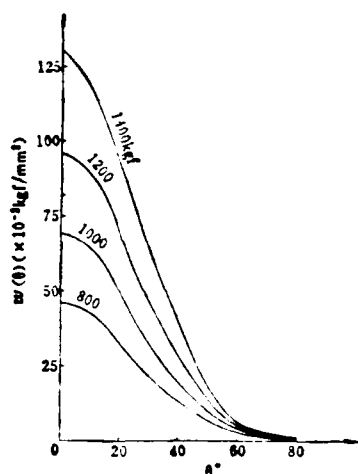


Figure 4. The $K(\theta)$ - θ curves of specimen No. 5 (material I)

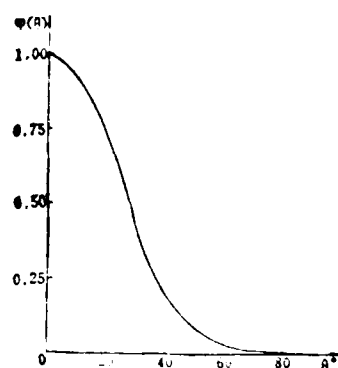


Figure 5. The $K(\theta)$ - θ curves of specimen No. 5 (material I)

TABLE 2. The geometry of the notched specimens

(1) 材料类别	(2) 试件编号	(3) 缺口深度 a (mm)	(4) 缺口曲率半径 R (mm)	(5) 缺口宽度 (mm)
(6) 材料 I	5	40	10	20
	6	40	20	40
(7) 材料 II	3	30	5	10
	8	30	10	20
	9	40	10	20
	10	40	20	40

1--types of material; 2--specimen no.; 3--depth of notch; 4--radius of curvature of notch; 5--width of notch; 6--material I; 7--material II

If the values of A given in this paper are used in the design stage of a composite slab made of many multi-axial layers, the resulting error in the calculated value of fracture strength will be very small.

2. Determination of $J(0)$. The value of $J(0)$ was determined by means of calculations performed on specimens with a centric crack. The formula used is [7]

$$J(0) = \frac{\pi c Y^2 P}{E B^2 W^2} + \frac{U_p}{B(W-2c)} \quad (12)$$

In the equation $U_p = \int P d\Delta$, is the plastic part of the deformation work, P is the load, B is the thickness of the specimen, c is the half-length of the crack and W is the width of the specimen. The geometric correction factors are taken to be the same as those for the isotropic materials

$$Y = 1 + 0.128 \left(\frac{2c}{W} \right) - 0.288 \left(\frac{2c}{W} \right)^2 + 1.525 \left(\frac{2c}{W} \right)^3 \quad (13)$$

The value of $J(0)$ determined from various different crack lengths is fairly stable. The average value of $J(0)$ for material I is 3.8573 kgf/mm and from equation (11), $d_0 = 1.50$ mm. The average value of $J(0)$ for material II is 3.6491 kgf/mm and $d_0 = 1.21$ mm.

III. FRACTURE CRITERION

The conditions for initiation of fracture of a composite laminated slab are different from those for the fracture of the entire specimen. Near the point of fracture, the strain gradient in the damage zone becomes very large, the stress is relaxed, the effects of nonuniformity become more pronounced, and the stress-strain relation deviates from that for a smooth specimen. Actual measurements show that the strain at the tip of the notch can reach a value that is 1.5-3 times that of ϵ_F . On the basis of the stress deformation field analysis performed on this region, one can assume that the composite slab fractures when the deformation work density at a definite distance d_0 from the crack tip reaches a certain critical value, i.e.,

$$\sigma_x(d_0, 0) \epsilon_x(d_0, 0) = \alpha \sigma_F \epsilon_F \quad (14)$$

In the equation, α is a correction factor used to reflect the change in the stress-strain relation at d_0 before the occurrence of fracture.

In the following, we analyze the composite slabs with a centric hole or centric crack by means of equation (14).

1. The case of a centric crack. Take the origin of coordinates to be at the center of the crack and let the load be applied in the y direction. The distribution of strain ϵ_y along the x direction is, for an anisotropic slab, approximately given by the following equation found in [4]:

$$\sigma_x(x, 0) = \frac{\sigma_g x}{\sqrt{x^2 - c^2}} \quad x > c \quad (15)$$

Most composite slabs made of fiber-reinforced resin-type composite materials have uniaxial tensile stress-strain curves for a direction along a main axis of the materials that can be rearranged and formed into folded lines. In general, these can be written as two straight lines

$$\sigma = \bar{E}_y \epsilon \quad \epsilon < \bar{\epsilon} \quad (16a)$$

$$\sigma = \bar{E}_y \bar{\epsilon} + h \bar{E}_y (\epsilon - \bar{\epsilon}) \quad \epsilon > \bar{\epsilon} \quad (16b)$$

In the equations, \bar{E}_y is the corresponding effective elastic modulus, h is the ratio of the slope of the second straight section to that of the first section and $\bar{\epsilon}$ is the strain corresponding to the point of deflection. From equation (16b) one can obtain

$$\epsilon = \frac{1}{h} \left[\frac{\sigma}{\bar{E}_y} - (1 - h) \bar{\epsilon} \right] \quad (17)$$

Equation (14) becomes for a specimen with a centric crack,

$$\sigma_x(c + d_0, 0) \epsilon_y(c + d_0, 0) = \alpha \sigma_g \epsilon_g \quad (18)$$

Substituting equations (17) and (15) into the above equation and rearranging, one obtains

$$\frac{1}{h \bar{E}_y (1 - \xi_1^2)} \sigma_g^2 - \frac{(1 - h) \bar{\epsilon}}{h \sqrt{1 - \xi_1^2}} \sigma_g = \alpha \sigma_g \epsilon_g \quad (19)$$

In the above equation, $\xi_1 = \frac{c}{c + d_0}$. Solve for σ_g from equation (19). The least absolute value of the real root is the desired fracture strength.

2. The case of a centric hole. Take the origin of coordinates to be at the center of the circular hole, and let the load be applied in the y direction. The stress distribution near the hole in an orthogonal anisotropic composite slab is approximately given by the following expression given in [4].

$$\sigma_x(x, 0) = \frac{\sigma_g}{2} \left\{ 2 + \left(\frac{R}{x}\right)^4 + 3 \left(\frac{R}{x}\right)^6 - (\lambda^2 - 3) \left[5 \left(\frac{R}{x}\right)^8 - 7 \left(\frac{R}{x}\right)^{10} \right] \right\} \quad x > R \quad (20)$$

In the equation, K_T is the stress concentration coefficient for an infinitely wide orthogonal anisotropic slab and is determined from

$$K_T = 1 + \sqrt{2 \left(\sqrt{\frac{E_2}{E_1} - \nu_{12}} \right) + \frac{E_2}{G_{12}}} \quad (21)$$

Substituting equations (20) and (17) into equation (14) and rearranging, we obtain

$$\frac{F^2}{E_1 h} \sigma_1^2 - \frac{1-h}{h} \bar{\epsilon} F \sigma_1 = \alpha \sigma_1 \epsilon_1 \quad (22)$$

In the equation,

$$F = \frac{1}{2} \{ 2 + \xi_1^2 + 3\xi_2^2 - (K_T - 3)(5\xi_1^2 - 7\xi_2^2) \} \quad (23)$$

98

$$\bar{\epsilon}_2 = \frac{R}{R + d_0}$$

Solve for σ_g from equation (22). The least absolute value of the real root is the desired fracture strength.

IV. EXPERIMENTAL VERIFICATION OF THE FRACTURE CRITERION

In order to test the applicability of the present fracture criterion, we performed some experiments on specimens prepared from material I and material II that contained centric cracks or centric holes. The cracks were produced by means of ultrasonic waves, while the centric holes were prepared by means of an ordinary drilling machine. Tables 3 and 4 gives the experimental values and the calculated values, as well as related parameters. The value of α was experimentally determined. For the centric crack specimens, it is 0.5 for both kinds of materials. For the centric hole specimens, $\alpha = 0.8$ for material I and $\alpha = 1$ for material II. The results seem to depend on the sensitivity of the material to the process of drilling. For the same material, the same value of d_0 is used for both the centric crack specimens and the centric hole specimens. It is apparent that there is a good agreement between the test results and the calculated values.

TABLE 3. Comparison between computational and test results of centric crack specimens

1. 材料类别	2. 试样编号	3. 试样宽度 (mm)	4. 试样厚 B (mm)	5. 裂纹长 2C (mm)	6. σ_p (kgf/mm ²)	7. σ_m (kgf/mm ²)
8. 材料 I	a-1	39.94	2.1	8.8	27.41	30.64
	a-2	40.12	2.16	16.0	22.61	23.54
	a-3	39.82	2.14	16.5	22.54	20.95
9. 材料 II	L-1	64.0	2.08	23.8	10.35	10.82
	L-2	64.175	2.055	31.93	9.74	9.49
	L-3	64.175	2.075	8.10	17.75	15.90
	L-4	64.15	2.075	16.10	12.14	12.57
	L-5	48.0	2.097	11.98	13.69	13.26
	L-6	32.025	2.073	8.10	15.75	15.32
	L-7	16.025	2.08	4.0	19.29	16.62

TABLE 4. Comparison between computational and test results of centric hole specimens

1. 材料类别	2. 试样编号	3. 试样宽度 (mm)	4. 试样厚 B (mm)	5. 圆孔直径 2R (mm)	6. σ_p (kgf/mm ²)	7. σ_m (kgf/mm ²)
8. 材料 I	d-1	39.94	2.1	8.0	32.60	30.16
	d-2	40.12	2.0	9.2	30.95	30.09
	d-3	40.12	2.04	12.6	27.57	27.24
9. 材料 II	K-1	64.0	2.09	4.0	27.88	21.73
	K-2	64.0	2.08	8.0	20.28	19.25
	K-3	64.0	2.1	12.0	17.38	17.19
	K-4	64.0	2.1	16.1	15.64	15.80
	K-5	64.0	1.97	20.0	17.02	12.47
	K-6	64.0	1.97	24.0	20.28	19.47
	K-7	64.0	1.9	24.30	18.76	14.98
	K-8	64.0	2.05	32.30	12.79	10.85

1--type of material; 2--specimen no.; 3--width of specimen;
 4--thickness of specimen; 5--length of crack; 6-- σ_p calculated;
 7-- σ_m experimental; 8--material I; 9--material II

V. CONCLUSION AND DISCUSSION

A method for predicting the fracture strength of notched fiber /99 composite laminated slabs is a research topic that has received much attention in recent years and has a great significance in engineering applications.

In this paper, the results of J-integral analysis [1] for the stress deformation field in the notch region of an isotropic slab are applied to fiber-reinforced resinous composite laminated slabs whose anisotropy has been taken into account. From this the characteristic length d_0 of the fracturing zone is obtained. We believe this is a more reasonable approach for obtaining d_0 .

Based on the finite element analysis of C/EP composite laminates [2] and experimental observations, we have proposed a new fracture criterion that takes as a main parameter the deformation work density within a distance d_0 from the tip of the crack.

Tests on C/EP and G/EP composite laminates have shown that the method presented in this paper meets engineering requirements. We have been able to successfully predict the fracture strength of centric crack specimens and centric hole specimens made from the same materials, using the value of d_0 . Our method is apparently more reasonable than the "point stress criterion" and the "average stress criterion" used abroad.

Even though we have taken the anisotropy of the materials into account when we applied the results of J-integral analysis for isotropic slabs to composite laminated slabs, the method is nevertheless an approximation. However, our experimental values agree satisfactorily with the calculated values, and the method is very convenient to use because it eliminates the need for a complex microscopic analysis of the notch region.

The use of the J-integral method for fracture analysis on composite laminated slabs has been found elsewhere in the literature. For example, see [8].

Part of the experimental work involved in this study was completed by Comrades Chung Yu and Chiao K'un-fang. This paper was reviewed by Ts'ai Ch'i-kung, a committee member of the Academic Committee of Academia Sinica, and Associate Professor Yang Ping-hsien of Peiching Institute of Aeronautics. We would like to thank them

for their encouragement.

REFERENCES

- [1] Ts'ai Ch'i-kung, On Neuber's Relation $K_t K_c = K_c^2$ --an Application of the J-Integral Theory to the Analysis of the Elastoplastic Stress-Strain Field at the Tip of a Notch. Collected works of the second meeting of the Peiching Practice Mechanics Information Exchange Conference, 1976, 323-332.
- [2] Hseh K'e-hsing, Chou Chin, et al., A Finite Element Analysis on the Course of Damage to Fracture of a C/EP Composite Laminate, Aircraft Structural Mechanics Research Institute Research Report 12-447, 1981.
- [3] Mandell J. F., Wang S. S. and McGarry F. J., The Extension of Crack Tip Damage Zones in Fiber Reinforced Plastic Laminates, JCM, vol. 9 (July 1975), 266-287.
- [4] Whitney J. M. and Nuismer R. J., Stress Fracture Criteria for Laminated Composites containing Stress Concentrations, JCM, Vol. 8 (July 1974), 253-265, or see uniaxial Failure of Composite Laminates containing Stress Concentrations, ASTM STP 593 (1975), 117-142.
- [5] Hseuh K'e-hsing, Fracture Mechanics of Fiber Reinforced Composite Materials (A Review on Related Literature), Aircraft Structural Mechanics Research Institute Research Report 12-428, 1980.
- [6] Luo Li-keng, Ch'en Hsien-Hsi, Ts'ai Ch'i-kung, Chen Min-chung, Experimental J-integral Analysis of a Specimen with a Single Notch, Acta Aeronautica et Astronautica Sinica, Vol. 2, No. 2 (1981).
- [7] Ts'ai Ch'i-fan, Engineering Fracture Mechanics, National Defense Industry Publishing House (1977), 243-381.
- [8] T'eng Ching T'ai I, Tso Ku Sheng, Fracture Mechanics of Composite Materials, Shi Chiao Publishing House (1978), 57-84.

NUMERICAL CALCULATION OF LOCAL CONVECTIVE HEAT TRANSFER
COEFFICIENTS OVER AIR-COOLED VANE SURFACES

Ling Chun-hsiao and Chin Te-nien

(Ch'inghua University)

ABSTRACT

An iterative method for solving two-dimensional compressible boundary layer equations and steady state equations of heat conduction simultaneously is presented and also a FORTRAN program for calculation of the local convective heat transfer coefficients over air-cooled vane surface by means of this method is provided [1]. The approximate integral method is used for solving boundary layer equations and the finite element method is applied to calculating the steady temperature field of the blade.

The input of the program consists of geometry of the blade, pressure or velocity distribution of gas flow external to the boundary layer, entrance flow conditions, internal cooling conditions, nodal numbers and coordinates of the elements. The output includes all principal boundary layer parameters, such as heat transfer coefficients and temperature distribution on the surface and temperature distribution inside the blade. A numerical example has been calculated and the results are favorable compared with the theoretical and experimental data given by other authors.

I. INTRODUCTION

/101

At present, the various methods for determining the heat transfer coefficients over vane surfaces can be divided into three groups, viz. empirical formulae [2], experimental determination [3] and numerical methods [1], [4], [5]. The numerical methods consist of solving the boundary layer equations numerically and determining the distribution of the heat transfer coefficients over the vane surfaces. During the past 10 years or so, there has been a lot of work

Received in October, 1981.

done abroad in this area and many programs for calculation have been published. (At present, not much has been done in this area in our country). To solve the boundary layer equations, it is required to use as boundary conditions the temperature distribution or enthalpy distribution over the vane surfaces. As these distributions are not known beforehand, some authors simply assume a constant wall temperature. (The surface temperature is usually taken to be that of the total temperature of the oncoming stream, as in [1]). Others have made corrections on the constant wall temperature assumption on the basis of empirical data. In this paper, we present an iterative method for solving simultaneously the boundary layer equations and the steady state equations of heat conduction which have a common boundary. This not only overcomes the difficulty associated with the indetermination of the wall temperature, but also enables one to simultaneously obtain the temperature distribution over the vane surfaces.

II. BASIC CONCEPT OF THE ITERATIVE METHOD

The temperature over the vane surfaces is usually unknown. Actually, it is not a constant, but a function of the heat transfer between the inner and outer boundary layers as well as the heat conduction of the vane and other factors. Hence, it is necessary to solve the inner and outer boundary layer equations and the heat conduction equations simultaneously in order to simultaneously determine the heat transfer coefficients of the inner and outer surfaces as well as the temperature distribution inside the vane. To simplify matters, we assume that the cooling condition inside the vane is known and use this as a boundary condition for solving the outer boundary layer equations and the vane heat conduction equations simultaneously.

The general form of the two-dimensional compressible boundary layer equations is [4]

$$\left\{ \begin{aligned} \frac{\partial}{\partial x}(\rho u) + \frac{\partial}{\partial y}(\rho v + \overline{\rho' v'}) &= 0 \end{aligned} \right. \quad (2-1)$$

$$\left\{ \begin{aligned} \rho u \frac{\partial u}{\partial x} + (\rho v + \overline{\rho' v'}) \frac{\partial u}{\partial y} &= \rho u_s \frac{du_s}{dx} + \frac{\partial}{\partial y} \left(\mu \frac{\partial u}{\partial y} - \overline{\rho u' v'} \right) \end{aligned} \right. \quad (2-2)$$

$$\left\{ \begin{aligned} \rho u \frac{\partial h}{\partial x} + (\rho v + \overline{\rho' v'}) \frac{\partial h}{\partial y} &= -u \rho_s u_s \frac{du_s}{dx} + (\mu + \epsilon) \left(\frac{\partial u}{\partial y} \right)^2 + \frac{\partial}{\partial y} \left(\frac{k}{c_p} \frac{\partial h}{\partial y} - \overline{\rho v' h'} \right) \end{aligned} \right. \quad (2-3)$$

/102

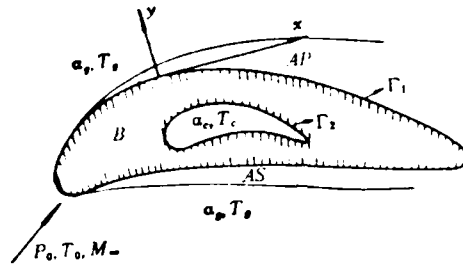


Figure 1. Sketch map for the fundamentals of the iterative method

As shown in Figure 1, $(x, y) \in AP$ and AS , and are orthogonal coordinates. u and v are the x and y components of velocity respectively. ρ , h , μ , ϵ , k and c_p are respectively the local mass density, static enthalpy, dynamic viscosity coefficient, turbulent viscosity, heat conduction coefficient of the gas and specific heat under constant pressure. P_0, T_0 and M_∞ are the total pressure, total temperature and Mach number of the oncoming stream, respectively.

"'", "e", "—", "w" denote, respectively, the pulsation of the turbulent flow, the outer edge of the boundary layer, average value and value at the wall surface.

The boundary conditions for equations (2-1) to (2-3) are

$$\left\{ \begin{aligned} u(x, 0) &= 0 \end{aligned} \right. \quad (2-4)$$

$$\left\{ \begin{aligned} v(x, 0) &= 0 \end{aligned} \right. \quad (2-5)$$

$$\left\{ \begin{aligned} \lim_{y \rightarrow \infty} u(x, y) &= u_s(x) \end{aligned} \right. \quad (2-6)$$

$$\left\{ \begin{aligned} h(x, 0) &= h_w(x) \text{ or } T(x, 0) = T_w(x) \end{aligned} \right. \quad (2-7)$$

However, $h_w(x)$ or $T_w(x)$ in equation (2-7) are not known beforehand, but can only be found from the simultaneous solution of the boundary layer equations and the heat conduction equations for the region B.

Assume that the material properties of the vane are constant; then the two-dimensional steady state heat conduction equations are (please refer to Figure 1):

$$\left\{ \begin{array}{l} \frac{\partial^2 T}{\partial x^2} + \frac{\partial^2 T}{\partial y^2} = 0 \quad (x, y \in B) \end{array} \right. \quad (2-8)$$

$$\left\{ \begin{array}{l} -\lambda \frac{\partial T}{\partial n} = \alpha_g (T - T_g) \quad (x, y \in \Gamma_1) \end{array} \right. \quad (2-9)$$

$$\left\{ \begin{array}{l} -\lambda \frac{\partial T}{\partial n} = \alpha_c (T - T_c) \quad (x, y \in \Gamma_2) \end{array} \right. \quad (2-10)$$

In the above, x and y are rectangular coordinates, T is the temperature, λ is the thermal conductivity of the material of the vane and α_g , T_g and α_c , T_c are, respectively, the heat transfer coefficient and the temperature of the gas flow on the outer surface of the blade and in the cooling passage, respectively.

α_g and T_g are also unknown, but can be found from the simultaneous solution of the heat conduction equations and the boundary layer equations (2-1) to (2-3). Hence, we can assume a random value for $T_w(x)$ (usually assumed to be T_0) and use this in the boundary condition given in equation (2-7) to solve for the heat transfer coefficients $\alpha_g(x)$ and $T_g(x)$ on the surfaces of the blade back and blade basin from their respective boundary layer equations. These are then used in the boundary condition given in equation (2-9) to solve equation (2-8) for the temperature field inside the blade. Now the new temperature distributions $T_w(x)$ on the surfaces of the blade back and blade basin are used in the boundary condition given by equation (2-7) to again solve the boundary layer equations for the blade back and blade basin. This process is repeated until two successive heat transfer coefficients thus obtained have the required degree of accuracy.

III. SOLUTION OF THE BOUNDARY LAYER EQUATIONS

103

Basically, the computer program given in [1] was used to solve the boundary layer equations in this study, except that we corrected

some mistakes in the original program and made some modifications. Two examples calculated by means of the canonical methods given in [6], [7] and [8] have results that agree completely with those in [1].

IV. CALCULATION OF THE TEMPERATURE FIELD OF THE VANE

To determine the temperature distribution over the surface of the vane, it is necessary to calculate the steady state temperature field of the blade which is the same as solving the two-dimensional heat conduction equation, equation (2-8), that satisfies the boundary condition of the third type, equation (2-9). As the solution region G has a fairly complex shape, we make use of the finite element analysis [9], [10]. Finding the solution to equation (2-8) that satisfies equation (2-9) by the variational principle is equivalent to solving for the extreme values of the following general equation:

$$I(T) = \iint_G \frac{\lambda}{2} \left[\left(\frac{\partial T}{\partial x} \right)^2 + \left(\frac{\partial T}{\partial y} \right)^2 \right] dx dy + \int_{\Gamma} \left(\frac{1}{2} \alpha T^2 - f T \right) ds \quad (4-1)$$

In the above, $\alpha = \alpha_g$ or α_c , $f = \alpha_g T_g$ or $\alpha_c T_c$. In order to obtain a better fit for the boundary of the curve, we use 8-node isoparametric elements with curved sides. The 8-nodes of the element e are, in order, (x_i, y_i) , $i=1, 2, \dots, 8$. The temperature at any point can be expressed in terms of an interpolated value of the form function $N_i(\xi, \eta)$ as follows:

$$T(x, y) = \sum_{i=1}^8 N_i(\xi, \eta) T_i \quad (4-2)$$

In the above, T_i is the temperature of the i th node. It can be deduced that the necessary condition for obtaining the minimum value of the general function $I(T)$ is

$$\sum_e \left[\sum_{i=1}^8 (h_i^e + g_i^e) T_i \right] - \sum_i P_i = 0 \quad (4-3)$$

in which

$$\left\{ \begin{array}{l} h_{ij}^* = \iint_e \lambda \left(\frac{\partial N_i}{\partial x} \cdot \frac{\partial N_j}{\partial x} + \frac{\partial N_i}{\partial y} \cdot \frac{\partial N_j}{\partial y} \right) dx dy \end{array} \right. \quad (4-4)$$

$$\left\{ \begin{array}{l} g_{ij}^* = \int_l \alpha N_i N_j ds \end{array} \right. \quad (4-5)$$

$$\left\{ \begin{array}{l} P_i = \int_l f N_i ds \end{array} \right. \quad (4-6)$$

Thus, we arrive at a set of linear algebraic equations that contain n unknowns T_i ($i=1,2,\dots,n$), and whose coefficient matrix possesses the properties of symmetry, orthogonality and being band-shaped. In our program, we adopt the trigonometric method of Gauss-Doolittle for finding the solution. Equations (4-4), (4-5) and (4-6) are calculated by means of Gaussian integrals. 3×3 Gaussian points are used for the integral in equation (4-4). This is the best approach for solving two-dimensional problems [10]. To achieve uniformity over the entire program, we use three Gaussian points for both equation (4-5) and equation (4-6). When doing numerical integration, the approximate values of α and f corresponding to the Gaussian points are found by a three-point parabolic interpolation. (l denotes the boundary of the element e).

During the stage of program test run, we tested the part of the program that solves for the temperature field, using as computational examples a flat slab and cylindrical walls with boundary conditions of the third type. The results show that the calculated values obtained from the part of the program using the finite elements agree completely with the corresponding analytical solutions, with maximum error not exceeding 0.05%. This shows that this part of the program is completely reliable.

Next, based on the fundamental concepts presented in Section II, we wrote an iterative program for solving the boundary layer equations and the heat conduction equations simultaneously. We did some actual computations using as an example the blade shape and related data given in [3]. The calculated results and a comparison with other data are shown in Figures 2 and 3 (curve 5 of Figure 3 is taken from [3]).

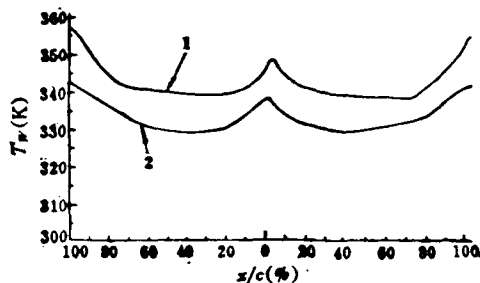


Figure 2. Comparison of the calculated temperature distribution over air-cooled vane surface with the results measured by A. B. Turner [3].
1--the calculated results in this paper; 2--the experimental results given in [3].

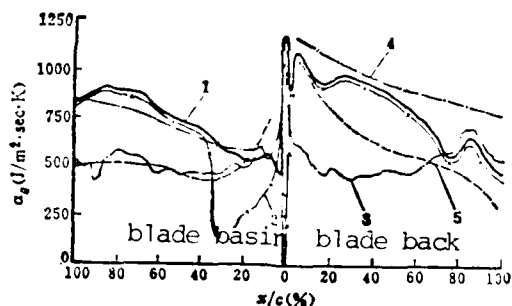


Figure 3. Comparison of the calculated heat transfer coefficients over air-cooled vane surface with the other data.
1--the calculated results in this paper; 2--the calculated results according to [1] (assume $T_w(x)=\text{constant}$); 3--the experimental results given in [3]; 4--the calculated results according to turbulent flat plate law, $Nu_x=0.0292Re_x^{0.8}Pr^{1/3}$; 5--the results according to the theory of Spalding and Patankar.

It can be seen from Figure 2 that there is a fairly good agreement between the temperature distribution over the blade surface obtained from our iterative calculation and the experimental results given in [3]. Not only do the two curves have the same trend of variations, but also the maximum discrepancy does not exceed 4%.

It can be seen from Figure 3 that the heat transfer coefficients for the vane surfaces calculated by means of our iterative method are close to the results of calculation based on the turbulent flat plate law in one region, while in another region, it agrees better with the experimental results given in [3]. In the first 40% chord length region of the blade basin, our results show a great deal of improvement over those calculated from the assumption of constant wall temperature given in [1]. In addition, the value of the heat transfer coefficient of the front nodal point as calculated by means of the program given in [1] always comes out to be zero. This is obviously not acceptable. In our program, we used the heat transfer formula for cylindrical diffracted flow ($Nu_d = 1.14 Re_d^{1/4} Pr^{1/4}$, where d denotes the diameter of the head section of the blade) to calculate the heat transfer coefficient of the front nodal point. The results thus obtained agree very well with those obtained experimentally. Furthermore, no mention was made in [1] of the effect of the degree of turbulence of the main stream on the development of the boundary layer. We performed calculations using the experimental data provided by [3] for different degrees of turbulence. Our results show that the program presented in [1] is applicable for cases with a high degree of main stream turbulence. One should keep this in mind when using this program. The example given in this paper was calculated and compared on the basis of the data given in Figures 10 and 11 of [3] for a 5.9% main stream turbulence. See [11] for a detailed account of the computed example and the program. /105

REFERENCES

- [1] McNally, William D. FORTRAN Program for Calculating Compressible Laminar and Turbulent Boundary Layers in Arbitrary Pressure Gradients. NASA TN D-5681, 1970.
- [2] Daniel J. Gauntner and James Sucec: Method for Calculating Convective Heat-Transfer Coefficients over Turbine Vane Surfaces. NASA TP-1134, 1978.
- [3] A. B. Turner: Local Heat Transfer Measurements on A Gas Turbine Blade. Journal of Mechanical Engineering Science, vol. 13, no. 1, Feb. 1971, pp 1-13.

- [4] H. A. Dwyer: A Computer Program for the Calculation of Laminar and Turbulent Boundary Layer Flows. NASA CR-114366, 1972.
- [5] T. J. Chung: Finite Element Analysis in Fluid Dynamics. McGraw-Hill, Inc., 1978.
- [6] Cohen, Clarence B, Roshotko, Eli: The Compressible Laminar Boundary Layer with Heat Transfer and Arbitrary Pressure Gradient, NACA TR 1294, 1956.
- [7] Sasman, P. K., Cresci, R. J.: Compressible Turbulent Boundary Layer with Pressure Gradient and Heat Transfer. AIAAJ, Vol. 4, no. 1, Jan. 1966, pp-19-25.
- [8] Schlichting, Hermann (J. Kestin, trans.): Boundary Layer Theory, Sixth ed., McGraw-Hill Book Co., Inc., 1968.
- [9] Li Ta-chien, et al. The Method of Finite Element Analysis, Part II, Science Publishing House, 1979.
- [10] K. J. Bathe, E. L. Wilson: Numerical Methods in Finite Element Analysis, Prentice-Hall, Inc., 1976.
- [11] Ling Chun-hsiao, Chin Te-nien: Numerical Calculation of the Heat Transfer Coefficients over Air-cooled Vane Surfaces, Ch'inghua University Science Reports, QH81031.

A BRIEFING ON THE CONFERENCE ON NEW
TECHNOLOGIES IN CHEMICAL ANALYSIS

1107

The Chinese Society of Aeronautics and Astronautics sponsored a conference on new technologies in chemical analysis that took place in Shenyang from June 1-5, 1982. The meeting was planned and prepared by the Physical and Chemical Properties Testing Team of the Committee on Materials. 58 papers were received in all, 34 of which were either delivered as special topic reports or read in one of the large or small meeting rooms. The subjects included chemical analysis techniques in the areas of atomic absorption spectrophotometry, ion-selecting electrodes and three-component polymers.

Through this information exchange, the achievements made in recent years in new chemical analysis techniques have been reviewed, and the attendant scientists obtained a better understanding of the development of chemical analysis techniques at home and abroad and its importance in the entire domain of scientific technology and in the development of the economy of the people.

Besides the exchange of academic information, the conference also included small-scale panel discussions on the subject of future development of chemical analysis. It was pointed out that this development should be such as to improve speed, reduce the required sample quantity and reduce pollution of the environment. Future conferences should as much as possible be specialized, frequent and with variety. Short training courses should be offered when necessary to enhance the understanding and application of certain new techniques. The scientists who attended the meeting gained a lot from the absorbingly interesting discussions and the enthusiasm shown. The team conducting the meeting discussed and agreed that the next conference should be held in 1984.

AD-A131 828

ACTA AERONAUTICA ET ASTRONAUTICA SINICA(U) FOREIGN
TECHNOLOGY DIV WRIGHT-PATTERSON AFB OH S LU ET AL.
28 JUL 83 FTD-ID(RS)T-0266-83

3/3

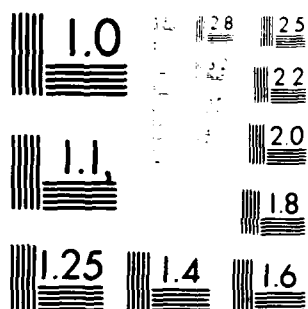
UNCLASSIFIED

F/G 20/4

NL



END
9-83



Microcopy Resolution Test Chart
 NATIONAL BUREAU OF STANDARDS-1963-A

CHINESE SOCIETY OF AERONAUTICS AND ASTRONAUTICS HOLDS INAUGURAL
MEETING FOR COMMITTEE ON FLIGHT MECHANICS AND FLIGHT TESTS

/107

The Chinese Society of Aeronautics and Astronautics held an inaugural meeting for its Committee on Flight Mechanics and Flight Tests in Kuangchou from August 13-17, 1982. 140 professors, specialists and engineers came as representatives of 48 scientific research, design, production and instruction departments. There were 11 committee members present at the meeting.

An academic information exchange meeting was held alongside the inaugural meeting. 80 papers were received in all. Two of the papers were read during the general meeting, while the rest were discussed in one of three groups, viz., flight quality research on aircraft carrying automats, flight quality research on aircraft flying under the conditions of atmospheric turbulence, large angle of attack, large side-glide angle or asymmetrical power and the fabrication, use and data manipulation of test instruments for flight tests. The papers related theory to practice, and were in accordance with the standards set for the flight quality of our military aircraft. Some of the papers given by some younger members of certain research or design institutes were received with enthusiasm. Chang Tsu-yen's "Computation and Analysis of Different Choices of Automaton for a High-Altitude High-Speed Attack Aircraft", Po Chao-kuey's "A Calculation of the Dynamic Response of a Big Transport to Atmospheric Turbulence" and Chiang Hsing-wei's "Breakdown Tests on Machines Working under Normal Conditions--An Application of the Inverse Spectrum" were among those with richer contents and definite practical values. Everybody felt this was a good sign.

During the meeting, the first meeting of the committee was also held. Discussions were held and corresponding decisions were made regarding the special study group formed under the committee and the academic activities to be engaged in during the next year.

CHINESE SOCIETY OF AERONAUTICS AND ASTRONAUTICS, CHINESE SOCIETY
OF MECHANICS AND CHINESE SOCIETY OF SPACE NAVIGATION JOINTLY HELD
THE SECOND NATIONAL CONFERENCE ON COMPOSITE MATERIALS

/108

The second National Conference on Composite Materials held jointly by the Chinese Society of Aeronautics and Astronautics, the Chinese Society of Mechanics and the Chinese Society of Space Navigation took place in Harbin from August 18-22, 1982. 265 representatives from 97 departments of the various science research institutes, factories and colleges all over the nation attended. The Chinese Society Association, the National Defense Science and Industry Committee and the National Science Committee put much emphasis on this meeting and sent their representatives to attend and speak at the meeting.

230 papers were received. These were either circulated or read during one of the sessions. Based on the contents of these papers, four special topic groups were formed: resin-based composite materials and industrial arts, hull and optimizing design, fracture fatigue properties and metal-based composite materials. Through this exchange of information, a better idea was obtained of the rapid development of advanced composite materials in our country during the past two years. The papers received were superior to those received for the first National Conference on Composite Materials. However, these works were still in the stage of theoretical study and scientific experimentation. Much remains to be done in the area of practical application. To achieve this, the representatives pointed out that theoretical research and scientific experimentation should be combined with practical applications without putting too much emphasis on either of these. The following were deemed important: stability of material properties, composite industrial arts, substrate design, structural analysis and design, connection design and materials industrial arts, effects on and protection of the environment, quality control and non-destructive testing techniques, machine processing and cost reduction, etc.

Some special topic discussions were also held during the conference. Arrangements were made for the attendant representatives to visit the "dolphin" helicopter.